Modeling 2009 in Massachusetts Bay using the unstructured-grid Bays Eutrophication Model

Massachusetts Water Resources Authority
Environmental Quality Department
Report 2010-22

Modeling 2009 in Massachusetts Bay using the unstructured-grid Bays Eutrophication Model

Submitted to

Massachusetts Water Resources Authority
Environmental Quality Department
100 First Avenue
Charlestown Navy Yard
Boston, MA 02129
(617) 242-6000

Prepared by
Rucheng Tian, Liuzhi Zhao, Changsheng Chen and Pengfei Xue
School for Marine Science and Technology
University of Massachusetts-Dartmouth
New Bedford, MA 02744

And

Wendy S. Leo and Michael J. Mickelson
Environmental Quality Department
Massachusetts Water Resources Authority
Boston, MA 02129

December 2010

Citation:

Tian RC, Chen C, Zhao LZ, Xue P, Leo WS, Mickelson MJ. 2010. **Modeling 2009 in Massachusetts Bay using the unstructured-grid Bays Eutrophication Model**. Boston: Massachusetts Water Resources Authority. Report 2010-22. 100p.

Key word acronyms and definitions

ECOM-si	Estuarine and Coastal Ocean Model-semi-implicit. A structured-grid hydrodynamic model.
FVCOM	Finite-Volume Coastal Ocean Model: An unstructured-grid hydrodynamic model.
GoM/GB FVCOM	FVCOM applied to the Gulf of Maine/Georges Bank.
RCA	Row Column Advanced (RCA) ecological systems operating program: a water quality model.
UG-RCA	Unstructured-grid version of RCA.
MB	Massachusetts Bay.
BEM	Massachusetts Bays Eutrophication Model: a coupled water quality and hydrodynamics model system.
BH	Boston Harbor
WRF	Weather Research and Forecast Model

EXECUTIVE SUMMARY

The Massachusetts Water Resources Authority (MWRA) contracted the Marine Ecosystem Dynamics Modeling (MEDM) laboratory of University of Massachusetts at Dartmouth (UMASSD) to simulate currents, temperature, salinity, dissolved oxygen, and other water quality parameters in Massachusetts Bay for the calendar year 2009 using the newly-developed unstructured-grid water quality model (UG-RCA). This report presents the simulation, validation, and interpretation for the hydrodynamic model and the water quality model. Projection of the impact of the MWRA effluent on water quality parameters such as algal development and dissolved oxygen level are presented as well.

We first conducted a hydrodynamic simulation using the Finite-Volume Coastal Ocean Model (FVCOM) which was used to drive the UG-RCA water quality simulation. The simulation was conducted in a nesting mode with a regional domain covering the entire Gulf of Maine and Georges Bank and a local domain for Massachusetts Bay (MB). Surface forcing including solar radiation, heat flux and wind were simulated using the Weather Research and Forecast model (WRF). For the regional model, 33 rivers were included of which 13 were located in the local domain. Five major tidal constituents were included at the open boundary of the regional domain; the local model was forced by the output of the regional model at the boundary. Data assimilation was conducted with the data from the MWRA monitoring program and all other available data in the region. The model successfully reproduced field observations in terms of temperature and salinity.

The water quality simulation using UG-RCA reproduced most of the observed magnitudes and seasonal cycles of water quality variables. The seasonal variation of the water quality field was dominated by a spring phytoplankton bloom characterized by high chlorophyll concentration and decreased nutrients in surface waters in spring, in both observations and model. Dissolved oxygen (DO) showed high values during the spring phytoplankton bloom as a result of photosynthetic production, but remained at a low level in fall, especially in the model results. This suggests that the DO dynamics are controlled by multiple factors such as high consumption by increased remineralization and low solubility under the high temperature characteristic of late summer and early fall. Multiyear comparisons revealed two contrasting phenomena in 2009: first, the spring phytoplankton bloom occurred about one month later in 2009 than in the previous years. Secondly, no fall bloom was predicted in 2009 whereas it was well developed in the previous years.

Based on our projection analysis, the outfall plume was mostly restricted to a local area about 20 km wide. However, long-distance effluent nutrient dispersal as far as down to the Cape Cod Bay was predicted under certain circumstances in March and December 2009. In the vertical dimension, the plume was basically constrained within the bottom 10 m during the stratified season in summer and early fall. In winter and late fall when the vertical mixing was strong, the outfall effluent plume can reach to the surface layer. However, no substantial bay-wide influence was observed on chlorophyll or DO levels. As the upward mixing and long-distance dispersal occurred during winter and late fall when light intensity limits phytoplankton growth, effluent nutrients were not effectively taken up and translated into phytoplankton biomass and subsequent biogeochemical cycles during that period of time.

Table of Contents

List of Figures

List of Tables

1. Introduction

1.1 Project overview

The Massachusetts Water Resources Authority (MWRA) has established a long-term monitoring program to evaluate the impact of MWRA sewage treatment plant effluent on the ecosystem function and water quality in the Massachusetts Bay system (MBS) including Boston Harbor (BH), Massachusetts Bay (MB) and Cape Cod Bay (CCB). The monitoring program primarily consists of an array of field observations, but is complemented by water quality modeling as required by the MWRA permit for effluent discharge into MB. Up to 2007, the water quality model RCA (Row-Column Advanced Ecological Systems Operating Program) developed by HydroQual was applied to MBS by HydroQual (1994-1999), University of Massachusetts Boston (2000-2005) and University of Massachusetts Dartmouth (2006-2007) (HydroQual, 2000; HydroQual, 2003; Jiang and Zhou, 2004a, b, 2006a, b, 2008; Tian et al. 2009). RCA was driven by the structured-grid hydrodynamic model ECOM-si (HydroQual and Signell, 2001). For the 2008 water quality simulation, we upgraded RCA to the unstructured-grid UG-RCA driven by the Finite-Volume Coastal Ocean Model FVCOM (Chen et al., 2010). Two major updates were included in this upgrade. First, the newly developed RCA version 3 was adapted to MBS whereas an older version was used prior to the 2008 simulations. RCA-v3 is a modular system which has more options and greater flexibility than the previously used version. Secondly, the unstructured-grid finite-volume algorithms well-suited to resolve the complex coastline and bottom topography in MBS were adapted from FVCOM. We tested the newly developed system for the case of 2006 and applied it for the 2008 simulation, which showed that UG-RCA can be successfully applied to MBS. We used this newly developed system for the 2009 simulation. This report presents the details of data treatment, model setup, model-data comparison and interpretation of the simulated results. The figures in this report make use of new color scales suggested by MWRA.

1.2 Physical background

The MBS comprises the Boston Harbor in the west, Cape Cod Bay in the south and Massachusetts Bay in the central region (**Figure 1.1**). It is a semi-enclosed coastal embayment with a length of approximately 100 km and a width of 50 km. The water depth averages about 35 m, with the maximum depth of 90 m in Stellwagen Basin, shoaling to 20 m on Stellwagen Bank. Stellwagen Bank, located on the east side of MB, limits deep-water exchange between MB and the Gulf of Maine (GoM). Deep water exchange occurs mainly through the North Passage off Cape Ann and the South Passage off Race Point.

The hydrodynamic circulation in MBS is subject to both local forcing such as wind and tide and remote forcing through the intrusion of the Western Maine Coastal Current (WMCC) (Bigelow, 1927; Butman et al., 2002). The general circulation pattern within MBS is counterclockwise with inflow through the North Passage and outflow through the South Passage. The inflow is primarily determined by (a) the WMCC which bifurcates near Cape Ann with one branch flowing into MBS (Bigelow, 1927; Lynch et al., 1996) and (b) coastal freshwater discharges, particularly from the Merrimack River located north of the bay (Butman, 1976). Driven by buoyancy and the Coriolis force, a considerable portion the Merrimack River freshwater discharges enters into Massachusetts Bay. Manohar-Maharj (1973) estimated that up to 90% of the freshwater found in Massachusetts

Bay originated from the Merrimack River. However, the amount of fresh water intrusion in to Mass Bay is influenced by many factors such as the WMCC and wind forcing. Local wind forcing can significantly alter the current pattern and velocity (Geyer et al., 1992; Butman et al., 2002; Jiang and Zhou, 2004a). Wind-induced upwelling and downwelling were observed and simulated in previous studies (e.g., Geyer et al., 1992; HydroQual and Signell, 2001; Jiang and Zhou, 2004a; Tian et al., 2009). However, the water column stratification is primarily controlled by seasonal variations in net surface heat flux and freshwater discharge. Water stratification starts in spring due to increased insolation and freshwater discharge, intensifies in summer due to surface heating, and erodes in fall due to surface cooling and increased wind stress, following which the water column becomes well mixed again in winter.

1.3 Biological background

Phytoplankton in the MBS generally shows seasonal cycles typical of temperate regions due to the seasonality in solar radiation, water column stratification and nutrient availability (Libby et al., 1999; Libby et al., 2000). During winter when the water column is well-mixed and solar radiation is weak, phytoplankton growth is restricted due to limited light exposure in most of the MBS. Phytoplankton usually bloom in spring following the establishment of water column stratification and increases in solar radiation. However, spatial differences and interannual variations in the timing of the phytoplankton spring bloom can occur due to local forcing and the physical environment. For example, the spring phytoplankton bloom often develops earlier in CCB than in Stellwagen Basin due to CCB's shallow water depth. During the post-bloom season in summer, phytoplankton biomass is low in most of the MBS due to nutrient limitation, but local phytoplankton growth can still occur due to, for example, wind-driven upwelling activity and river discharge. The fall bloom in MBS usually occurs in late September and early October when increased wind stress and cooling at the sea surface erode the stratification, increasing vertical mixing and replenishing nutrients from the deeper layer to the euphotic zone. With further increases in vertical mixing and decreases in solar radiation, phytoplankton growth is limited again, leading to high nutrient concentrations and low phytoplankton abundance in winter.

The seasonal cycle of phytoplankton production is accompanied by succession in phytoplankton species. Diatoms dominate the spring phytoplankton bloom under nutrient-replete conditions, particularly with high silicate concentrations. On the other hand, phytoflagellate species prevail during the summer stratified season under nutrient-depleted conditions. With the replenishment of surface nutrients in fall, a phytoplankton assemblage of different sizes and species develops. Phytoplankton seasonal succession results in variations in biological parameter values and carbon: chlorophyll ratio. The seasonality in phytoplankton production and biomass is reflected in the secondary production level as variations in zooplankton abundance and species through bottom-up control (Turner, 1994; Libby et al., 2000).

Benthic biological and biogeochemical dynamics directly affect nutrient supply and oxygen demand and thus the water quality of MBS. BH, CCB and Stellwagen Basin are characterized by a soft sea floor with fine sediment and high organic matter content, whereas the coastal regions are mostly covered by coarse sediment and rocks (Kropp et al., 2001; Kropp et al., 2002; Maciolek et al., 2003). In regions of soft floor with fine sediments, sediment oxygen demand (SOD) is higher than that in the hard-floor region. In BH, for example, high values of SOD and nutrient flux have been observed. Outside of the harbor in MB and CCB, physical processes significantly affect

benthic biogeochemical processes where aerobic conditions dominate (Maciolek et al., 2003; Tucker et al., 2002; Jiang and Zhou, 2008). Most of these biological and biogeochemical processes are parameterized in the BEM.

1.4 Modeling updates

The modeling project has played a valuable role in both scientific investigation and decision making for the MWRA outfall design and monitoring program. Before the relocation of the outfall from Boston Harbor to its new offshore position in September 2000, Signell et al. (2000) conducted a series of simulations to analyze the impact of the relocation. They found that the effluent concentration decreased by ten-fold in the harbor whereas relatively elevated effluent concentration was predicted only within several kilometers around the offshore outfall, due to dilution and dispersal in the larger water body. During the summer stratified season, the effluent plume was more restricted in a local domain around the outfall as compared to the winter season when dispersal and dilution dominated. Previous modeling work also showed that the outfall effluent discharge did not have considerable bay-wide effect on the function of the bay ecosystem (Jiang and Zhou, 2006 and 2008; Tian et al., 2009).

The reliability of model predictions depends on the correctness of the parameterization and the robustness of the simulation. Over the years, efforts were continuously made to improve the modeling system. For example, HydroQual and Signell (2001) found that the parameterization of short-wave radiation in the water column is of primary importance to the simulation of temperature variation and distribution. Shortwave radiation energy was initially introduced to the first sigma layer in the physical ECOM-si model, which led to an overheating in surface waters. An exponential decay function with depth was then implemented in the model which considerably improved temperature predictions. Chen et al. (2009) and Tian et al. (2009) found that wind forcing plays a key role in both physical and biological simulations. A spatially-resolved wind field improved model-data comparison and increased DO level in the bottom layer by 9-18% for the case of 2007 as compared with runs driven by uniform wind forcing. The difference is particularly notable during storm events and front passage. HydroQual (2001a) conducted a sensitivity analysis on the impact of boundary conditions on the simulation of water quality variables. They found that certain variables such as DO in the interior of the bay are correlated with values at the open boundary, particularly at the north-northeast region of Mass Bay. Certain variations in bottom DO were directly caused by the boundary conditions. To improve the open boundary condition, Jiang and Zhou (2004b) introduced the objective analysis (OA) method of interpolating boundary conditions based on field observations, which has been used up to the present (Jiang and Zhou, 2008; Tian et al., 2009; Chen et al., 2010 and the present study). HydroQual (2001b) found that the Bays Eutrophication Model with two phytoplankton groups failed to reproduce observed chlorophyll levels in 1993. The addition of a third group notably improved the model prediction. The major characteristic of the third “fall” phytoplankton group is the lower carbon-to-chlorophyll ratio than that in the previous two groups, winter/spring and summer phytoplankton groups. As shown by HydroQual (2002), the chlorophyll simulation can be improved on an annual basis by altering parameter values, but seasonal deviation such as that observed in the fall of 1993 was better resolved by adding the additional fall phytoplankton group compared to sensitivity runs using the two original phytoplankton groups.

Massachusetts Bay (MB) is a complex embayment. First, its varying coastline and bottom topography can induce complex hydrodynamics features such as mesoscale eddies, filaments and coastal jets (Jiang and Zhou, 2006a and b). Second, the Western Maine Coastal Current bifurcates at Cape Ann, with one branch intruding into MB, which represents an external forcing for both physical and biochemical dynamics. Third, wind forcing, combined with the coastline and bottom topography, can generate upwelling and downwelling. Fourth, river discharges further complicate hydrodynamics and nutrient loadings. All of these features are a challenge for the modeling community to get right in the modeling dynamics and setup. Improvements have been continuously made over the years as described above; one major step was the introduction of the Finite-Volume Coastal Ocean Model (FVCOM) and the development of the unstructured-grid water quality model driven by FVCOM (Chen et al., 2009 and 2010). FVCOM is one of the models most suitable to resolve complex coastline and bottom topography. The nesting setup of FVCOM can ensure mass conservation and continuity in physical forcing at the open boundary (Chen et al., 2010).

2. Methods

This section consists of six subsections. The first briefly describes the Finite-Volume Coastal Ocean Model used to simulate the physical fields to drive the water quality model. Next we describe the structure and functionality of the unstructured-grid water quality model used for the 2009 simulation. The third section describes the unstructured triangular grids including the nesting domain and the vertical coordinate. The section on forcing describes both the meteorological forcing for FVCOM and surface forcing for UG-RCA. The fifth section, "Nutrient loading," describes most of the nutrient and organic matter sources including the MWRA outfall. The final section describes how the open boundary condition of the UG-RCA state variables was determined, and describes the data set used for open boundary conditions.

2.1 FVCOM

The unstructured-grid, finite volume, 3D, free surface primitive equation Coastal Ocean Model (FVCOM) was developed originally by Chen et al. (2003). FVCOM is a message-passaging interface parallelized model updated by a team of scientists at the University of Massachusetts-Dartmouth (UMASSD) and Woods Hole Oceanographic Institution (WHOI) (Chen et al., 2006a, b). In the horizontal, FVCOM uses a non-overlapping unstructured triangular grid, which is particularly suitable for resolving the complex coastal geometry of Massachusetts Bay. In the vertical, FVCOM is discretized by layers using the generalized terrain-following hybrid coordinate (Pietrzak et al., 2002). This vertical coordinate system allows for vertical layers of uniform thickness near the surface and bottom over the slope with a smooth transition to topography-following layers in the inner shelf and estuaries, which is critical to resolving the wind-driven surface mixed layer and sloping bottom boundary layer. FVCOM is solved numerically by the flux calculation in an integral form of the governing equations with options of either mode-split (like the Princeton Ocean Model, or the Regional Ocean Modeling System developed at Rutgers) or semi-implicit (like ECOM-si) schemes. The flux calculation ensures the conservation of mass and momentum over individual control volumes and thus the whole computational domain. The finite-volume numerical approach combines the advantage of finite-element methods for geometric flexibility and finite-difference methods for simple discrete code structure and computational efficiency.

FVCOM uses the modified MY-2.5 and Smagorinsky turbulent closure schemes for vertical and horizontal mixing, respectively (Mellor and Yamada, 1992; Smagorinsky, 1963). FVCOM provides optional vertical turbulence closure schemes using the General Ocean Turbulence Model (GOTM) developed by Burchard et al., 2002. The present version of FVCOM contains several new modules: non-hydrostatic dynamics (Lai et al., 2010); advanced data Kalman Filter data assimilation packages (Chen et al., 2009); an unstructured-grid surface wave model (FVCOM-SWAVE) (Qi et al., 2008), an unstructured-grid sea ice model (UG-CICE, Gao et al., submitted), a sediment model (FVCOM-SED) and generalized biological model (FVCOM-GEM). An automatic nesting grid system is also implemented in FVCOM, which allows two different FVCOM models to run through the nested boundary without the need of interpolation from one to another.

2.2 UG-RCA

UG-RCA adapts the biological dynamics and model structure of RCA, but integrates transport and eddy diffusivity using the finite volume algorithms employed in FVCOM. Briefly, it consists of 26 water quality state variables and 23 sediment variables, including various forms of organic carbon, nitrogen and phosphorus, inorganic nutrients, phytoplankton and dissolved oxygen (Figure 2.2). Dissolved oxygen (DO) is a primary state variable of environmental concern in the simulation system. In the model, DO is computed by the reaeration flux at the sea surface, sediment oxygen demand (SOD) at the bottom and internal biological and biogeochemical dynamics in the water column such as phytoplankton photosynthetic production, respiration consumption, biogeochemical oxygen demand through the mineralization of particulate and dissolved organic matter and nitrification. Phytoplankton growth is sustained by solar radiation and dissolved inorganic nutrients including ammonium NH_4^+, nitrate NO_3^- and nitrite NO_2^-, phosphate PO_4^{3-} and dissolved silica SiO_3^{2-}. Nutrients are formed through the mineralization of organic substances in the water column and at the sediment-water interface. In the model, organic matter is divided into dissolved and particulate forms with each being further divided into refractory and labile categories. Zooplankton grazing is not explicitly modeled with trophodynamics, but represented by a first order, temperature-dependent rate of transformation of phytoplankton into particulate and dissolved organic matter. Phosphorus, nitrogen, and silicon were parameterized in a similar way as the organic carbon pools. The total number of state variables is 26: salinity, three phytoplankton groups (spring, summer and fall groups), four nutrients (ammonia, nitrate+nitrite, phosphate and dissolved silica), four organic phosphorus forms, four organic nitrogen pools, seven organic carbon pools (four labile and refractory dissolved and particulate forms plus two reactive and one exudate components), biogenic silica, dissolved and aqueous oxygen.

While the major model structure and biological dynamics of RCA were kept, two major updates were made to UG-RCA. First, RCA uses the total solar radiation to drive phytoplankton photosynthesis; however, only the visible light fraction is reactive with the photosystem of chlorophyll and converted to biochemical energy for carbon fixation. Therefore, the photosynthetically active radiance (PAR) is used to drive phytoplankton growth in UG-RCA instead of the total solar radiation as in RCA. Secondly, the structured-grid RCA requires recalculating the salinity together with water quality variables. This approach is used to check the transport in the water quality model. There is no need to do this in an unstructured grid model. In UG-RCA, the salinity is obtained directly from the physical model output. The volume and mass conservations are checked directly by balancing fluxes in individual control volumes. This saves computation cost, particularly when data assimilation is done on salinity in the physical model, since river discharges, precipitation and evaporation can also alter salinity but are not included in RCA and UG-RCA.

UG-RCA has 180 parameters in total (Table 2.2). In the present model setup, however, 31 of the total 180 parameters are not used, so that there are effectively 149 parameters. Parameters 1-4 are the “option” parameters that control the model setup. Parameter #1 “AGMOPT” stands for “Algal Growth Model Option”, by which users can select different phytoplankton growth functions: “0” to select the standard phytoplankton growth function, “1” to select the Laws-Chalup function. Parameter #2 “ACTALG” defines the number of “Active Algal Groups” effectively simulated in the model. It is assigned a value of 3 for winter-spring, summer and fall phytoplankton groups in Massachusetts Bay. Parameter #3 “KAOPT” defines the choice of reaeration

parameterization: 0 for constant, 1 for spatially variable, 2 for current velocity shear dependent, and 3 for wind stress dependent. Parameter "KEOPT" defines the choice of light attenuation function: 0 for constant, 1 for spatially variable, 2 for temporally variable, 3 for 2D spatially and temporally variable, and 4 for 3D spatially and temporally variable. As PAR is used in UG-RCA whereas GoM-WRF predicts total solar radiation, parameter #5 "PAR" defines the PAR fraction or conversion factor from total solar radiation to PAR. Other parameters are defined in Table 2.2 which essentially control biological and biogeochemical rates in the model.

The sediment module in UG-RCA is essentially the same as the model developed by DiToro (2001). It is designed to capture the sinking flux of organic matter from the water column to sediments, sedimentary diagenesis transforming organic matter into inorganic nutrients, nutrient feedback from sediment to the water column, sediment oxygen demand during sedimentary diagenesis, and denitrification which converts nitrate into gaseous nitrogen (N_2) and thus leads to nitrogen loss from the system through outgassing to the atmosphere. Sediment module parameters are not listed in Table 2.2.

2.3 Model grid

FVCOM used for Massachusetts Bay is a sub-grid domain model (hereafter referred to as MB-FVCOM) nested within the Gulf of Maine regional domain model (hereafter referred to as GoM-FVCOM). The computational domain of MB-FVCOM is configured with 9738 cells and 5472 nodes. The horizontal resolution of this sub-grid domain varies from 290 m near the coast to 5-10 km near the nested boundary (Figure 2.2, upper panel). GoM-FVCOM consists of 27421 cells and 14777 nodes, with the horizontal resolution varying from 10-25 km in the open ocean to 1.0 km near the coast (Figure 2.2, lower panel). GoM-FVCOM uses hybrid terrain-following coordinates with a total number of 30 layers in the vertical. In shallow regions with depth < 60 m, the vertical layers are defined using the σ-coordinate, while in regions with depth ≥ 60 m, the s-coordinate is used. These two coordinates merge on the 60-m isobath at which the water column is divided by uniform layers with a thickness of 2 m. In the σ-coordinate, the layer thickness varies with water depth, with a maximum of 2 m. In the s-coordinate, five uniform layers with a thickness of 2 m are specified in the upper and lower layers adjacent to the surface and bottom, respectively. The remaining mid-depth is divided into 20 layers with thickness varying with water depth. The same vertical coordinate system was used for MB-FVCOM. The GoM regional and Massachusetts Bay sub-domain grids share common triangular cells along the nesting boundary. The model output from GoM-FVCOM at the nested boundary can directly drive MB-FVCOM with no need for any spatial interpolation. This one-way nesting approach ensures volume and mass conservation between the two computational domains.

Both GoM-FVCOM and MB-FVCOM are solved using the mode-split integration scheme. The time step is 12 seconds for the external mode and 120 seconds for the internal mode for GoM-FVCOM, and 5 seconds for the external mode and 50 seconds for the internal mode for MB-FVCOM.

UG-RCA is configured on the same grid as MB-FVCOM, but with a smaller offshore extent (Figure 2.2). It is driven by the hourly MB-FVCOM fields of water temperature, salinity, velocity and turbulence mixing diffusivities. UG-RCA is coded with the flexibility to allow users to select a

different time step from the hydrodynamics model. For the Massachusetts Bay modeling project, the time step used to drive UG-RCA is 50 seconds, with 72 time steps per hour.

2.4 Forcing

2.4.1 Physical models

Both GoM-FVCOM and MB-FVCOM are driven by surface forcing (wind stress, precipitation, evaporation, surface net heat flux, and short-wave irradiance), river discharges and tidal forcing. Please note that the tidal forcing for MB-FVCOM consists of the GoM-FVCOM prediction of surface elevation at the common boundary. Available hydrographic and satellite sea-surface temperature data were assimilated for both simulations.

The surface forcing data were provided by the data-assimilated fields of the WRF (Weather Research and Forecast) model. WRF is the new-generation mesoscale numerical weather prediction system developed principally by National Center for Atmospheric Research (NCAR) through collaboration with other government agencies (http://wrf-model.org/index.php). WRF uses the hydrostatic North American Mesoscale weather model fields as initial and boundary conditions with two-way nesting capability, and can provide continuous hindcasts and 3-day forecasts. WRF replaced the older MM5 in our GoM weather forecast model system (Chen et al., 2005). GoM-WRF is configured with a "regional" domain (covering the Scotian Shelf, Gulf of Maine, Georges Bank, and the New England Shelf) and a "local" domain (covering Massachusetts coastal waters west to Long Island Sound) with horizontal grid spacing of 9 and 3 km respectively, and 31 sigma levels in the vertical with finer resolution in the Planetary Boundary Layer. All available data from the National Data Buoy Center's Coastal-Marine Automated Network (C-MAN) and meteorological buoys are assimilated. The surface wind stress, air-sea heat flux components, and evaporative flux are computed using GoM-WRF output, with a horizontal resolution of 9 km, the COARE 2.6 bulk algorithm (Fairall et al., 1996, 2003), and satellite sea surface temperature. The surface radiative fluxes are computed using International Satellite Cloud Climatology Project (ISCCP) data. The resulting hindcast data-assimilated surface forcing fields are used to drive both the regional GoM-FVCOM and MB-FVCOM.

GoM-FVCOM includes 33 rivers emptying into the GoM region. Of those, 13 are inside the Massachusetts Bay sub-domain. Those, plus the MWRA outfall discharge, are included in MB-FVCOM. The freshwater discharge data from the rivers were directly downloaded from the US Geological Survey (USGS) http://waterdata.usgs.gov/ma/nwis. No accurate discharge data are available for the Mystic River, and its discharge was assumed to be proportional to the Charles River discharge by a factor of 0.195. The daily freshwater flow from the MWRA outfall was provided by MWRA.

Tidal forcing used to drive GoM-FVCOM was specified at the open boundary with the real o'clock time. The tidal elevation at the open boundary is calculated based on amplitudes and phases of five major tidal constituents: three semi-diurnal tides (M_2, S_2 and N_2,) and two diurnal tides (K_1 and O_1). In addition to the surface forcing and river discharge, MB-FVCOM is driven by the lateral boundary conditions specified through one-way nesting with the GoM-FVCOM model output. The surface elevation at the nesting node at the boundary is directly given by the GoM-FVCOM.

2.4.2. UG-RCA surface forcing

UG-RCA is directly driven by the hourly model output field of MB-FVCOM. In addition to the initial and open boundary conditions, UG-RCA requires the surface wind speed and solar radiation as the surface forcing. The wind speed (w) is used to determine the reaeration rate for oxygen exchange at the air-sea interface, which is formulated as:

$$F_{O2} = k\left(DO_{sat} - DO\right) \tag{2.1}$$

$$k = 0.728\sqrt{w} - 0.317w + 0.0372w^2 \tag{2.2}$$

$$DO_{sat} = 14.6244 - 0.36713T + 0.0044972T^2 + 0.0966S + 0.00205S\cdot T + 0.0002739S^2 \tag{2.3}$$

where F_{O2} is the oxygen reaeration flux, DO_{sat} is the dissolved oxygen saturation concentration determined with an empirical function of temperature (T) and salinity (S) (Hyer et al., 1971; HydroQual, 1993), and k is the piston coefficient (also called the piston velocity) of the oxygen air-sea exchange, determined by an empirical function depending on the wind speed (Banks and Herrera, 1977).

The solar radiation is used to compute the phytoplankton growth rate based on the Laws-Chalup function:

$$\mu_{\max} = \frac{G_{pre}\left(1-k_{RG}\right)\left(1-f_{SC}\right)I}{G_{pre}\Big/G_{pr0} + I\left[1+G_{pre}\Big/\left(I_S G_{pr0}\right)\right]}, \tag{2.4}$$

where I is the photosynthetically active radiation PAR (einsteins m^{-2} d^{-1}) and I_s is the half-saturation radiation (Laws and Chalup, 1990). Other parameters are defined in Table 2.2.

Calibrated with satellite-derived shortwave irradiance and available measurement data at the coast, GoM-WRF provides the light intensity at surface required for UG-RCA. The GoM-WRF predicted total short-wave radiation was then converted into PAR using a conversion factor of 0.437 determined based on decadal SeaWIFs PAR data and GoM-WRF predicted total solar radiation (Chen et al., 2010).

The daily average solar radiation exhibits typical seasonal cycles with low values in winter and high values in summer (Figure 2.3). Due to variations in cloudiness, however, low solar radiation occurs throughout the year. The general pattern of seasonal variation of solar radiation is similar between 2008 and 2009, but due to changes in the cloudiness, the detailed insolation can differ from year to year. For example, the insolation in July 2009 was notably higher than that during the same period of time in 2008. The wind speed also shows seasonal cycles, with low values in summer and high values in winter and fall. Daily variations in wind speed are much higher than seasonal variations. Similar pattern in wind seasonal variation was found between 2008 and 2009, but wind events differ between the two years. For example, wind was much stronger in March 2009 than that during the same period of time in 2008. Daylight fraction varies from 0.37 in winter to 0.63 in summer at the latitude of the MBS.

2.5 Nutrient loadings

Nutrient and carbon loadings include the MWRA effluent outfall from the Deer Island Treatment Plant (DITP), non-MWRA point sources, non-point sources, river discharge and atmospheric sources. Each source was specified based on recent observed data when available, combined with historical observations and estimates.

MWRA conducts daily measurements of treated sewage flow in millions of gallons per day and daily or weekly concentration of various pollutants in mg l^{-1}. The data for NO_3^-, NO_2^-, NH_4^+ and PO_4^{3-} were directly used to drive UG-RCA, while the bulk-parameter data of Biochemical Oxygen Demand (CBOD), Total Kjeldahl Nitrogen (TKN) and Total Phosphorus (TP) were first converted and partitioned into model variables (Tables 2.3 and 2.4). For example, CBOD was converted into total organic carbon using the function TOC = 0.7CBOD+18 (HydroQual and Normandeau, 1993) and then partitioned to each organic matter pool using the functions listed in Table 2.3. TKN and TP were converted into total organic nitrogen and phosphorus and then partitioned into their respective organic pools. Silicate was not analyzed on a regular basis at the MWRA outfall. To help determine the silicate loading, MWRA collected four samples over the period of May 19-22, 2009. MWRA's Department of Laboratory Services reported an average value for these samples of 90 μM Si. This value was less than one quarter of the value (12.5 mg/L = 208 μM Si) suggested by HydroQual (1993; p.3-6) for all RCA simulations. We replaced the previous value used in RCA with the value estimated from the measurement.

Non-point source loadings comprise the storm drain system-derived runoff and groundwater discharge which are fully based on historical estimates (Menzie-Cura, 1991; Alber and Chan, 1994). For runoff from combined sewer systems, updates were conducted using the total estimated combined sewer overflow (CSO) volume at the Mystic/Chelsea confluences, the upper inner Harbor, the lower inner Harbor, Fort Point Channel, North Dorchester Bay, South Dorchester Bay and the Neponset River estuary. Estimated annual outflow at these sites were provided by MWRA. These data were divided into monthly values following the same monthly variation in freshwater discharge as the Charles River. The Charles River discharge is correlated with the precipitation in the region (Appendix A of Libby et al. 2009). The pollutant concentrations in combined sewage reported by Alber and Chan (1994, their table 2.4) were used to estimate the contaminant loadings for previous BEM simulations and also for the 2009 simulation with UG-RCA. The groundwater discharges and those from other non-MWRA treatment plants were specified using the same value estimated by Menzie-Cura (1991).

The river discharges included in the UG-RCA simulation were the Charles River, Neponset River and Mystic River. The Merrimack River was included in MB-FVCOM, but not in UG-RCA since it was located outside the UG-RCA sub-domain. The nutrient concentrations near the mouth of these three rivers were measured by MWRA as part of its CSO receiving-water monitoring program; the nutrient loading from these rivers were estimated using the monthly averaged values. Measurements were made of inorganic nutrients, organic phosphorus, particulate organic nitrogen (PON) and dissolved organic nitrogen (DON). The river loadings were estimated by multiplying the river discharge rate with the nutrient concentration. The measured inorganic nutrients can be directly used, whereas the total organic phosphorus must be converted into model variables using the functions listed in Table 2.3. PON and DON measured in rivers were equally split into refractory and labile pools for RPON, LPON, RDON and LDON, respectively; because standard

aquatic measurements of nutrients and carbon do not determine how much is refractory, labile, or very labile (reactive), the coefficients in Table 2.4 are used to partition the measured amounts into the model state variables (HydroQual and Normandeau, 1993.)

The atmospheric loadings were provided using the values estimated by Menzie-Cura (1991). These values were used in the previous BEM simulation (HydroQual and Normandeau, 1995; HydroQual, 2000; HydroQual, 2003; Jiang and Zhou, 2004a; Tian et al., 2009). The loadings included both dry-fall and wet-fall inorganic and organic nitrogen, phosphorus, and carbon.

For organic carbon loading, non-MWRA sewage treatment plants contributed the largest value in 2009 (31%), followed by the MWRA outfall (23%), atmospheric (17%), non-point sources (15%) and rivers (14%) (Figure 2.4). The carbon effluent discharge from the MWRA outfall was comparable to that of the previous years from 2006 to 2008. The 2005 carbon effluent discharge was notably higher than that in the other years. For nitrogen loading, the MWRA outfall represented the largest input (49%), followed by the atmospheric flux (28%), non-MWRA point sources (13%), non-point sources (7%) and river discharge (4%). The 2009 nitrogen effluent discharge was slightly higher than that in previous years, but the difference was a small fraction of the total load (<6% in average). For phosphorus loading, the MWRA outfall again contributed the largest portion (51%), followed by the non-MWRA point sources (27%), non-point sources (15%), river discharge (4%) and atmospheric flux (3%). In contrast to nitrogen effluent, the phosphorous discharges decreased by 8% as compared to the average load from 2005 to 2008.

2.6 Open boundary conditions for UG-RCA

The UG-RCA simulation requires the open boundary conditions of water quality state variables. Following the previous BEM simulation approach, bi-weekly open boundary conditions were specified by using the objective analysis (OA) procedure to interpolate the MWRA field data onto the boundary nodes. The field measurements were made approximately monthly at 7 stations near the MWRA outfall (called "near-field" stations indicated by "N") and bimonthly at 24 far-field stations indicated by "F" (Figure 2.5). Three additional cruises were conducted for the *Alexandrium* red tide monitoring program on May 20, 29 and June 8 (noted as AF stations in figure 2.5).

The data included 14 variables: Chlorophyll, DO, NH_4^+, NO_3^-, PO_4^{3-}, SiO_3^{2-}, DON, DOC, DOP, PON, POC, POP, Biogenic silica and salinity. DON was estimated by the difference between the total dissolved nitrogen (TDN) and total dissolved inorganic nitrogen (NO_3^-, NO_2^-, NH_4^+). DOP was estimated by the difference between total dissolved phosphorus (TDP) and dissolved phosphate (PO_4^{3+}). Particulate phosphorus (PARTP) was used as POP. DON and PON were split equally into labile and refractory pools. The partition coefficients for organic carbon and phosphorus are listed in Table 2.4.

The OA-mapped chlorophyll field was partitioned to the three phytoplankton groups using the partition coefficients listed in Table 2.5. The fraction of the phytoplankton represented by each group changes over time and space in the model. The coefficients in Table 2.5 are the partitions imposed at the open boundary during each season of the year. From January to April, the chlorophyll along the boundary was considered as entirely comprised of the winter-spring phytoplankton group with a zero partition coefficient to the other two phytoplankton groups. May

was considered as a transition period with chlorophyll being equally split into winter-spring and summer phytoplankton groups. In June and July, the chlorophyll belonged to the summer phytoplankton group. August was another transitional period with chlorophyll being split into the summer and fall phytoplankton groups. Chlorophyll consisted of only fall phytoplankton in September and October and was split into winter-spring and fall phytoplankton groups in December. The carbon to chlorophyll ratios of phytoplankton were 40, 65 and 15 for winter-spring, summer and fall phytoplankton, respectively (HydroQual, 2000; HydroQual, 2003; Jiang and Zhou, 2004a; Tian et al., 2009).

The OA analysis was done using the OA software called OAX. This software was developed by Bedford Institute of Oceanography (Hendry and He, 1996). We used this method in the 2006-2007 BEM simulation (Tian et al., 2009). In the OAX, the covariance function (R) between data and estimation site is based on their pseudo-distance (r) determined as:

$$R(r) = (1 + r + \frac{r^3}{3})e^{-r} \tag{2.5}$$

$$r = \sqrt{\left(\frac{x_d - x_m}{a}\right)^2 + \left(\frac{y_d - y_m}{b}\right)^2 + \left(\frac{z_d - z_m}{c}\right)^2 + \left(\frac{t_d - t_m}{T}\right)^2} \tag{2.6}$$

where x ,y, z, and t are the four spatial and temporal coordinates; the subscripts d and m indicate data and model positions, respectively; and parameters a, b, c, and T are the de-correlation scales for their corresponding coordinate. Given the fact that the measurement sites were away from the open boundary and measurements were made on a monthly or bi-monthly basis, the OA analysis was done with relatively large de-correlation scales: 30 km in the horizontal, 15 m in the vertical and 45 days in time.

Examples of the OA-mapping results on the open boundary for April 15 and August 15 are presented in Figure 2.6. Given the low frequency of field observations and the large distance between the open boundary and the observation sites, particularly for the Southern Passage, the OA-mapped results should be interpreted with caution. Briefly, chlorophyll concentration was higher in April than in August and a slight subsurface chlorophyll maximum was observed on the April transect. Nutrients showed high concentrations in the deeper channel and low values in the surface layer. Similar to chlorophyll, DO concentration was higher in April than in August. In general, particulate organic substances were more abundant in April than in August, following the trend of chlorophyll and indicating that live phytoplankton contribute a considerable part to the particulate organic pools. Also particulate organic substances showed a vertical gradient, with higher values in the surface layer and lower values in bottom waters. Except for the high POP patch mentioned above, dissolved organic matter showed similar concentration levels on the April and August transects. DOC displayed a vertical distribution structure with higher values in the surface and lower values in the bottom. DON, on the other hand, had little vertical structure, particularly on the April transect. DOP was dominated by a high patch in the bottom of the south passage on the April transect, reflecting high levels of DOP measured in eastern Cape Cod Bay at that time of year.

3. Results

3.1 Physical Fields

3.1.1 Model-data comparisons

The BEM is designed to assess the water quality of Massachusetts Bay (MB). Since this system is highly controlled by the physical environment, available data were assimilated into the physical model MB-FVCOM to provide the best known physical fields for the water quality model. These data included the satellite-derived sea-surface temperature (SST) and all available hydrographic data. The model-data comparisons described here demonstrate how well MB-FVCOM, with these assimilated data, provides realistic physical fields.

Figures 3.1 and 3.2 show the comparison between model-predicted and observed temperature and salinity at MWRA monitoring stations F26, F27, F29, F31, N01 and N10. Stations F26 and 27 are located in the northern part of the study area close to the UG-RCA open boundary. Station F29 is located in the southern part of the study area close to the open boundary. Stations N01 and N10 are located in the central MB and F31 is within Boston Harbor. Assimilation of SST and hydrographic data made the model-predicted temperature and salinity match the observations well, but in some cases, data assimilation caused rapid adjustments in the simulated results.

Near the open boundary area (Stations F26, F27 and F29) and in central MB (N01 and N10), the water column was stratified from spring to early fall, with large temperature and salinity differences between the surface and bottom. At the harbor station F31, however, the water column was fully mixed through the entire year. At Stations N01 and N10, the bottom temperature exhibited substantial high-frequency (weekly) fluctuations.

Salinity displayed larger fluctuations near the surface than near the bottom. The variation was particularly high at Stations F26 and F27, signaling the impact of the freshwater discharge from the Merrimack River just north of MB.

Figure 3.3 shows the comparison between modeled surface temperature, salinity and currents and data collected at Buoy 44013 near the outfall. Surface temperature compares well between the data and simulation. High-frequency variations were observed in both temperature and salinity observations, indicating that similar variations in the model are not all caused by data assimilation, but by natural mechanisms such as horizontal advection and river discharges. Salinity data at the buoy are available only from June 1, 2009. A drop in surface salinity was observed late June and early July, which was not reproduced by the model. Current data are available only from July 1 to August 31, 2009. The simulated current was broadly compatible with the data in magnitude and direction. However, short-term discrepancies were observed, particularly in middle of July when the predicted current was briefly opposite to the observation. As shown later, mesoscale eddies are one dominating current feature in MBS. The timing and location of these eddies can cause deterioration in the model-data comparison at a fixed point.

Figures 3.4-3.8 compare the near-surface distributions of temperature and salinity. Note that the plots of observed data gather all the observations for the month. The plot for February includes the early February and the later February survey. Observations in the other months span at least three days, the shortest time it takes to complete a survey. The model plots gathered model results for the same time as each observed data point. After the observed data and modeled results were gathered for the month, they were contoured. The assimilation worked well to reproduce realistic fields of temperature and salinity. In February, there was a mostly homogeneous distribution of both temperature and salinity, with a slight inshore-offshore gradient in salinity (Figure 3.4). In April, temperature and salinity showed a southeast to northwest gradient: warmer and fresher in the harbor and northwestern MB, colder and saltier in southern MB and offshore (Figure 3.5). The model reproduced both magnitude and spatial pattern of the observations of both temperature and salinity. In June, the temperature and salinity distribution was similar to that in April, but with a higher temperature (Figure 3.6). The temperature was < 6 °C in April and about 16 °C in June. In August, the surface temperature reached 20 °C, but with higher values in the offshore region, opposite to the pattern in June and April (Figure 3.7). The simulated temperature was slightly higher than that observed; this is also seen at stations F31 and N10 in Figure 3.1. Given that the model is controlled – apart from data assimilation – by numerous forcings and internal dynamics such as insolation, heat fluxes and advection, slight deviation between simulation and observation is inevitable. In October, the surface temperature decreased considerably, to below 13 °C (Figure 3.8). Salinity showed a consistent pattern year round, with lower values in the harbor and coastal regions and relatively higher values in the offshore region and in southern MB.

3.1.2 Monthly averaged surface sub-tidal currents, temperature and salinity

The surface current in January was dominated by the coastal current flowing from the western Maine coast to the outer coast of Cape Cod (Figure 3.9). Current bifurcation and water intrusion into MB was not evident during January. In February, however, the coastal current bifurcated at the northern end of Stellwagen Bank with one branch flowing into MB. Water intrusion from the coastal current was strengthened further in March and May (Figures 3.9 and 3.10). From May through September, subtidal eddies prevailed in the surface current pattern (Figures 3.10 and 3.11). These eddies changed from month to month, but three of them were observed off and on throughout the summer season: one located on the east side of the coastal current off the North Passage, one located inside MB on the west side the coastal current and the third one located in the south region between MB and Cape Cod Bay. The distribution of monthly averaged currents in fall from October through December was back to the pattern of winter and spring, although the intensity of currents differs between the seasons.

To examine the seasonal variability of water properties, we present in Figures 3.12-3.17 the model-predicted temperature and salinity field near the surface at the end of each month. In section 3.1.1, we have shown that the water is seasonally well-stratified in Massachusetts Bay except in the shallow area of Boston Harbor. The monthly fields showed that water temperature was not spatially uniform in the Bay. The surface temperature was the coldest in January and February, with temperature ranging from 2 °C within the bay to 4 °C in the offshore region (Figure 3.12). Surface temperature started to rise in March, ranging from 3 to 5 °C, but a gradient formed with warmer water in the southern part of the domain and cooler water in northern end of the domain. Surface

temperature within the bay remained lower than that in the offshore region. In April, the gradient in surface temperature had changed direction, with higher values within the bay and in the north-coastal region and lower values in the offshore region. Temperature at this time rose to 7–9 °C. The surface water temperature distribution in May and June was characterized by a high-temperature patch in Cape Cod Bay where temperature reached 13 °C in May and 16 °C in June, whereas it remained around 12 °C in the northern offshore region (Figure 3.13). In July, surface water temperature reached 20 °C in Cape Cod Bay and warm surface waters extended over the entire Bay. In August, however, cooler water appeared at the northern end of the simulation domain. Waters with temperatures as low as 16 °C occupied a great part of the northern domain and extended into MB. A well defined temperature front formed within the bay as well as in the offshore region, with warmer water south and southeast of the front and cooler water north and northwest of the front. Surface water temperature decreased considerably in September, ranging from 14 to 18 °C within the simulation domain (Figure 3.14). In October, surface water temperature decreased to 9–11 °C. Unlike the previous two months when cold water reached the western end of the bay and even within Boston Harbor, the cold water mass in October was limited to the eastern side of the bay. As such, a well defined temperature front was formed running northwest-southeast within the bay. In November, the south-north gradient in surface water temperature weakened but persisted. In December, however, the temperature gradient was reversed, with lower values in Cape Cod Bay and higher values in the offshore region.

Salinity in January and February showed little spatial variation (Figure 3.15). Low salinity surface waters were perceptible only near the mouth of the Merrimack River and in Boston Harbor. In March, the lower salinity water extended to the northeastern end of MB and in April, fresher waters occupied a great part of the northern bay. Salinity in Cape Cod Bay had decreased as well. In May and June, lower salinity waters occupied a large part of the bay and the coastal region in the western Gulf of Maine (Figure 3.16). A similar pattern was found in July, with fresher water extending even to the northern offshore region of the MB-FVCOM simulation domain. The August salinity pattern was similar except that the patch of lower salinity water was contained within MB. From September through December, surface water salinity continued to increase in MB with the low salinity patch shrinking. Salinity finally reached its winter status in December, similar to January and February (Figure 3.17).

3.2 Water quality fields

3.2.1 Data-model comparison

Data-model correlation analyses of key variables are presented in Figure 4.18, including surface chlorophyll, NO_3, SiO_3, NH_4, and bottom DO and DO saturation. Good correlations were found between the modeled and observed results for NO_3^- near the surface and DO near the bottom. For the near-surface chlorophyll, the correlation is not as good as that for nitrate and DO. Basically the model tended to overestimate chlorophyll at low concentrations and underestimate chlorophyll at high concentrations. The model-data correlation for the surface silicate was reasonably good (r=0.71), while ammonium data were relatively more scattered than other variables. Unlike the dissolved oxygen concentration, for which a good correlation was found between the model prediction and observation, the model tended to underestimate the saturation of dissolved oxygen. The saturation of dissolved oxygen was not directly modeled, rather it is calculated based on

temperature, salinity and DO data. Biases in the simulation of these different parameters could all influence the accuracy of DO saturation estimates.

Annual cycles of key variables were plotted with the observational data for visual comparison (Figures 3.19-3.33). Chlorophyll concentration was broadly similar between the simulation and observation, but higher values observed at certain stations were not reproduced by the model, for example see N01 in Figure 3.19 and Station 139 in Figure 3.21. A general pattern in the chlorophyll distribution in the simulation indicates an absence of the fall phytoplankton bloom in MB in 2009. This model prediction is supported by the observations at most of the monitoring stations, except in the near-field where high chlorophyll concentration was observed (Figure 3.19). The absence of a fall bloom in 2009 was observed and predicted at most of the monitoring stations, but anomalous phytoplankton growth close to the outfall may have occurred in the fall that was not predicted by the model. Libby et al. (2010) reported blooms of diatoms *Skeletonema* and *Dactyliosolen* during the fall season in 2009 at near-field stations. Such blooms of individual species can not be resolved by the RCA model. However, when the data were averaged over depth and over all stations in the near-field or other regions, Libby et al. (2010) found that depth-averaged chlorophyll remained at low level during fall 2009 except at the deepest stations (Libby et al., 2010, their figure 2-4). Looking more closely at the monitoring data and also data from the moorings near the outfall and off Cape Ann, there was a brief episode of high chlorophyll in late September, at least near the outfall and off Cape Ann. Then levels dropped sharply by mid October bit rebounded in mid-November. October 2009 was particularly cool, cloudy, and rainy. The far-field survey coincided with the October dip in chlorophyll, and stations near the boundary are sampled only on the far-field surveys.

Boston Harbor (BH) shows a different seasonal cycle in the chlorophyll concentration as compared to MB. In BH, the chlorophyll concentration remained relatively high from spring to fall so that peaks in chlorophyll concentration in spring and fall are less clear (Figure 3.21). As mentioned in Tian et al. (2009), the shallow depth and multiple anthropogenic and natural nutrient sources contribute to the sustained high primary production in the harbor during the summer. Taylor et al. (2010) did a comparison of multi-year averaged seasonal cycles of major water quality variables. They found that even though chlorophyll levels remain relatively high during the summer season in Boston Harbor, chlorophyll decreased after the diversion of the MWRA outfall from the harbor to the offshore location.

At most of the monitoring stations, model-estimated and observed dissolved inorganic nitrogen (DIN) showed similar seasonal variation both near the bottom and at the surface (Figures 3.22 and 3.24). Typically, DIN was replenished during the winter mixing season. DIN depletion in surface waters was observed in March and April when DIN concentration decreased to a very low level due to the consumption by the spring phytoplankton bloom. DIN remained at a low level through summer and early fall and replenished again in late fall and winter. In contrast to surface waters, DIN in the bottom layer stayed at a relatively high level all through the summer and fall seasons, indicating a stratification in DIN concentration at most of the monitoring stations. Model-simulated primary production was depicted at three monitoring stations where field observations were often conducted (primary production data were not available for 2009 at the time this report was prepared) (Figure 3.25). Primary production did not show typical peaks for spring and fall blooms, but rather remained at a relatively high level throughout the summer season. Primary production at

the aforementioned near-field station N18 was not particularly lower than that at other stations, but it decreased to a low level during the fall season at all the stations. As a general observation, nutrient concentration is considerably higher in the bottom layer than in the surface layer at most of the monitoring stations during summer, indicating that stratification affected nutrient redistribution in the water column during the summer season in 2009. However, the difference varies from station to station. The surface-bottom difference in nutrient concentration is the largest at the outfall site and Station N18, which may reflect an influence from the outfall. The surface-bottom differences in nutrient concentration were also relatively larger at other near-field stations (e.g., Stations N01, N04 and N07 in Figure 3.22) than at the far-field stations (Figure 3.23). Particularly at Station F01 located in Cape Cod Bay, the difference in nutrient concentration between the surface and bottom layers appears to be minimal. At the far-field station F22 (Figure 3.22), on the other hand, nutrient concentration is noticeably higher in the bottom layer than in the surface layer, with a difference comparable with that found at the near-field stations.

Most of the DON and PON data were reproduced by the model (Figures 3.26-3.31) except for particularly high observed DON values (e.g., DON at Station N01 in Figure 3.26) and some of the lower PON values. DON showed very little seasonal variation, in contrast to PON which manifested relatively high values during the spring phytoplankton bloom and low values during the winter mixing season. Also PON concentration gradually decreased from the peak formed during the spring phytoplankton bloom to low levels in winter. Approximately following the chlorophyll distribution, predicted PON did not display a second peak in the fall, probably due to the weak fall phytoplankton bloom. No anomalous signal was found near the outfall in either DON or PON, showing that the organic nitrogen pools are essentially controlled by internal dynamics within the water column and the outfall effluent did not noticeably alter their distribution. POC displayed high frequency variations (Figures 3.30 and 3.31). The seasonal cycles of POC differed from that of chlorophyll. During the spring phytoplankton bloom where chlorophyll concentration was relatively high, POC was relatively lower. During the summer season when chlorophyll was relatively low, POC remained at a relatively high level. During the fall when no phytoplankton bloom was simulated, POC continued to be as high as during the summer season. This discrepancy implies that biogenic detritus constituted a considerable portion of model POC as compared to living phytoplankton cells, at least in determining the seasonal variations in POC. At near-field stations, the model tended to overestimate the concentration of POC, particularly in the bottom layer. Model-data comparison appeared to be better at certain far-field stations in terms of magnitude, but both the data and simulation are characterized by high frequency variations with relatively little seasonal pattern.

Relatively good comparison of DO has been obtained between simulation and observation (Figures 3.32 and 3. 33). The model slightly underestimated the DO level at the near-field stations, but the difference remained minimal compared to the total concentration. DO displayed high values during the spring phytoplankton bloom, but stayed at a low level during the summer and fall season. As pointed out by Tian et al. (2009), the high DO values in spring reflected photosynthesis production through phytoplankton growth, whereas remineralization of organic substances occurred in summer and fall so that DO stayed low during that period of time. Water mass inflow through the open boundary and horizontal advection can also alter bottom DO concentration in the region (Libby et al., 2008).

Time-series of key variables (temperature, DIN, chlorophyll and DO) throughout the water column are shown in Figures 3.34-3.38. The model reproduced the observed homogeneous water column in winter and stratification in summer and early fall in the temperature profile. The lowest temperature of about 2-4 °C was reached in February and stratification started around early April. The strongest stratification occurred in July with a mixed layer depth ranging from 5-10 m. At shallow station F23, the water column tended to be homogenized most of the time. Only in August did the temperature field show weak stratification at this station. Destratification took place at the end of October throughout MB, and a homogeneous water column continued through November and December.

DIN displayed a similar seasonal cycle between the model and the data: replenished in winter throughout the whole water column, depleted fully in spring and early summer, regenerated through remineralization and input from the sediment to the bottom layer, and vertically mixed again in late fall and winter. The model seemed to overestimate DIN in winter at station F23 and F02, but few data were collected during the winter season. Given the low frequency of sampling, interpolation and extrapolation can considerably deteriorate the data mapping.

Time-series mapping of chlorophyll shows the spring phytoplankton bloom as the dominant feature. As mentioned earlier, the fall phytoplankton bloom was not well developed in the 2009 simulation so that no high chlorophyll concentration was mapped in the modeled time series. DO matched well in general between the model and observation in terms of seasonal cycle and magnitude. The highest values of DO were observed and modeled during the spring phytoplankton bloom and the lowest values appeared in the bottom layer in summer when remineralization consumption and sediment oxygen demand were highest within an annual cycle. The model seems to overestimate DO during the spring phytoplankton bloom and also in the bottom layer at the end of September and early October. Given the low frequency of field observations, the time-series mapping of observed should be interpreted with caution, especially in winter.

Sediment nutrient fluxes and oxygen demand (SOD) were observed (Tucker et al., 2010) at three stations in BH (BH02, BH03 and BH08A) and three stations in Massachusetts Bay (MB01, MB03 and MB05) (Figure 2.4). At the bay stations shown at the right side of the figure, the model-data comparison results were reasonably good, with little seasonal variation (Figures 3.39 and 3.40). In contrast, nutrient fluxes and SOD were substantially higher during summer and early fall at the harbor stations as compared with the bay stations, indicating that remineralization contributed a substantial share to the increased nutrient supplies in summer in BH. The model simulation results compared relatively well with the observations for most sediment fluxes in BH, except at BH02 where the model underestimated the SOD flux in summer.

In summary, the UG-RCA 2009 simulation reproduced most of the observed magnitudes and seasonal variations of an array of parameters. For some specific cases, however, model-data deviation was observed, such as an overestimation of surface DIN at near-field stations, underestimation of DO concentrations at most stations, and underestimation of harbor sediment oxygen demand. Also, the model did not predict a fall bloom in 2009 although high (but variable) chlorophyll values were reported at near-field stations.

3.2.2 Comparison with previous year simulations

In this section we compare the UG-RCA simulations of 2006, 2008 and 2009, which were carried out by using the same model (2007 was simulated using the ECOM-si-RCA system.) Two contrasting phenomena can be observed in the 2009 chlorophyll simulation as compared to that of 2006 and 2008 (Figure 3.41). First, the spring phytoplankton bloom was later in 2009 than in 2006 and 2008. The spring bloom occurred around the end of April and early May in 2009 whereas it was observed in late March and early April in 2006 and 2008. That is, the 2009 spring phytoplankton bloom was later by about one month when compared to that in 2006 and 2008. The amplitude of the spring bloom was, however, comparable among the three years. Second, the fall phytoplankton bloom was well developed in 2006 and 2008, but absent in the 2009 model simulation. The fall bloom occurred near the end of October and early November in 2006 and 2008, but the chlorophyll concentration remained at a lower summertime level in 2009. Libby et al. (2010) averaged chlorophyll concentration within different regions and found that the fall bloom in 2009 was very weak or absent in most areas. Only at the northern open boundary did depth-averaged chlorophyll noticeably increase in fall.

The DIN seasonal cycle was generally similar among the three years, with high values in winter, low values in summer and replenishment in late fall (Figure 3.42). Nonetheless, slight differences can be seen from year to year. DIN concentration was lower in winter and fall 2006 than in 2008 and 2009 during the same period of time. Concerning 2009, specifically, the spring drop in DIN was later in 2009 than in 2006 and 2008, which is consistent with the later spring phytoplankton bloom in the same year. Also, DIN concentration at the end of October was relatively higher in 2009 than in 2006 and 2008, in agreement with the fact that the fall bloom was not well developed in 2009.

For bottom DO, no substantial difference was observed between the three years (Figure 3.43). DO displayed high values during the spring phytoplankton bloom and low values in late summer and early fall over all three years. The DO level was quite similar at the end of the annual simulation in 2006 and 2009, while 2008 showed a late-year increase and ended slightly higher.

4. Projection Experiments

We conducted a model run without MWRA effluent to assess the potential influence of the MWRA outfall on the water quality and ecosystem function in Massachusetts Bay. In this section, we refer the initial run with the MWRA outfall as the "control run" and the sensitivity-analysis run as the "non-sewage" run. We compared the chlorophyll concentration, dissolved inorganic nitrogen and DO between the two simulations. The intensities and seasonal variations of the chlorophyll concentration for these two runs were almost identical (Figure 4.1). Even though the two simulation lines were not fully superposed on each other, the difference between the runs remained negligible throughout the year.

The seasonal cycle of DIN near the surface also was similar between the two simulations (Figure 4.2). The results were almost the same in summer. A noticeable difference was found in winter, during which the "non-sewage" run predicted lower DIN concentration than the control run with the MWRA outfall. Near the bottom, the non-sewage run predicted a notably lower DIN concentration than the control run near the outfall and inshore, whereas the two predictions were more comparable at other stations (Figure 4.3). The DO results were practically identical between the two simulations (Figure 4.4). Although the time series of the DO concentration were not fully superposed, the difference between the non-sewage and control runs remained almost indistinguishable.

However, in the bottom model layer, we do find a notable difference between the two runs in terms of ammonium, which is the most abundant nutrient in the outfall sewage discharge (Figures 4.5-4.7). In January, ammonium from the outfall was restricted to the northeastern corner of the simulation domain including Boston Harbor (Figure 4.5). In February and March, the effluent ammonium was dispersed down to Cape Cod Bay (CCB), essentially along the west coast of MB. The outfall's influence on bottom-layer ammonium can be seen over the entire CCB at the end of February and in March. At the end of February, ammonium concentration was even higher in CCB than on the west coast of MB, indicating that effluent ammonium can be trapped within CCB. From May through October, effluent ammonium was again restricted to the local area around the outfall, with a peak concentration observed in August (Figures 4.6 and 4.7). During late fall in November and December, effluent ammonium was dispersed down to CCB again. Certainly, effluent dispersal is controlled by the current system which can vary over time subject to wind forcing and cold water intrusion from the Western Maine Coastal Current. If we consider ammonium as a semi-conservative tracer of effluent, the two long-distance dispersions in 2009 occurred in winter and late fall when the stratification was weak and even absent. In summary, the effluent is in most cases restricted horizontally within a local domain of about 20 km wide around the outfall location. However, based on the model prediction, long-distance dispersion can occur under particular circumstances, with nutrients transported as far as CCB.

We plotted data along a west-east transect across the outfall for the end of each month (Figures 4.8 and 4.9). The height of the effluent plume, as inferred from the ammonium concentration, varied from month to month. In January and February, the outfall plume reached to the surface (Figure 4.8). From March through September, however, the plume was mostly restricted to the bottom 10 m or so. This projection is in approximate agreement with the rise height of 5-15 m

predicted by Blumberg et al. (1996) using near-field and far-field models. The core of the plume remained contained with the bottom layers from October through December, but its influence was perceptible up to the surface (Figure 4.9). As the plume can spread along the slope of the topography toward the coast, the absolute depth of the plume changes from place to place. The surfacing of the plume occurred during months of weak stratification, indicating that the vertical mixing basically controls the upward spread of the outfall effluent.

Libby et al. (2009b) did a comparison between data collected before and after the September 6 2000 diversion of the MWRA outfall from Boston Harbor to the MB. Higher ammonium concentration after the diversion was found at the near-field stations. However, field measurements are not directly comparable to the model projection shown here. Field measurements before the diversion were conducted when the outfall was located in Boston Harbor, whereas the non-sewage run here was configured without any effluent discharge into the system. The difference between data collected before and after the relocation of the outfall has the potential to obscure the direct influence of the outfall on effluent concentration and distribution given that it consists of the difference between two sewage discharge regimes. Also, the data comparison in Libby et al. (2009b) was based on the ammonium averaged over depth, region, and season, whereas here we output the instantaneous difference in the bottom layer, which represents the maximum difference predicted by the model.

This is the first time that the comparison between the control and the non-sewage runs has been conducted systematically over 12 months and over the entire simulation domain. Tian et al. (2009) and Chen et al. (2010) also conducted projection runs, but their analysis was based on the difference at 15 meters in the water column, and only in April and August when the effluent ammonium is mostly trapped in the bottom layer according to the present study. Projections before 2008 were conducted with a different physical model, ECOM-si. Inter-model differences should be taken into account in comparing various non-sewage projections, but the results of the present study are broadly consistent with past projections.

As shown at the beginning of this section, no anomaly was observed in chlorophyll or DO levels corresponding to the ammonium distribution around the outfall. In fact, during the stratified season when light is available, the effluent was basically trapped within the bottom layers around the outfall. During the well-mixed season when effluent could effectively reach the surface, both light and vertical mixing were unfavorable to phytoplankton growth. As a result, the nutrient discharge from the outfall did not seem to result in biomass and DO anomalies.

5. Summary

The 2009 simulation was conducted using MB-FVCOM/UG-RCA. The surface forcing was essentially based on meteorological data collected at Buoy 44013 and weather model predictions; nutrient loadings were based on the MWRA monitoring data and river discharges; and open boundary conditions were established from the data collected during the MWRA monitoring program.

The UG-RCA 2009 simulation reproduced most of the magnitudes and seasonal variations of the observations. For some specific cases, a deviation between simulation and data was observed, such as underestimation of DO in surface waters during the spring phytoplankton bloom.

The seasonal variation of model-predicted water quality variables was dominated by spring phytoplankton blooms that were reflected by high chlorophyll concentration, which depleted nutrients near the surface in spring; surface nutrients remained at low levels until the fall. Two contrasting phenomena were observed in 2009 as compared to the previous years. First, the spring phytoplankton occurred about one month later in 2009 than in 2006 and 2008. Secondly, no fall phytoplankton bloom was predicted in 2009 whereas it was well developed in the previous years.

DO showed high values during the spring phytoplankton bloom due to photosynthetic production, but remained at a low level in fall, kept low by high DO consumption and low DO solubility under high temperature.

Based on our projection analysis of removing the MWRA outfall from the simulation, we determined the horizontal and vertical extent of the outfall effluent plume using ammonium as a proxy. In the horizontal scale, the plume was mostly restricted to a local area around the outfall within about 20 km. However, long-distance effluent dispersal as far as down to Cape Cod Bay was predicted under certain circumstances in March and December 2009. In the vertical, the height of the plume was essentially controlled by vertical dynamics and mixing in the water column. In winter and late fall when the vertical mixing was strong, the outfall effluent plume can reach to the surface layer. During the stratified season in summer and early fall, the ammonium plume was basically constrained within the bottom 10 m. However, no substantial bay-wide influence was observed in chlorophyll and DO. We believe that the timing of the effluent spreading influences its effect on the function of the ecosystem. As the upward mixing and long-distance dispersal occurred during winter and late fall when light intensity limits phytoplankton growth, effluent nutrients were not effectively taken up and translated into phytoplankton biomass and subsequent biogeochemical cycles.

6. References

Alber M. and Chan A. 1994. Sources of contaminants to Boston Harbor: revised loading estimates. Boston: Massachusetts Water Resources Authority. Report 1994-01, 113pp.

Banks R.B. and Herrera F.F. 1977. Effect of wind and rain on surface reaeration. *J. Envir. Engr. Div., ASCE*. **103**: 489-504.

Bigelow H.B. 1927. Physical oceanography of the Gulf of Maine (Part II). *Bulletin of the Bureau of Fisheries*, **40**: 511-1027.

Blumberg A., Ji Z. and Ziegler C.K., 1996, Modeling outfall plume behavior using a far field model, *J. Hydraulic Engineering*, **112**: 610-616.

Burchard H., Bolding K., Rippeth T.P., Stips A., Simpson J.H. and Sündermann J. 2002. Microstructure of turbulence in the Northern North Sea: a comparative study of observations and model simulations. *J. Sea Res.*, **47**: 223–238.

Butman B. 1976. Hydrography and low frequency currents associated with the spring runoff in Massachusetts Bay. *Memoires. Societe Royale des Sciences de Liege*, **6**: 247-275.

Butman B., Bothner M.H., Lightsom F.L., Gutierrez B.T., Alexander P.S., Martini M.A. and Strahle W.S. 2002. Long-term Oceanographic Observations in Western Massachusetts Bay offshore of Boston, Massachusetts: Data Report for 1989-2000, U.S. Geological Survey Digital Data Series 74.

Chen C., Liu H. and Beardsley R. 2003. An unstructured grid, finite-volume, three dimensional, primitive equations ocean model: Application to coastal ocean and estuaries. *Journal of Atmospheric and Ocean Technology*, **20 (1)**: 159–186.

Chen C., Beardsley R.C., Hu S., Xu Q. and Lin H. 2005. Using MM5 to hindcast the ocean surface forcing fields over the Gulf of Maine and Georges Bank region. *Journal of Atmospheric and Ocean Technology*. **22**: 131-145.

Chen C., Beardsley R.C. and Cowles G. 2006a. An unstructured grid, finite-volume coastal ocean model (FVCOM) system. Special Issue entitled "Advance in Computational Oceanography", *Oceanography*, **19(1)**: 78-89.

Chen C., Beardsley R.C. and Cowles G. 2006b. An unstructured grid, finite-volume coastal ocean model-FVCOM user manual, School for Marine Science and Technology, University of Massachusetts Dartmouth, New Bedford, Second Edition. SMAST/UMASSD Technical Report-06-0602, 318 pp.

Chen C., Malanotte-Rizzoli P., Wei J., Beardsley R.C., Lai Z., Xue P., Lyu S., Xu Q., Qi J. and Cowles G.W. 2009. Application and comparison of Kalman filters for coastal ocean problems: An experiment with FVCOM, *J. Geophys. Res.*, **114**, C05011, doi:10.1029/2007JC004548.

Chen C., Tian R., Beardsley R.C., Qi J. and Xu Q. 2010. Modeling 2008 in Massachusetts Bay using an upgraded unstructured-grid Bays Eutrophication Model. Boston: Massachusetts Water Resources Authority. Report 2010-15. 127p.

Di Toro D.M. 2001. *Sediment Flux Modeling*. Wiley-Interscience, New York, 624 pp.

Fairall C.W., Bradley E.F., Rogers D.P., Edson J.B. and Young G.S. 1996. Bulk parameterization of air–sea fluxes in TOGA COARE. *J. Geophys. Res.*, **101**: 3747–3767.

Fairall C.W., Bradley E.F., Hare J.E.,Grachev A.A. and Edson J.B. 2003. Bulk Parameterization of Air–Sea Fluxes: Updates and Verification for the COARE Algorithm. *Journal of Climate* 2003; **16:** 571-591.

Gao G., Chen C., Qi J. and Beardsley R.C. 2010. Development of Unstructured-grid Version CICE: Validation and Applications, Submitted to *J. Geophys. Res.*

Geyer W.R., Gardner G.B., Brown W.S., Irish J., Butman B., Loder T. and Signell R.P. 1992. Physical oceanographic investigation of Massachusetts and Cape Cod Bays. Boston: Massachusetts Bays Program. MBP-92-03, 497pp.

Hendry R. and He I. 1996. Technical report on objective analysis (OA) project, Bedford Institute of Oceanography, Dartmouth, Nova Scotia, 105pp.

HydroQual, Inc. and Normandeau Associates, Inc. 1993, A water quality model for Massachusetts and Cape Cod Bays. Boston: Massachusetts Water Resources Authority. Report 1993-05, 222pp.

HydroQual, Inc. and Normandeau Associates, Inc. 1995. A water quality model for Massachusetts and Cape Cod Bays: Calibration of the Bay Eutrophication Model (BEM). Boston: Massachusetts Water Resources Authority. Report 1995-08. 402 pp.

HydroQual, Inc. 2000. Bays Eutrophication Model (BEM): modeling analysis for the period 1992-1994. Boston: Massachusetts Water Resources Authority. Report 2000-02, 158pp.

HydroQual, Inc. 2001a. Boundary sensitivity for the Bays Eutrophication Model (BEM). Boston: Massachusetts Water Resources Authority. Report 2001-14. 90pp.

HydroQual. 2001b. Analysis of the addition of a third algal group to the Bays Eutrophication Model (BEM) kinetics. Boston: Massachusetts Water Resources Authority. Report 2001-15. 110 p.

HydroQual, Inc. and Signell R.P. 2001. Calibration of the Massachusetts and Cape Cod Bays Hydrodynamic Model: 1998-1999. Boston: Massachusetts Water Resources Authority. 2001-12, 170pp.

HydroQual. 2002. Sensitivity of the Bays Eutrophication Model (BEM) to changes in algal model coefficients. Boston: Massachusetts Water Resources Authority Report 2002-16. 236 p.

HydroQual, Inc. 2003. Bays Eutrophication Model (BEM): modeling analysis for the period 1998-1999. Boston, Massachusetts Water Resources Authority. Report 2003-03, 318pp.

HydroQual, 2004. "User's Guide for RCA, Release 3.0", Hydroqual, Inc, New Jersey.

Hyer P.V., Fang C.S., Ruzeck E.P. and Hargis W.J. 1971. Hydrography and hydrodynamics of Virginia estuaries, studies of the distribution of salinity and dissolved oxygen in the upper York system. Gloucester Point, VA:Virginia Institute of Marine Science.

Jiang M.S. and Zhou M. 2004a. Calibration of the Massachusetts and Cape Cod Bays water quality model: 2000-2001. Boston: Massachusetts Water Resources Authority. Report 2004-09. 90pp.

Jiang M.S. and Zhou M. 2004b. Calibration of the Massachusetts and Cape Cod Bays Hydrodynamic Model: 2000-2001. Boston: Massachusetts Water Resources Authority. Report 2004-08. 71pp.

Jiang M. and Zhou M. 2006a. The Massachusetts and Cape Cod Bays hydrodynamic model: 2002-2004 simulation. Massachusetts Bay Eutrophication Model: 2002-2004 Simulation. Boston: Massachusetts Water Resources Authority. Report 2006-12. 128 p.

Jiang M. and Zhou M. 2006b. Massachusetts Bay Eutrophication Model: 2002-2004 Simulation. Boston: Massachusetts Water Resources Authority. Report 2006-13. 126 p.

Jiang M. and Zhou M. 2008. Massachusetts Bay Eutrophication Model: 2005 simulation. Boston: Massachusetts Water Resources Authority. Report 2008-13. 82 p. Report 2008-12., 118pp.

Kropp R.K., Diaz R., Hecker B., Dahlen D., Boyle J.D., Abramson S.L. and Emsbo-Mattingly S. 2001. 2000 Outfall Benthic Monitoring Report. Boston: Massachusetts Water Resources Authority. Report 2001-14, 148pp.

Kropp R.K., Diaz R., Dahlen D., Boyle J.D. and Hunt C.D. 2002. 2001 Harbor Benthic Monitoring Report. Boston: Massachusetts Water Resources Authority. Report 2002-19, 74pp.

Lai Z., Chen C., Cowles G. and Beardsley R.C. Submitted. A Non-Hydrostatic Version of FVCOM, Part I: Validation Experiments (submitted to *Journal of Geophysical Research-Oceans*, in revision).

Laws E.A. and Chalup M.S. 1990. A microalgal growth model. *Limnol. Oceanogr.* 35, 597-608.

Libby P.S., Hunt C.D, Geyer W.R., Keller A.A., Oviatt C.A. and Turner J.T. 2000. 1999 Annual Water Column Monitoring Report. Boston: Massachusetts Water Resources Authority. Report 2000-09, 180pp.

Libby P.S., Hunt C.D, McLeod L.A., Geyer W.R., Keller A.A., Borkman D., Oviatt C. A. and Turner J. T. 2001. 2000 Annual Water Column Monitoring Report. Boston: Massachusetts Water Resources Authority. Report 2001-17, 196pp.

Libby P.S., Borkman D.G., Geyer W.R., Keller A.A., Turner J.T., Mickelson M.J., and Oviatt C.A. 2008. Water Column Monitoring in Massachusetts Bay: 1992-2007. Boston: Massachusetts Water Resources Authority. Report 2008-16, 170pp.

Libby P.S., Anderson D.M., Borkman D.G., Geyer W.R., Keller A.A., Oviatt C.A. and Turner J.T. 2009a. 2008 Water Column Monitoring Results. Boston: Massachusetts Water Resources Authority. Report 2009-12. 31p. plus appendices.

Libby P,S,, Borkman D,, Geyer W,R,, Keller A,A,, Turner J,T,, Mickelson M,J, and Oviatt C,A. 2009b. Water column monitoring in Massachusetts Bay 1992-2007: focus on 2007 results. Boston: Massachusetts Water Resources Authority. Report 2009-04. 162 p. (incl. appendices).

Libby P.S., Borkman D.G., Geyer W.R., Turner J.T. 2010. 2009 Water Column Monitoring Results. Boston: Massachusetts Water Resources Authority. Report 2010-13. 36p + appendices.

Lynch D.R., Naimie C.E. and Werner F.E. 1996. Comprehensive coastal circulation model with application to the Gulf of Maine. *Cont. Shelf Res.*, 12: 37-64.

Maciolek N. J., Diaz R. J., Dahlen D., Hecker B., Gallagher E. D., Blake J. A., Williams I. P., Emsbo-Mattingly S., Hunt C. and Keay K. E. 2003. 2002 Outfall Benthic Monitoring Report. Boston: Massachusetts Water Resources Authority. Report 2003-13, 166pp.

Manohar-Maharaj V. 1973. Spring run off in to Massachusetts Bay. Master Thesis, MIT, Cambridge, 97p.

Mellor G. L. and Yamada T. 1982. Development of a turbulence closure model for geophysical fluid problems. *Rev. Geophys. Space Phys.*, **20**: 851-875.

Menzie-Cura. 1991. Sources and loadings of pollutants to Massachusetts Bays. Boston: Massachusetts Bays Program. Report MBP-91-01, 266pp.

Pietrzak J., Jakobson J.B., Burchard H., Vested H.J. and Peterson O. 2002. A three-dimensional hydrostatic model for coastal and ocean modeling using a generalized topography following coordinate system. *Ocean Modelling* **4**:173–205.

Qi J., Chen C., Beardsley R.C., Perrie W. and Cowles G. 2009. An unstructured-grid finite-volume surface wave model (FVCOM-SWAVE): implementation, valida.tions and applications. *Ocean Modelling*, **28**: 153-166. doi:10.1016/j.ocemod.2009.01.007.

Signell, R.P., Jenter, H.L. and Blumberg, A.F., 2000, Predicting the physical effects of relocating Boston's sewage outfall, *J. Estuarine, Coastal and Shelf Sci.*, **50**: 59-72.

Smagorinsky J. 1963. General circulation experiments with the primitive equations, I. The basic experiment. *Monthly Weather Review*, **91**: 99–164.

Taylor D.I., Oviatt C.A. and Borkman D.G. 2010. Non-linear Responses of a Coastal Aquatic Ecosystem to Large Decreases in Nutrient and Organic Loadings. *Estuaries and Coasts*:1-13. DOI 10.1007/s12237-010-9312-3.

Tian, R.C., Chen C.S., Xu Q.C., Xue P.F., Cowles G.W., Beardsley R. and Rothschild B. 2009. Massachusetts Bay Eutrophication Model: 2006-2007 Simulation. Boston: Massachusetts Water Resources Authority. Report 2009-11. 147p.

Tucker J., Kelsey J., Giblin A. and Hopkinson C. S. 2002. Benthic Metabolism and Nutrient Cycling in Boston Harbor and Massachusetts Bay: Summary of Baseline Data and Observations after One Year of Harbor-to-Bay Diversion of Sewage Effluent. Boston: Massachusetts Water Resources Authority. Report 2002-13, 83pp.

Tucker J., Kelsey S. and Giblin A.E. 2010. 2009 Benthic nutrient flux annual report. Boston: Massachusetts Water Resources Authority. Report 2010-10. 27 p.

Turner J.T. 1994. Planktonic Copepods of Boston Harbor, Massachusetts Bay and Cape-Cod Bay, 1992. *Hydrobiologia*, **293**: 405-413.

Table 2. 1 State variable numbers and units in UG-RCA.

Number	Variable	Unit
1	Salinity	ppt
2	Winter/spring phytoplankton	mg C l^{-1}
3	Summer phytoplankton	mg C l^{-1}
4	Fall phytoplankton	mg P l^{-1}
5	Particulate organic phosphorous – refractory component	mg P l^{-1}
6	Particulate organic phosphorous – labile component	mg P l^{-1}
7	Dissolved organic phosphorous – refractory component	mg P l^{-1}
8	Dissolved organic phosphorous – labile component	mg P l^{-1}
9	Total dissolved inorganic phosphorous	mg N l^{-1}
10	Particulate organic nitrogen – refractory component	mg N l^{-1}
11	Particulate organic nitrogen – labile component	mg N l^{-1}
12	Dissolved organic nitrogen – refractory component	mg N l^{-1}
13	Dissolved organic nitrogen – labile component	mg N l^{-1}
14	Total ammonia (ammonia in water and phytoplankton cell)	mg N l^{-1}
15	Nitrite + nitrate	mg Si l^{-1}
16	Biogenic silica	mg Si l^{-1}
17	Total silica – (silica in water and phytoplankton cell)	mg C l^{-1}
18	Particulate organic carbon – refractory component	mg C l^{-1}
19	Particulate organic carbon – labile component	mg C l^{-1}
20	Dissolved organic carbon – refractory component	mg C l^{-1}
21	Dissolved organic carbon – labile component	mg C l^{-1}
22	Dissolved organic carbon – algal exudate	mg C l^{-1}
23	Dissolved organic carbon – reactive component	mg C l^{-1}
24	Particulate organic carbon – reactive component	mg C l^{-1}
25	O2* - aqueous oxygen	mg O_2 l^{-1}
26	Dissolved oxygen	mg O_2 l^{-1}

Table 2. 2 Parameter definition, symbols, values and units in RCA-v3 and UG-RCA, and in RCA-v2. Where values used in RCA differ from those used in UG-RCA, they are shown in parentheses.

Order	Parameter definition	Symbol	Value	Unit
1	MODEL OPTION	AGMOPT	1	
2	Phytoplankton categories	ACTALG	3	
3	REAERATION FORMULATION	KAOPT	3	
4	EXTINCTION COEFFICIENT	KEOPT	1	
5	PAR FRACTION	PAR	0.437	
9	GROWTH TEMPERATURE FOR DIATOMS	TOPT1	8.000	^oC
10	TEMPERATURE CORRECTION EFFECT ON GROWTH RATE BELOW TOPT1	K1BETA1	0.004	$^oC^{-2}$
11	TEMPERATURE CORRECTION EFFECT ON GROWTH RATE ABOVE TOPT1	K1BETA2	0.006	$^oC^{-2}$
12	GROSS PHOTOSYNTHETIC RATE PER UNIT CELL (ASSOCIATED WITH PHOTOSYNTHETIC DARK REACTIONS)	GPRE1	2.5	d^{-1}
13	GROSS PHOTOSYNTHETIC RATE PER UNIT CELL PER UNIT LIGHT INTENSITY UNDER NUTRIENT-SATURATED CONDITIONS AND ZERO IRRADIANCE	GPR01	0.64 (0.28)	m^2 Ein^{-1}
14	SATURATING ALGAL LIGHT INTENSITY	IS1	0.000	Ein m^{-2} d^{-1}
15	HALF SATURATION CONSTANT FOR NITROGEN	KMN1	0.010	mg N l^{-1}
16	HALF SATURATION CONSTANT FOR PHOSPHOROUS	KMP1	0.001	mg P l^{-1}
17	HALF SATURATION CONSTANT FOR SILICA	KMS1	0.020	mg Si l^{-1}
18	BASAL OR RESTING RESPIRATION RATE	K1RB	0.030	d^{-1}
19	TEMPERATURE COEFFICIENT FOR BASAL/ENDOGENOUS RESPIRATION	K1RT	1.0	dimensionless
20	GROWTH-RATE-DEPENDENT RESPIRATION COEFFICIENT	K1RG	0.280	dimensionless
21	DEATH RATE DUE TO GRAZING	K1GRZC	0.100	d^{-1}
22	TEMPERATURE COEFFICIENT	K1GRZT	1.100	dimensionless
23	FRACTION OF C ALLOCATED TO STRUCTURAL PURPOSES	FSC1	0.10	dimensionless
24	CARBON TO CHLOROPHYLL RATIO	WCCHL1	40.0	mg C (mg chl)$^{-1}$
25	CARBON TO PHOSPHORUS RATIO - NON-P LIMITED	WCP1	40.0	mg C (mg P)$^{-1}$
26	CARBON TO NITROGEN RATIO - NON-N LIMITED	WCN1	5.0	mg C (mg N)$^{-1}$
27	CARBON TO SILICA RATIO - NON-SI LIMITED	WCS1	2.500	mg C (mg Si)$^{-1}$
28	QUOTIENT OF NUTRIENT-LIMITED NUTRIENT:C RATIOS AT RELATIVE GROWTH RATES OF 0 AND 1	QF1	0.85	
29	CHLOROPHYLL SELF-SHADING EXTINCTION COEFFICIENT FOR ALGAL GROUP 1	XKC1	0.017	m^2 (mg chl) $^{-1}$
30	BASE ALGAL SETTLING RATE - GROUP 1	VSBAS1	0.500	m d^{-1}
31	NUTRIENT STRESSED ALGAL SETTLING RATE - GROUP 1	VSNTR1	1.000	m d^{-1}
	Algal Group 2			

Order	Parameter definition	Symbol	Value	Unit
41	OPTIMAL GROWTH TEMPERATURE FOR SUMMER GROUP 2	TOPT2	18.000	^oC
42	TEMPERATURE CORRECTION EFFECT ON GROWTH RATE BELOW TOPT2	K2BETA1	0.004	$^oC^{-2}$
43	TEMPERATURE CORRECTION EFFECT ON GROWTH RATE ABOVE TOPT2	K2BETA2	0.006	$^oC^{-2}$
44	GROSS PHOTOSYNTHETIC RATE PER UNIT CELL (ASSOCIATED WITH PHOTOSYNTHETIC DARK REACTIONS)	GPRE2	3.0	d^{-1}
45	PHOTOSYNTHETIC RATE PER UNIT CELL PER UNIT LIGHT INTENSITY UNDER NUTRIENT-SATURATED CONDITIONS AND ZERO IRRADIANCE	GPR02	0.64 (0.28)	m^2 Ein^{-1}
46	SATURATING ALGAL LIGHT INTENSITY	IS2	000.0	Ein m^{-2} d^{-1}
47	HALF SATURATION CONSTANT FOR NITROGEN	KMN2	0.010	mg N l^{-1}
48	HALF SATURATION CONSTANT FOR PHOSPHOROUS	KMP2	0.001	mg P l^{-1}
49	HALF SATURATION CONSTANT FOR SILICA	KMS2	0.005	mg Si l^{-1}
50	BASAL OR RESTING RESPIRATION RATE	K2RB	0.036	d^{-1}
51	TEMPERATURE COEFFICIENT FOR BASAL/ENDOGENOUS RESPIRATION	K2RT	1.0	
52	GROWTH-RATE-DEPENDENT RESPIRATION COEFFICIENT	K2RG	0.280	
53	DEATH RATE DUE TO GRAZING	K2GRZC	0.100	d^{-1}
54	TEMPERATURE COEFFICIENT	K2GRZT	1.100	
55	FRACTION OF C ALLOCATED TO STRUCTURAL PURPOSES	FSC2	0.10	
56	CARBON TO CHLOROPHYLL RATIO	WCCHL2	65.0	mg C $(mg\ chl)^{-1}$
57	CARBON TO PHOSPHORUS RATIO - NON-P LIMITED	WCP2	40.000	mg C $(mg\ P)^{-1}$
58	CARBON TO NITROGEN RATIO - NON-N LIMITED	WCN2	5.670	mg C $(mg\ N)^{-1}$
59	CARBON TO SILICA RATIO - NON-SI LIMITED	WCS2	7.000	mg C $(mg\ Si)^{-1}$
60	QUOTIENT OF NUTRIENT-LIMITED NUTRIENT:C RATIOS AT RELATIVE GROWTH RATES OF 0 AND 1	QF2	0.85	
61	CHLOROPHYLL SELF-SHADING EXTINCTION COEFFICIENT FOR ALGAL GROUP 2	XKC2	0.017	m^2 $(mg\ chl)^{-1}$
62	BASE ALGAL SETTLING RATE - GROUP 2	VSBAS2	0.300	m d^{-1}
63	NUTRIENT STRESSED ALGAL SETTLING RATE - GROUP 2	VSNTR2	0.700	m d^{-1}
	Algal Group 3			
73	OPTIMAL GROWTH TEMPERATURE FOR DIATOMS	TOPT3	14.0	^oC
74	TEMPERATURE CORRECTION EFFECT ON GROWTH RATE BELOW TOPT3	K3BETA1	0.004	$^oC^{-2}$
75	TEMPERATURE CORRECTION EFFECT ON GROWTH RATE ABOVE TOPT3	K3BETA2	0.006	$^oC^{-2}$
76	GROSS PHOTOSYNTHETIC RATE PER UNIT CELL (ASSOCIATED WITH PHOTOSYNTHETIC DARK REACTIONS)	GPRE3	2.5	d^{-1}

Order	Parameter definition	Symbol	Value	Unit
77	GROSS PHOTOSYNTHETIC RATE PER UNIT CELL PER UNIT LIGHT INTENSITY UNDER NUTRIENT-SATURATED CONDITIONS AND ZERO IRRADIANCE	GPR03	0.64 (0.28)	m^2 Ein^{-1}
78	SATURATING ALGAL LIGHT INTENSITY	IS3	000.0	Ein m^{-2} d^{-1}
79	HALF SATURATION CONSTANT FOR NITROGEN	KMN3	0.005	mg N l^{-1}
80	HALF SATURATION CONSTANT FOR PHOSPHOROUS	KMP3	0.001	mg P l^{-1}
81	HALF SATURATION CONSTANT FOR SILICA	KMS3	0.040	mg Si l^{-1}
82	BASAL OR RESTING RESPIRATION RATE	K3RB	0.030	d^{-1}
83	TEMPERATURE COEFFICIENT FOR BASAL/ENDOGENOUS RESPIRATION	K3RT	1.0	dimensionless
84	GROWTH-RATE-DEPENDENT RESPIRATION COEFFICIENT	K3RG	0.280	dimensionless
85	DEATH RATE DUE TO GRAZING	K3GRZC	0.100	d^{-1}
86	TEMPERATURE COEFFICIENT	K3GRZT	1.100	dimensionless
87	FRACTION OF C ALLOCATED TO STRUCTURAL PURPOSES	FSC3	0.10	dimensionless
88	CARBON TO CHLOROPHYLL RATIO	WCCHL3	15.0	mg C (mg chl)$^{-1}$
89	CARBON TO PHOSPHORUS RATIO - NON-P LIMITED	WCP3	40.000	mg C (mg P)$^{-1}$
90	CARBON TO NITROGEN RATIO - NON-N LIMITED	WCN3	5.670	mg C (mg N)$^{-1}$
91	CARBON TO SILICA RATIO - NON-SI LIMITED	WCS3	2.500	mg C (mg Si)$^{-1}$
92	QUOTIENT OF NUTRIENT-LIMITED NUTRIENT:C RATIOS AT RELATIVE GROWTH RATES OF 0 AND 1	QF3	0.85	
93	CHLOROPHYLL SELF-SHADING EXTINCTION COEFFICIENT FOR ALGAL GROUP 3	XKC3	0.017	m^2 (mg chl) $^{-1}$
94	BASE ALGAL SETTLING RATE - GROUP 3	VSBAS3	0.300	m d^{-1}
95	NUTRIENT STRESSED ALGAL SETTLING RATE - GROUP 3	VSNTR3	1.000	m d^{-1}
	Biogeochemical parameters			
105	HALF SATURATION CONSTANT FOR PHYTOPLANKTON RECYCLE FRACTIONS MG C/L	KMPHYT	0.050	mg C l^{-1}
106	REFRACTORY PARTICULATE ORGANIC PHOSPHOROUS	FRPOP	0.150	
107	LABILE PARTICULATE ORGANIC PHOSPHOROUS	FLPOP	0.300	
108	REFRACTORY DISSOLVED ORGANIC PHOSPHOROUS	FRDOP	0.100	
109	LABILE DISSOLVED ORGANIC PHOSPHOROUS	FLDOP	0.150	
110	DISSOLVED INORGANIC PHOSPHOROUS	FPO4	0.300	
111	REFRACTORY PARTICULATE ORGANIC NITROGEN	FRPON	0.150	
112	LABILE PARTICULATE ORGANIC NITROGEN	FLPON	0.325	
113	REFRACTORY DISSOLVED ORGANIC NITROGEN	FRDON	0.150	
114	LABILE DISSOLVED ORGANIC NITROGEN	FLDON	0.175	
115	AMMONIA	FNH4	0.200	
116	REFRACTORY PARTICULATE ORGANIC CARBON	FRPOC	0.150	
117	LABILE PARTICULATE ORGANIC CARBON	FLPOC	0.350	
118	REFRACTORY DISSOLVED ORGANIC CARBON	FRDOC	0.100	

Order	Parameter definition	Symbol	Value	Unit
119	LABILE DISSOLVED ORGANIC CARBON PHOSPHORUS	FLDOC	0.400	
120	HYDROLYSIS RATE OF RPOP TO RDOP	K57C	0.010	d^{-1}
121	TEMPERATURE COEFFICIENT	K57T	1.080	
122	HYDROLYSIS RATE OF LPOP TO LDOP	K68C	0.050	d^{-1}
123	TEMPERATURE COEFFICIENT	K68T	1.080	
124	MINERALIZATION RATE OF RDOP TO PO4	K79C	0.010	d^{-1}
125	TEMPERATURE COEFFICIENT	K79T	1.080	
126	MINERALIZATION RATE OF LDOP TO PO4	K89C	0.100	d^{-1}
127	TEMPERATURE COEFFICIENT NITROGEN	K89T	1.080	
128	HYDROLYSIS RATE OF RPON TO RDON	K1012C	0.008	d^{-1}
129	TEMPERATURE COEFFICIENT	K1012T	1.080	
130	HYDROLYSIS RATE OF LPON TO LDON	K1113C	0.050	d^{-1}
131	TEMPERATURE COEFFICIENT	K1113T	1.080	
132	MINERALIZATION RATE of RDON TO NH4	K1214C	0.008	d^{-1}
133	TEMPERATURE COEFFICIENT	K1214T	1.080	
134	MINERALIZATION RATE OF LDON TO NH4	K1314C	0.050	d^{-1}
135	TEMPERATURE COEFFICIENT NITRIFICATION/DENITRIFICATION RATES	K1314T	1.080	
136	NITRIFICATION RATE AT 20 DEG C	K1415C	0.100	d^{-1}
137	TEMPERATURE COEFFICIENT	K1415T	1.080	
138	HALF SATURATION CONSTANT FOR NITRIF- ICATION OXYGEN LIMITATION	KNIT	1.000	mg O_2 l^{-1}
139	DENITRIFICATION RATE AT 20 DEG C	K150C	0.050	d^{-1}
140	TEMPERATURE COEFFICIENT	K150T	1.045	
141	MICHAELIS CONSTANT FOR DENITRIFICATION OXYGEN LIMITATION SILICA MINERALIZATION RATES AT 20 DEG C	KNO3	0.100	mg O_2 l^{-1}
142	MINERALIZATION RATE OF BIOGENIC SI TO AVAIL SI	K1617C	0.080	d^{-1}
143	TEMPERATURE COEFFICIENT CARBON HYDROLYSIS/OXIDATION RATES AT 20 DEG C	K1617T	1.080	
144	HYDROLYSIS RATE OF RPOC TO RDOC	K1820C	0.010	d^{-1}
145	TEMPERATURE COEFFICIENT	K1820T	1.080	
146	HYDROLYSIS RATE OF LPOC TO LDOC	K1921C	0.070	d^{-1}
147	TEMPERATURE COEFFICIENT	K1921T	1.080	
148	OXIDATION RATE OF RDOC	K200C	0.008	d^{-1}
149	TEMPERATURE COEFFICIENT	K200T	1.080	
150	OXIDATION RATE OF LDOC	K210C	0.100	d^{-1}
151	TEMPERATURE COEFFICIENT	K210T	1.080	
152	MICHAELIS CONSTANT FOR LDOC	KMLDOC	0.100	mg C l^{-1}
153	HALF SATURATION CONSTANT FOR ORG CARBON	KDOC	0.200	mg O_2 l^{-1}
154	ALGAL EXUDATE DOC OXIDATION RATE	K220C	0.300	d^{-1}
155	TEMPERATURE COEFFICIENT	K220T	1.047	
156	FRACTION OF PRIMARY PRODUCTIVITY GOING TO LABILE ORGANIC CARBON VIA EXUDATION REPOC/REDOC ARE ASSOCIATED WITH SANITARY/CSO SOLIDS	FLOCEX	0.100	
157	HYDROLYSIS RATE OF REPOC TO REDOC	K2324C	0.01	d^{-1}
158	TEMPERATURE COEFFICIENT	K2324T	1.0	
159	REACTIVE DOC OXIDATION RATE	K240C	0.150	d^{-1}
160	TEMPERATURE COEFFICIENT	K240T	1.047	

Order	Parameter definition	Symbol	Value	Unit
161	CARBON TO PHOSPHORUS RATIO OF CSO SOLIDS	CTOPCSO	0.0	
162	CARBON TO NITROGEN RATIO OF CSO SOLIDS	CTONCSO	0.0	
163	OXIDATION RATE FOR AQUEOUS SOD	K250C	0.150	d^{-1}
164	TEMPERATURE COEFFICIENT	K250T	1.080	
165	HALF SATURATION CONSTANT FOR O2*	KO2EQ	0.100	mg O_2 l^{-1}
166	MINIMUM VALUE FOR KL	KLMIN	0.0	m d^{-1}
167	DIFFUSIVITY OF OXYGEN ACROSS THE AIR-WATER INTERFACE	DIFUS	0.0	m^2 d^{-1}
168	TEMPERATURE CORRECTION COEFFICIENT FOR ATMOSPHERIC REAERATION	KAT	1.024	
169	TEMPERATURE CORRECTION	VSBAST	1.027	
170	PARTICULATE ORGANIC MATTER SETTLING RATE	VSPOM	1.000	m d^{-1}
171	TEMPERATURE CORRECTION	VSPMT	1.027	
172	TEMPERATURE CORRECTION FOR DEPOSITION TO SEDIMENT	VSSEDT	1.027	
173	POWER COEFF. FOR CSO SOLID SETTLING RATE (>=1	BVCSO	1.0	dimensionless
174	CRITICAL REPOC CONC. FOR CSO SETTLING FUNCTION	CRCSO	1.0	mg C l^{-1}
175	MINIMUM SETTLING RATE FOR CSO SOLIDS Vcso = VMINCSO+(VMAXCSO-VMINCSO)*(REPOC/CRCSO)**BVCSO)	VMINCSO	0.0	m d^{-1}
176	MAXIMUM SETTLING RATE FOR CSO SOLIDS	VMAXCSO	0.0	m d^{-1}
177	PARTITION COEFFICIENT FOR SORBED PHOSPHORUS	KADPO4	6.0	l mg SS^{-1}
178	PARTITION COEFFICIENT FOR SORBED SILICA	KADSI	6.0	l mg SS^{-1}
179	SETTLING RATE FOR PHOSPHORUS/SILICA SORBED TO SUSPENDED SOLIDS	VSPIM	0.0	m d^{-1}
180	BASE (CHL-A CORRECTED) EXTINCTION COEFFICIENT (USED WHEN KEOPT=0,2)	KECONST	0.001	m^{-1}

Table 2. 3 Data-model conversion for the MWRA effluent, rivers, and other sources.

	Model		**Conversion**	**Data**	
Variable	Definition	Units	Function	Variable	Units
Flow	Sewage flow	L day^{-1}	3.785mflow	mflow	gallon d^{-1}
TOC	Total organic C	mg C d^{-1}	0.7CBOD+18	CBOD	mg O d^{-1}
RPOC	Refractory POC	mg C d^{-1}	9	CBOD	mg O d^{-1}
LPOC	Labile POC	mg C d^{-1}	0.198CBOD	CBOD	mg O d^{-1}
RDOC	Refractory DOC	mg C d^{-1}	9	CBOD	mg O d^{-1}
LDOC	Labile DOC	mg C d^{-1}	0.132CBOD	CBOD	mg O d^{-1}
REDOC	Reactive DOC	mg C d^{-1}	0.37CBOD	CBOD	mg O d^{-1}
TON	Total organic N	mg N d^{-1}	(TKN-NH4)/1000	TKN	μg N d^{-1}
RPON	Refractory PON	mg N d^{-1}	0.4(TKN-NH4)/1000	TKN	μg N d^{-1}
LPON	Labile PON	mg N d^{-1}	0.4(TKN-NH4)/1000	TKN	μg N d^{-1}
RDON	Refractory DON	mg N d^{-1}	0.1(TKN-NH4)/1000	TKN	μg N d^{-1}
LDON	Labile DON	mg N d^{-1}	0.1(TKN-NH4)/1000	TKN	μg N d^{-1}
TOP	Total organic P	mg P d^{-1}	(TP-PO4)/1000	TP	μg P d^{-1}
RPOP	Refractory POP	mg P d^{-1}	0.3(TP-PO4)/1000	TP	μg P d^{-1}
LPOP	Labile POP	mg P d^{-1}	0.55(TP-PO4)/1000	TP	μg P d^{-1}
RDOP	Refractory DOP	mg P d^{-1}	0.05(TP-PO4)/1000	TP	μg P d^{-1}
LDOP	Labile DOP	mg P d^{-1}	0.1(TP-PO4)/1000	TP	μg P d^{-1}

Table 2. 4 Partition coefficients for organic substances in seawater and river water.

		Labile	Refractory	Reactive	Exudate
Nitrogen	PON	0.5	0.5		
	DON	0.5	0.5		
Phosphorus	POP	0.647	0.353		
	DOP	0.66	0.33		
Carbon	POC	0.4	0.6	-	-
	DOC	0.2	0.7	0.05	0.05

Table 2. 5 Partition coefficients of chlorophyll to phytoplankton groups at the open boundary.

	Winter-spring group	Summer group	Fall group
January-April	1.0	0	0
May	0.5	0.5	0
June-July	0	1.0	0
August	0	0.5	0.5
September-November	0	0	1.0
December	0.5	0	0.5

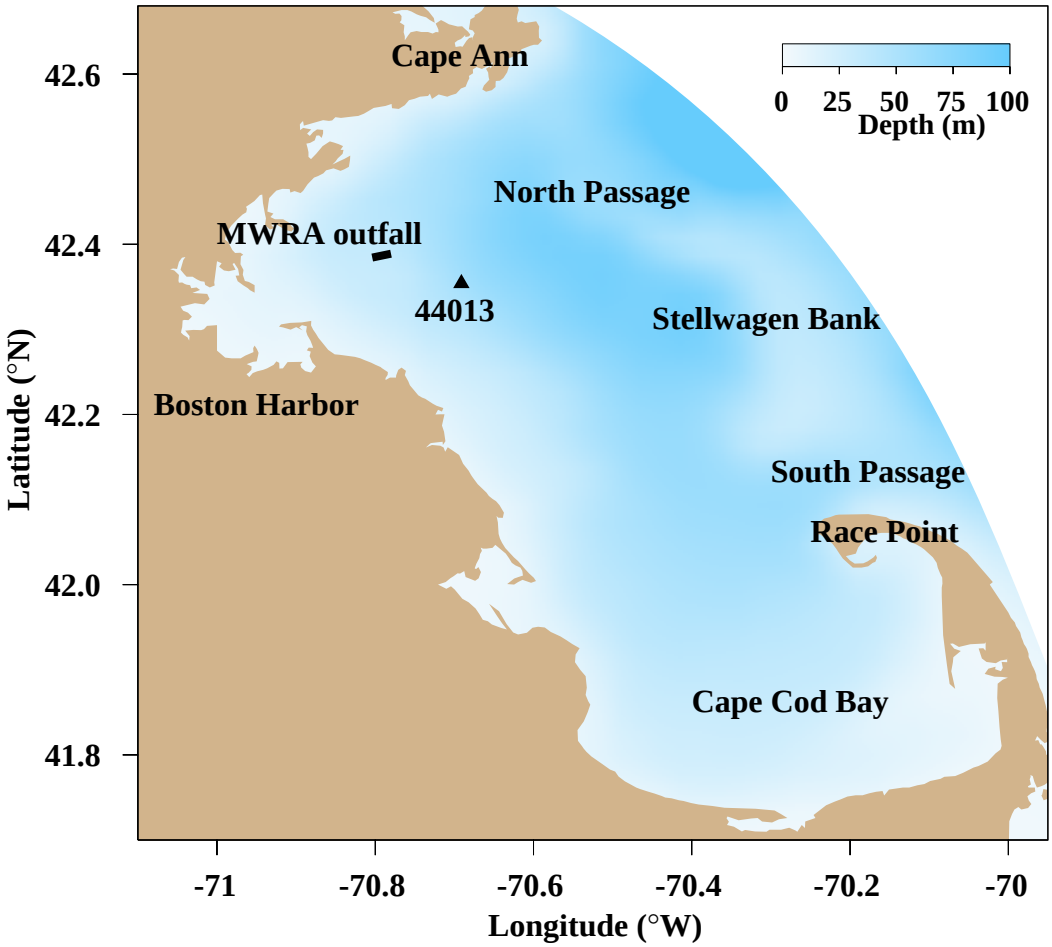

Figure 1. 1 The Massachusetts Bay system (MBS) and location of the MWRA outfall and Buoy 44013.

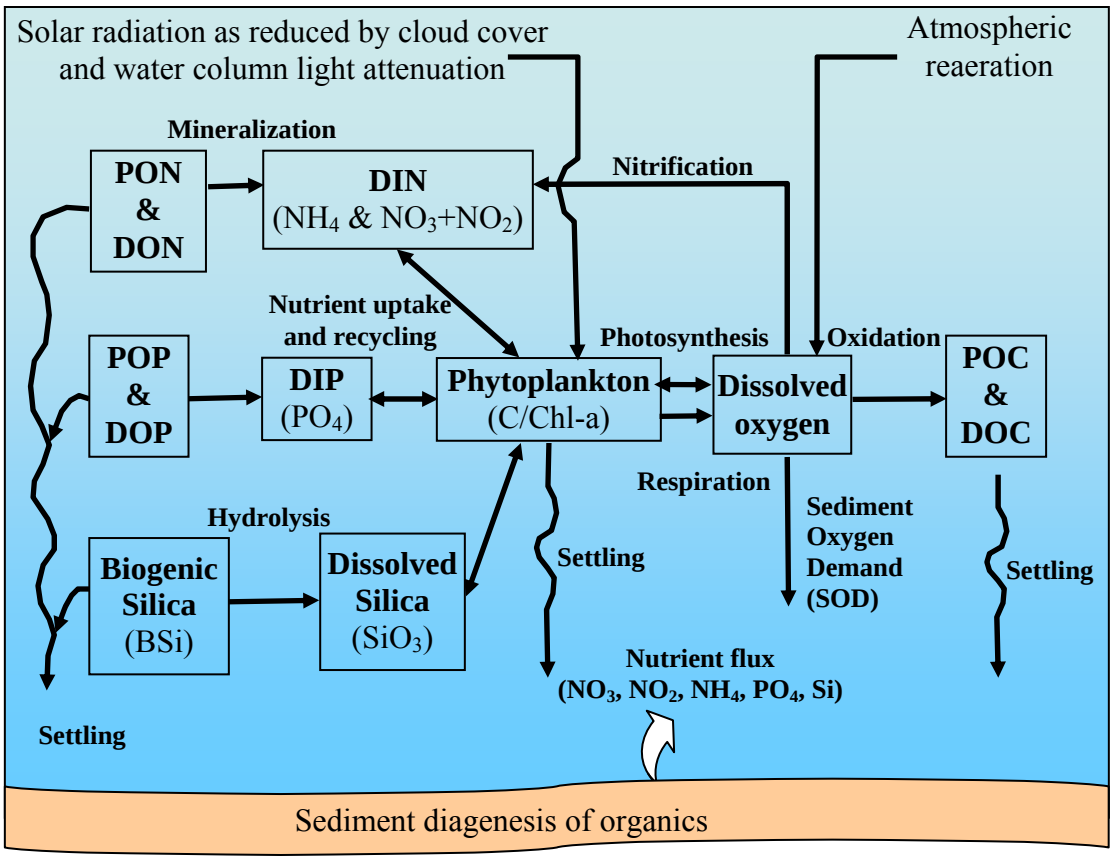

Figure 2. 1 The UG-RCA water quality model (reproduced from HydroQual, 2004).

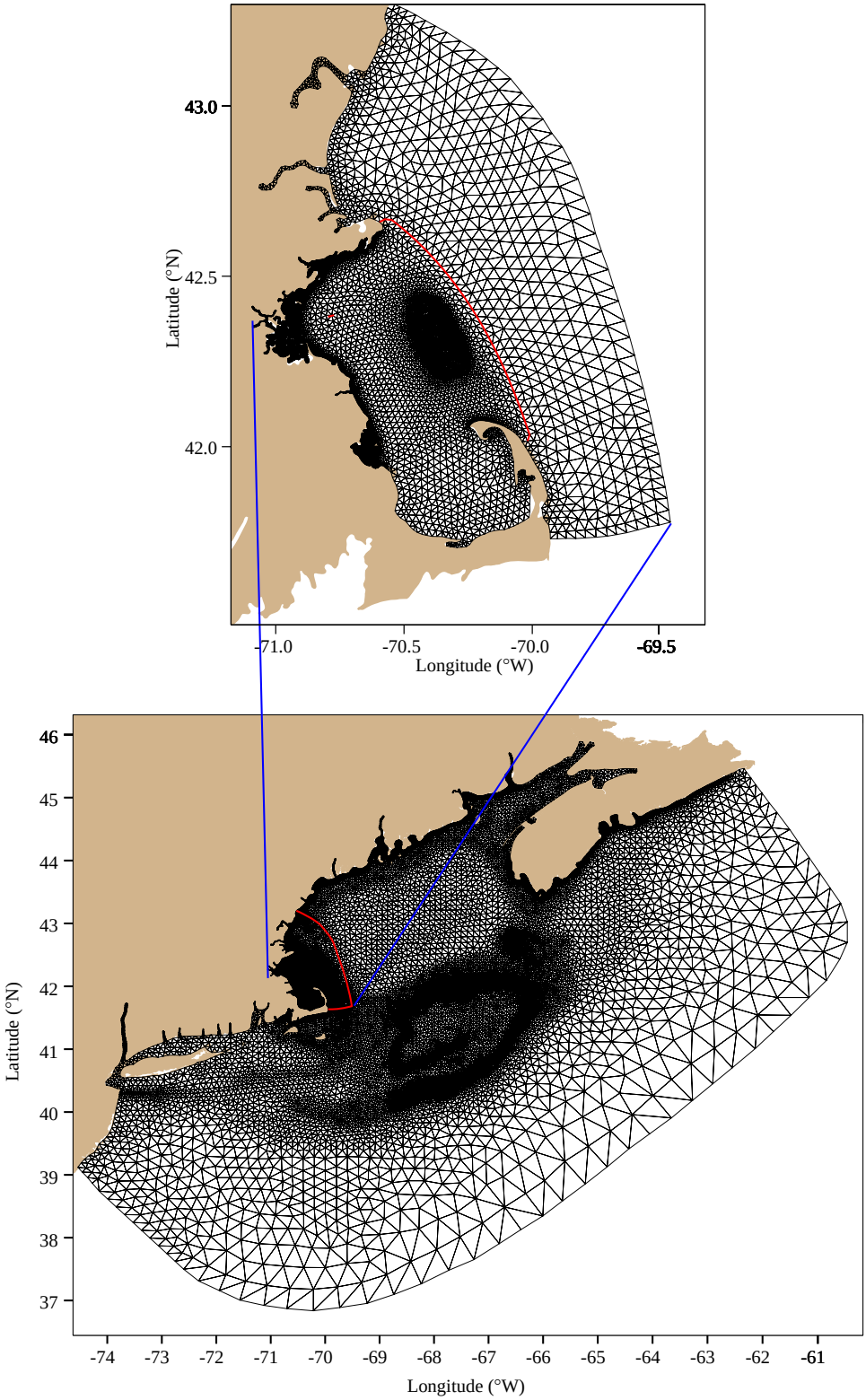

Figure 2. 2 Grid for Gulf-of-Maine FVCOM (lower panel); the red line shows the nested domain of Massachusetts Bay FVCOM. The upper panel shows the higher-resolution grid for MB-FVCOM; the red line shows the domain of the water quality model UG-RCA.

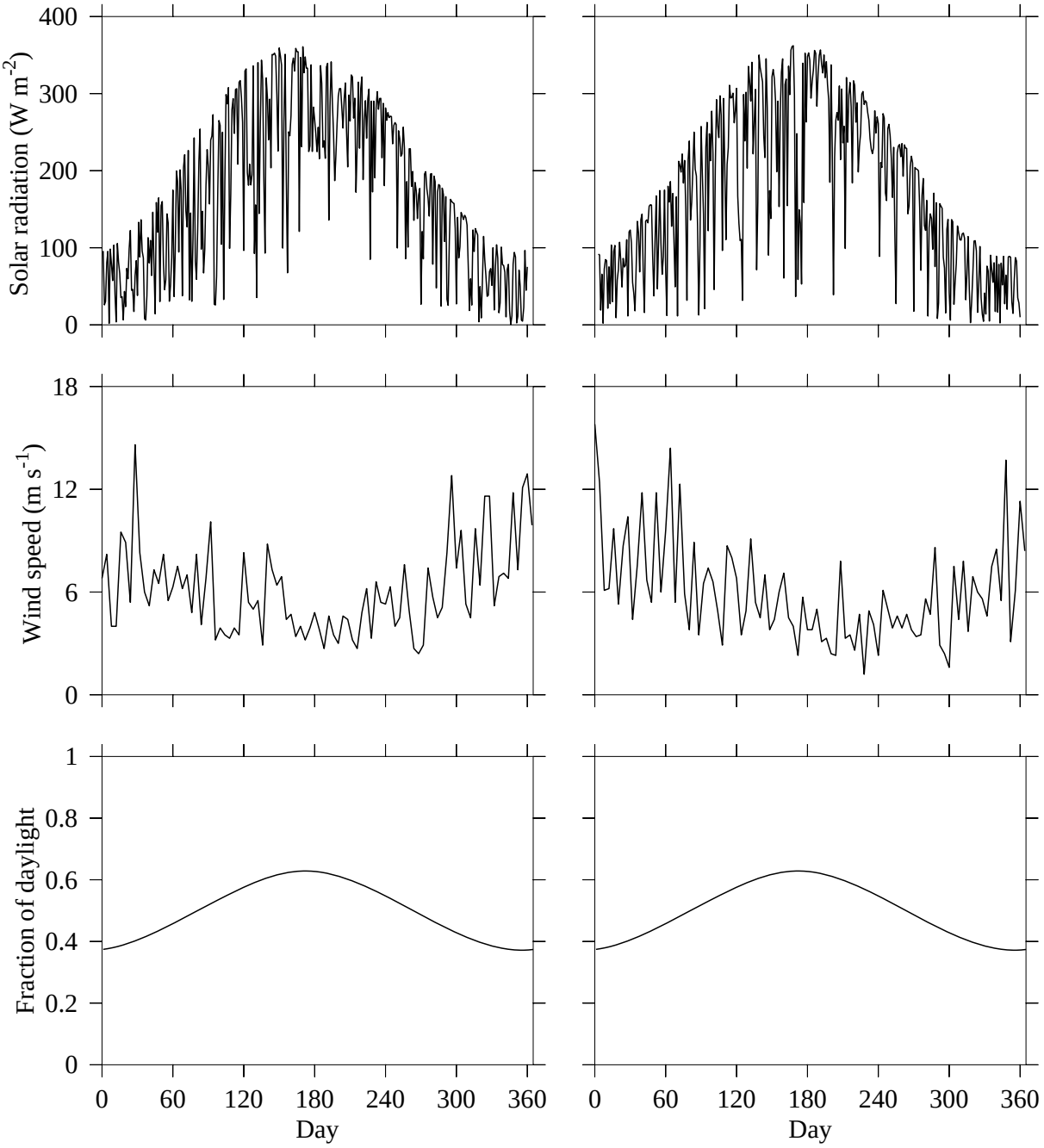

Figure 2. 3 Daily averaged total solar radiation, wind speed, and fraction of daylight in 2008 (left panel for comparison) and 2009 (right panel).

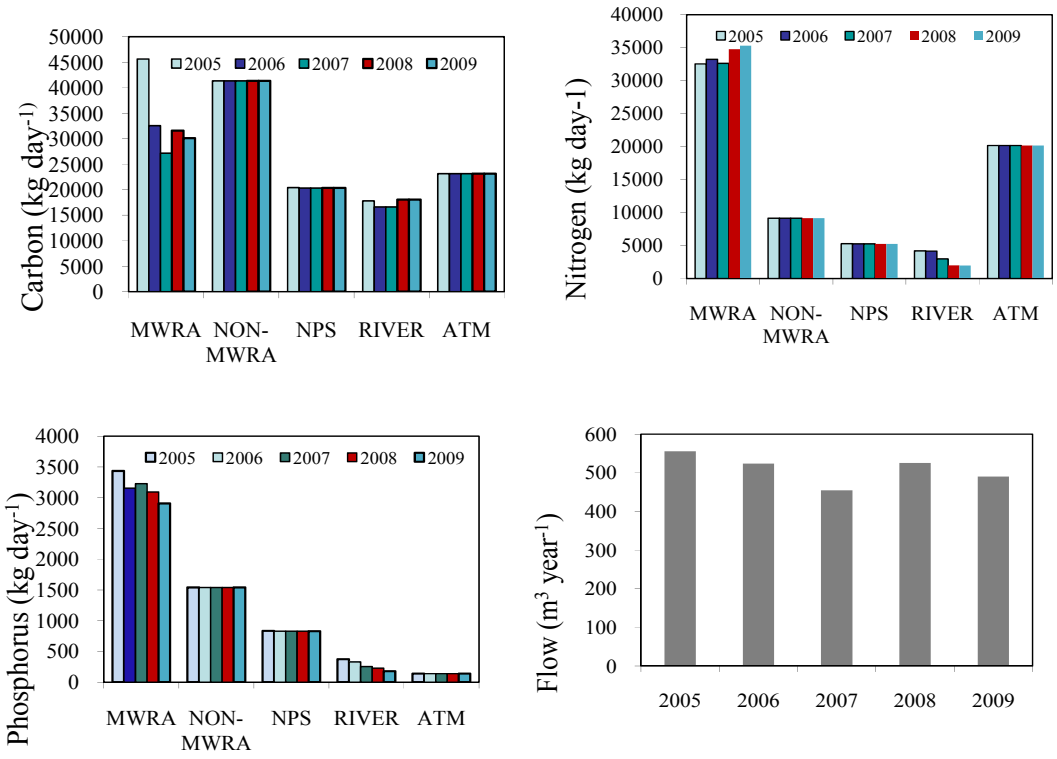

Figure 2. 4 Mean daily loads of carbon, nitrogen and phosphorus from different anthropogenic sources. MWRA: MWRA outfall; Non-MWRA: Non MWRA point sources; NPS: Non-point sources; River: River loadings; ATM: Atmospheric input. The last panel depicts the total flow of the MWRA outfall.

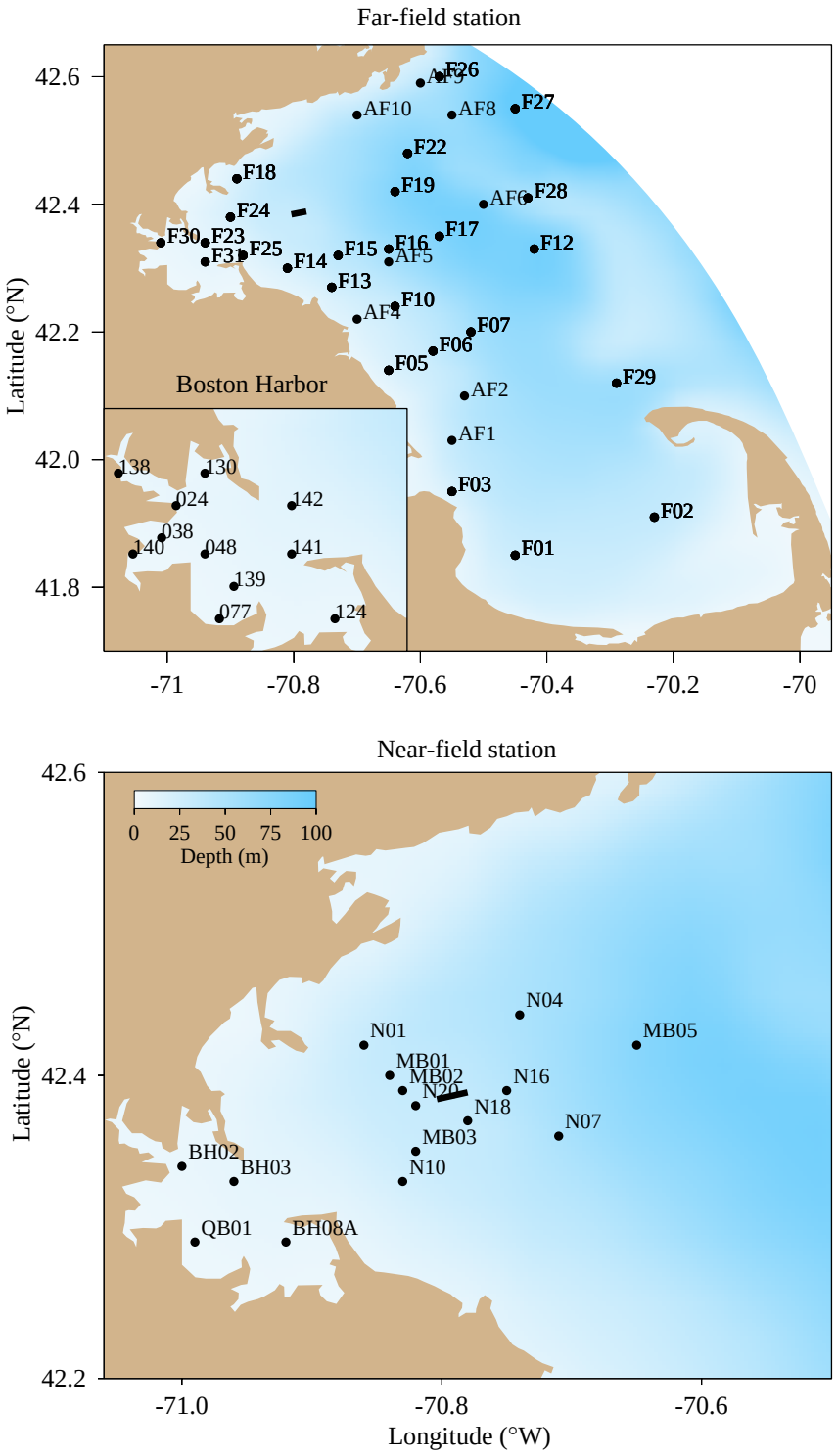

Figure 2. 5 Station locations: far-field (denoted with "F"), *Alexandrium* Rapid Response Study (denoted with "AF") and harbor stations in the upper panel, and near-field (denoted with "N"), harbor sediment flux (denoted with "BH" and "QB") and Massachusetts Bay sediment flux (denoted with "MB") stations in the lower panel. The bold line represents the location of the MWRA outfall.

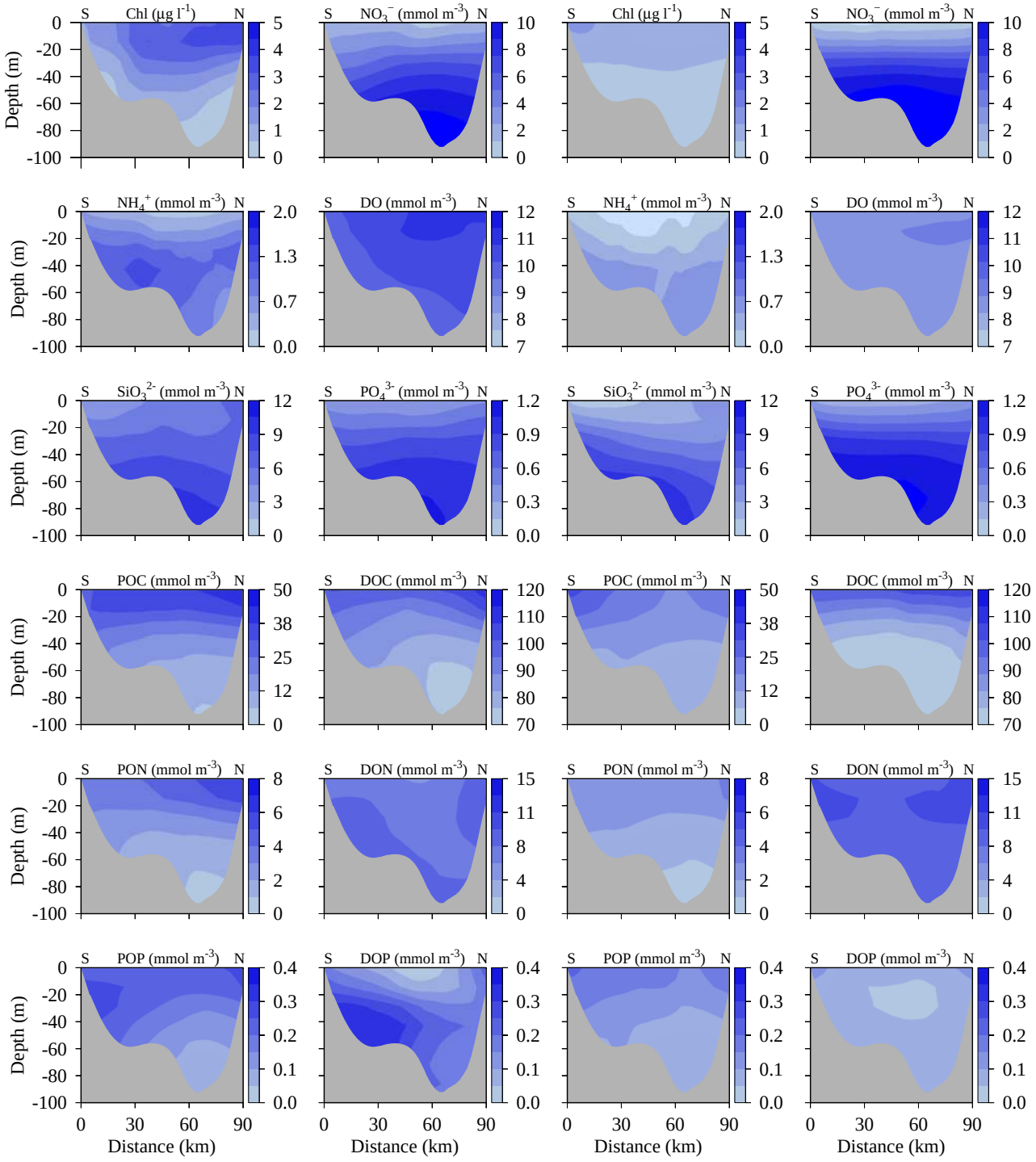

Figure 2. 6 Open boundary condition transects from Cape Cod (south S) to Cape Ann (north N) of chlorophyll, nutrients, DO and organic components on April 15 (left 12 panels) and August 15 (right 12 panels), 2009.

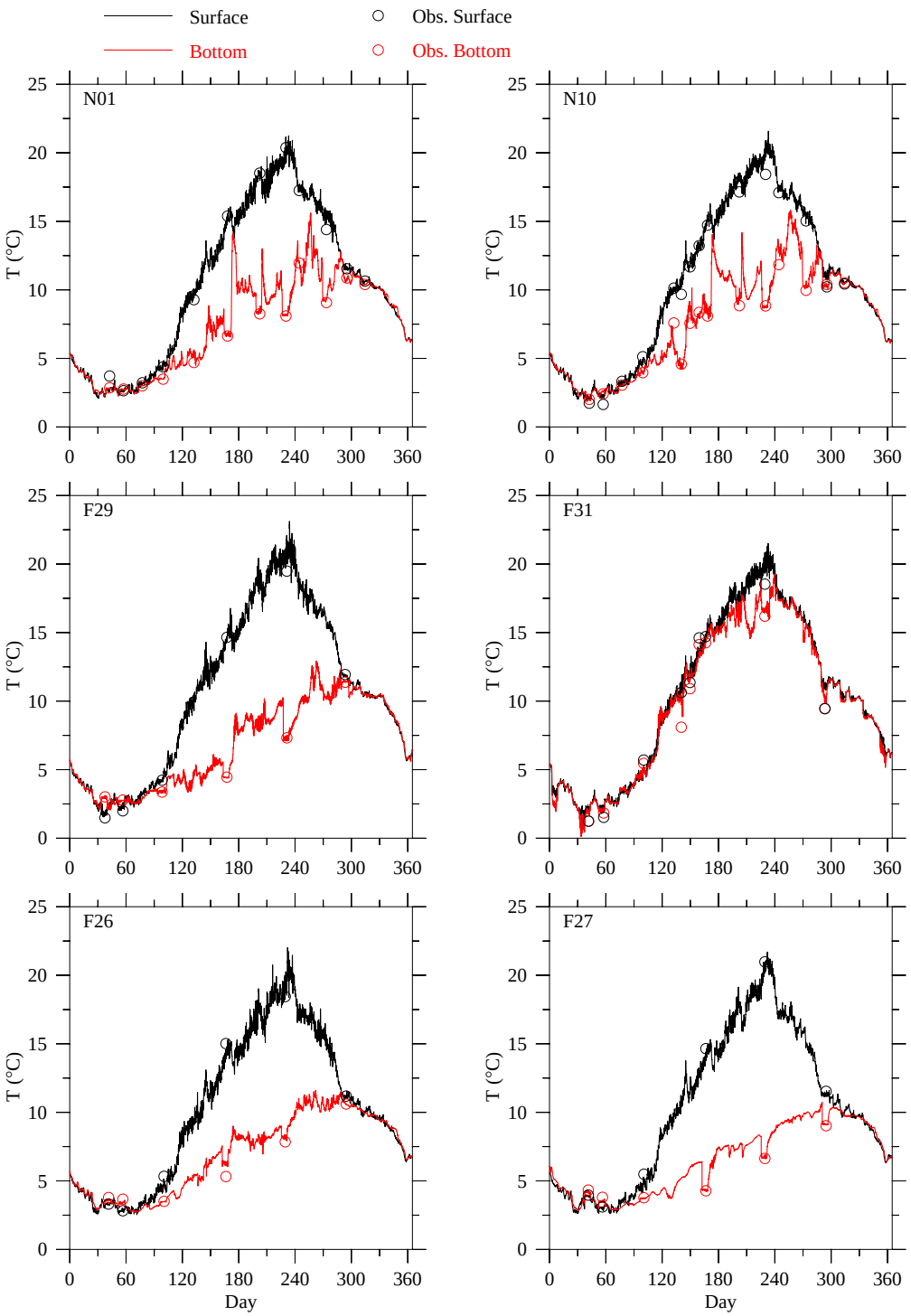

Figure 3. 1 Comparison of temperature observed (circles) and modeled (lines) time series at selected Massachusetts Bay monitoring stations in 2009.

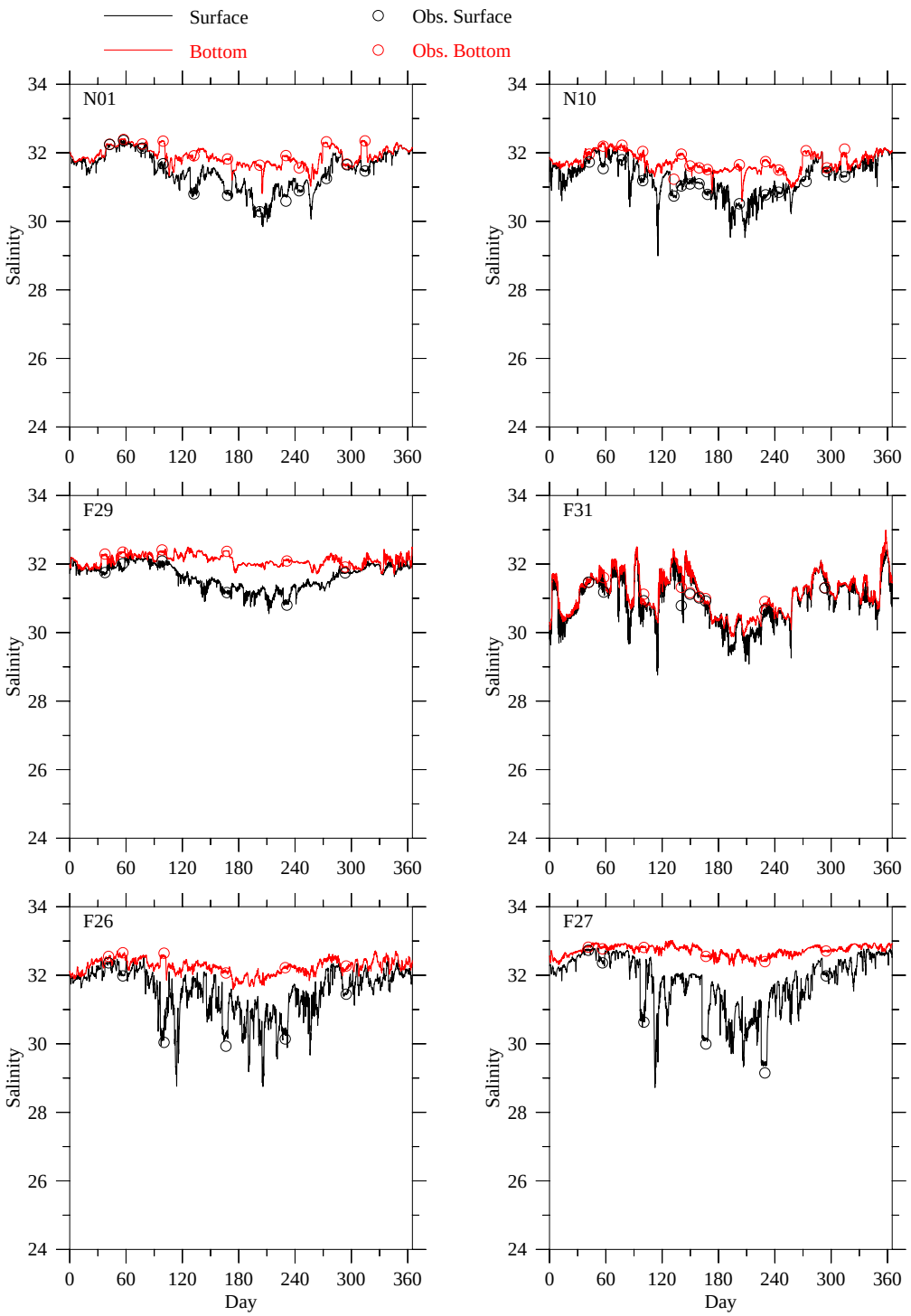

Figure 3. 2 Comparison of salinity observed (circles) and modeled (lines) time series at selected Massachusetts Bay monitoring stations in 2009.

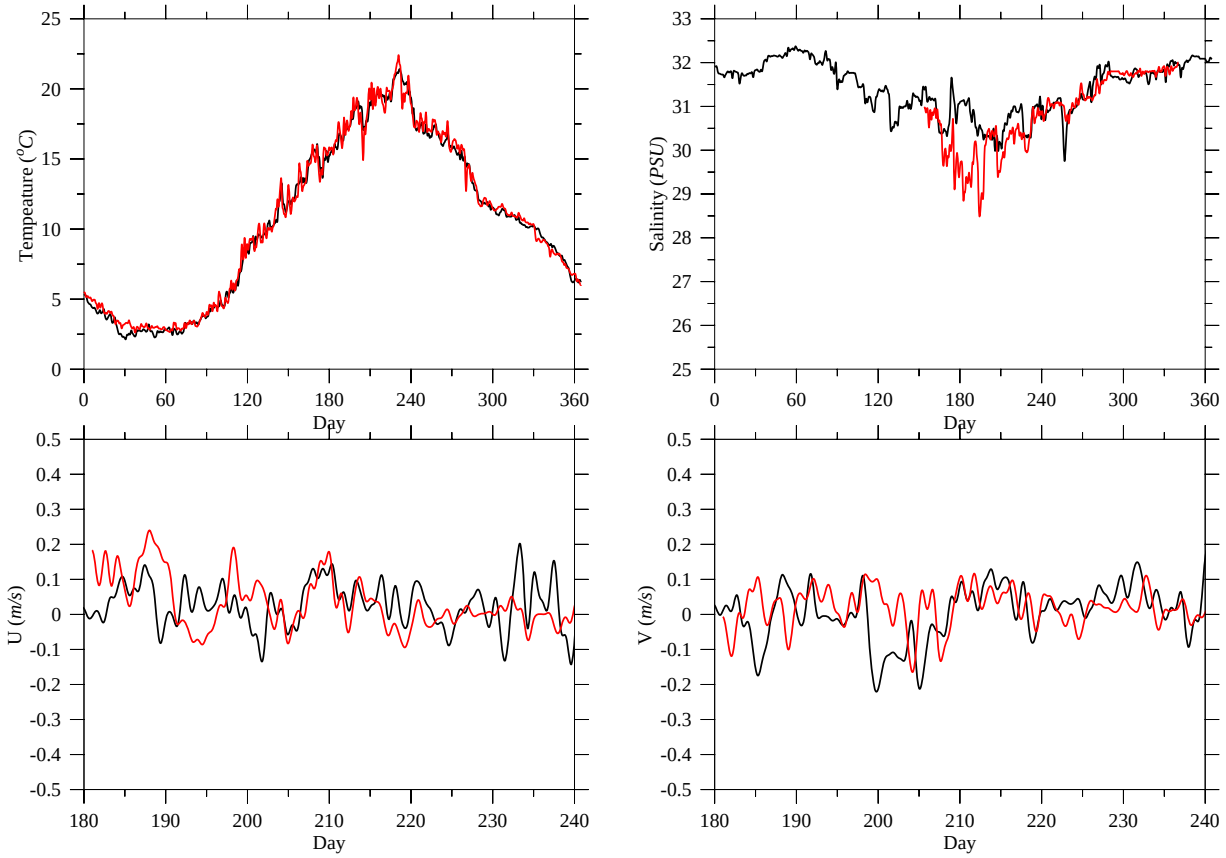

Figure 3. 3 Comparison of observed (red lines) and modeled (black lines) surface temperature, salinity and subtidal current U (west-east direction) and V (south-north direction) time series at Buoy 44013 in 2009. Salinity data is available only from June 1. The buoy location is shown on Figure 1.1.

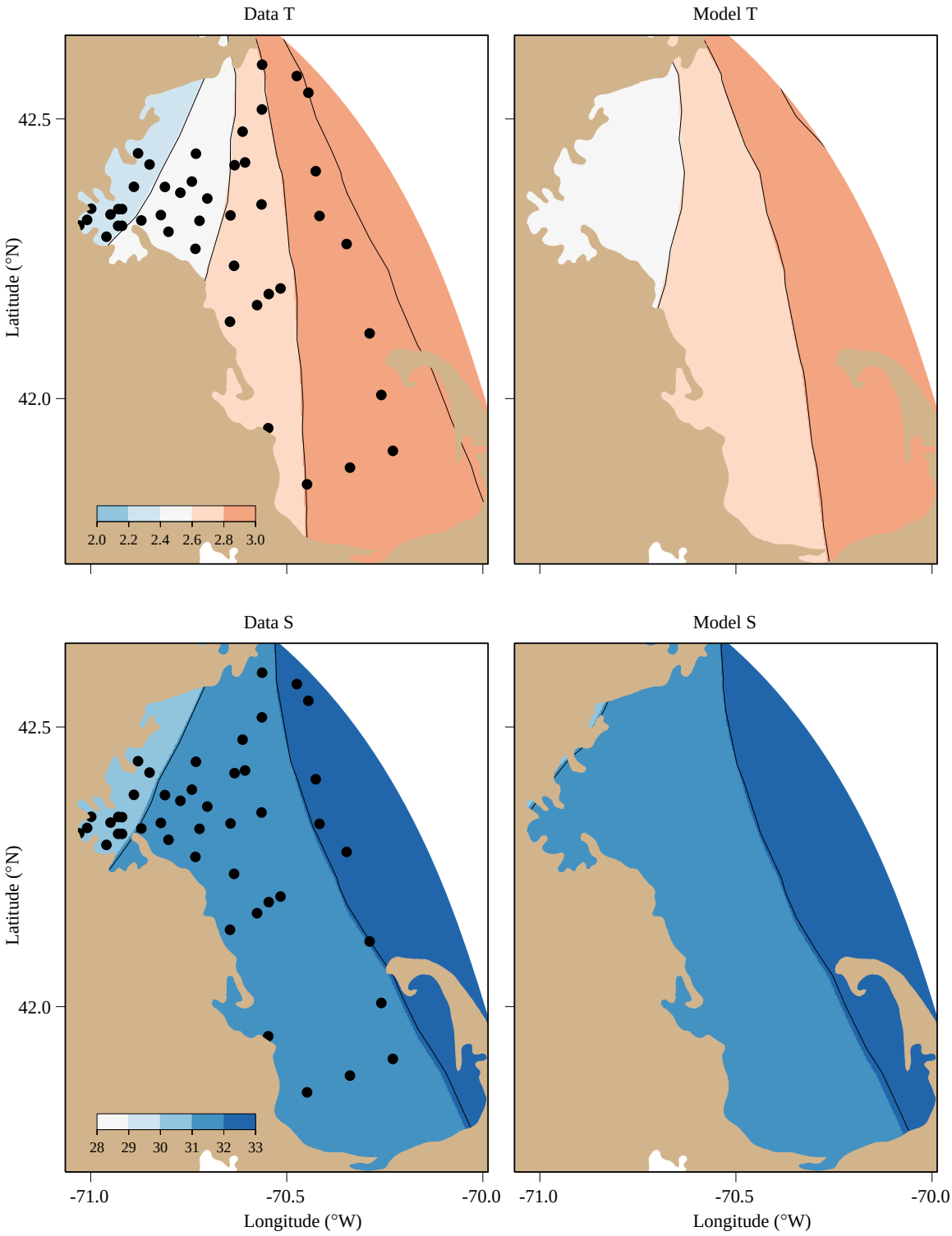

Figure 3. 4 Comparison between observed (left) and model-computed (right) near-surface temperatures (upper panels) and salinities (lower panels): February 2009.

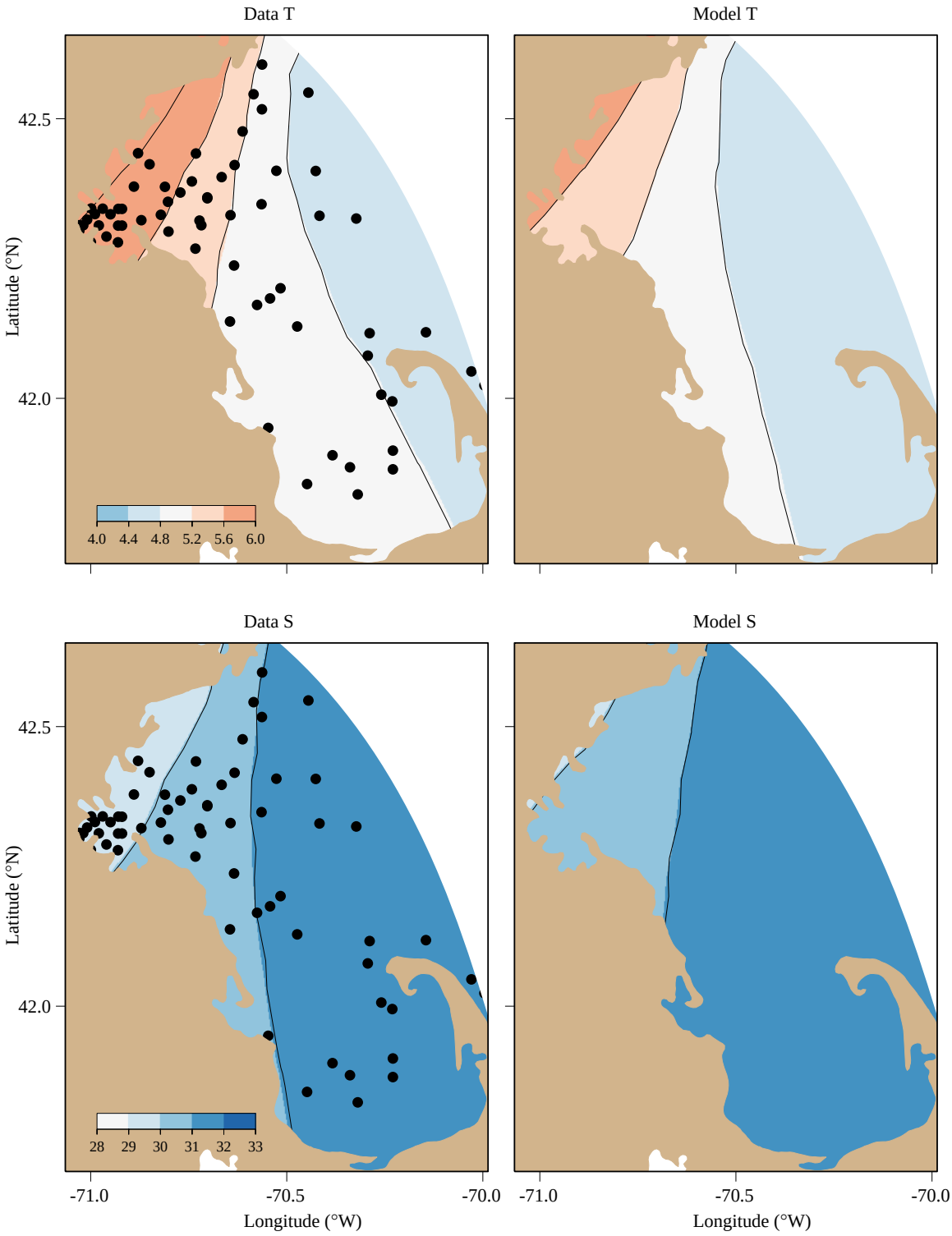

Figure 3. 5 Comparison between observed (left) and model-computed (right) near-surface temperatures (upper panels) and salinities (lower panels): April 2009**.**

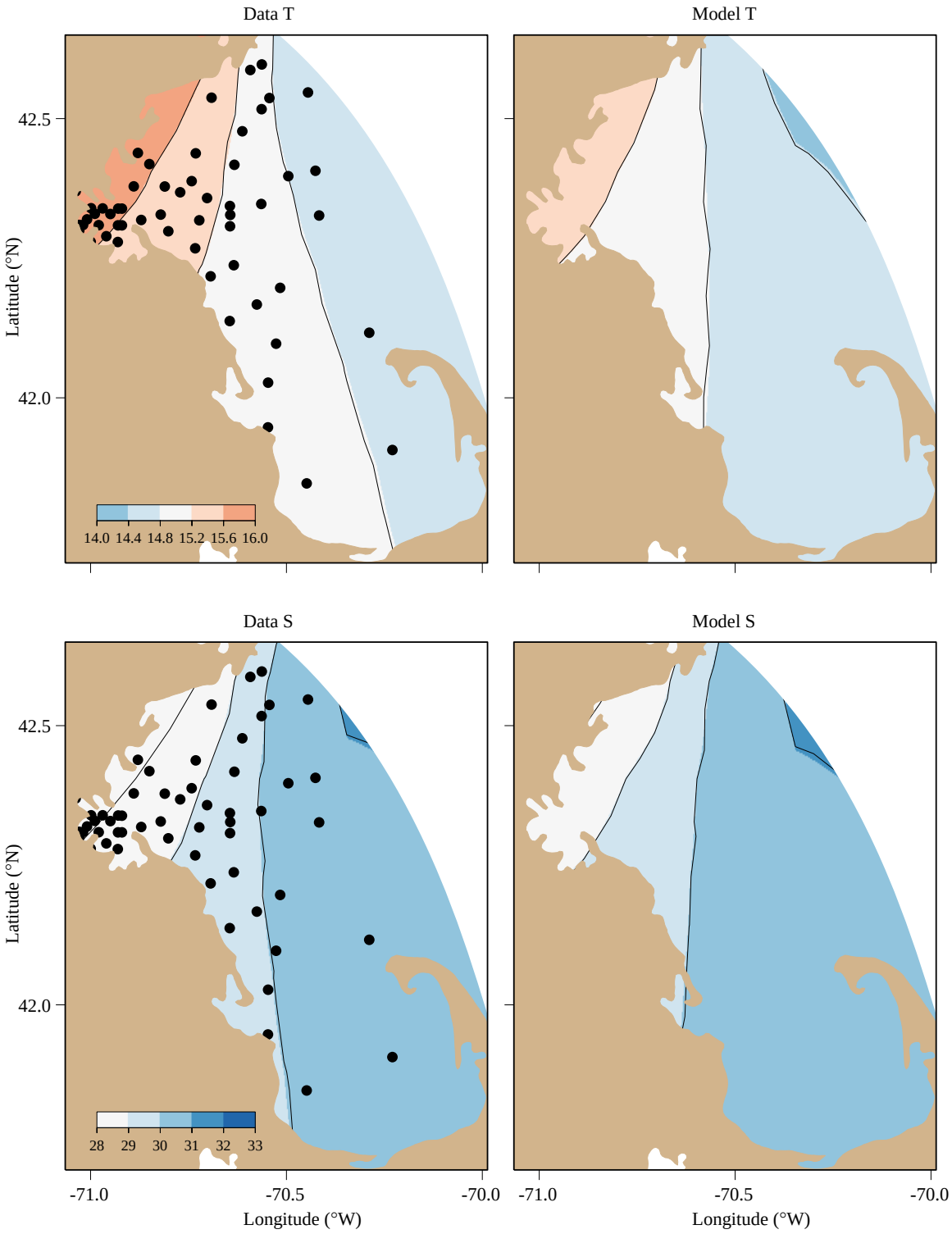

Figure 3. 6 Comparison between observed (left) and model-computed (right) near-surface temperatures (upper panels) and salinities (lower panels): June 2009.

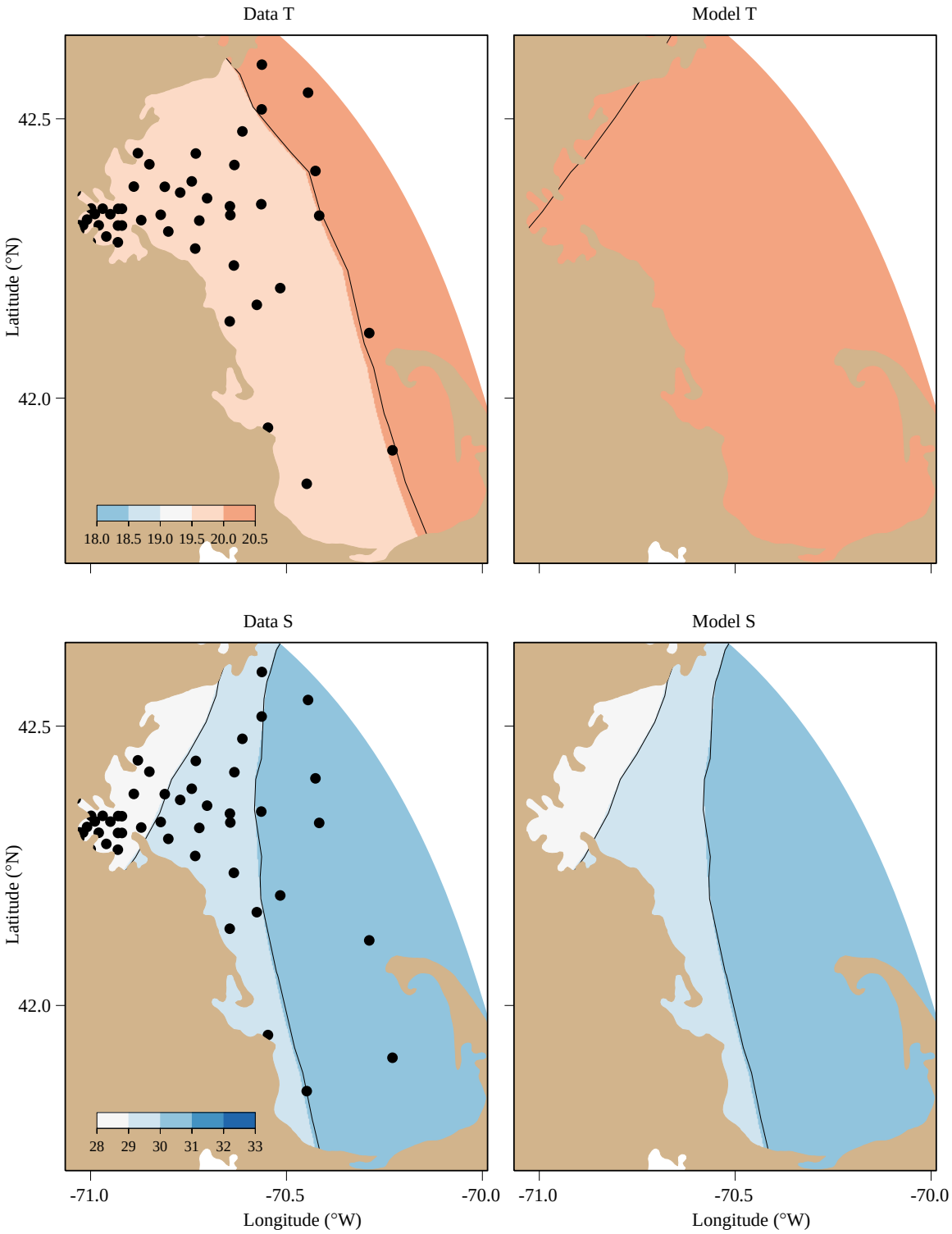

Figure 3. 7 Comparison between observed (left) and model-computed (right) near-surface temperatures (upper panels) and salinities (lower panels): August 2009.

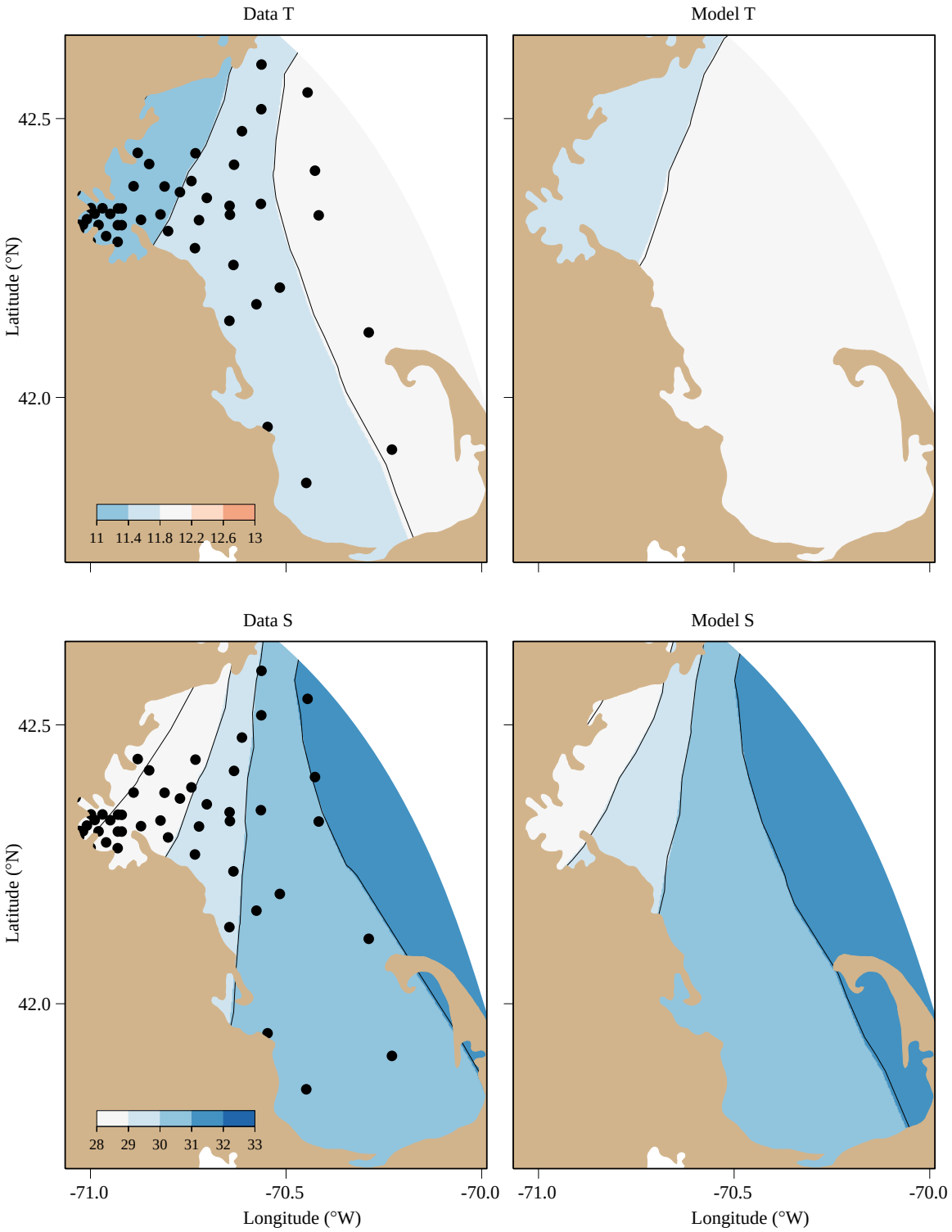

Figure 3. 8 Comparison between observed (left) and model-computed (right) near-surface temperatures (upper panels) and salinities (lower panels): October 2009.

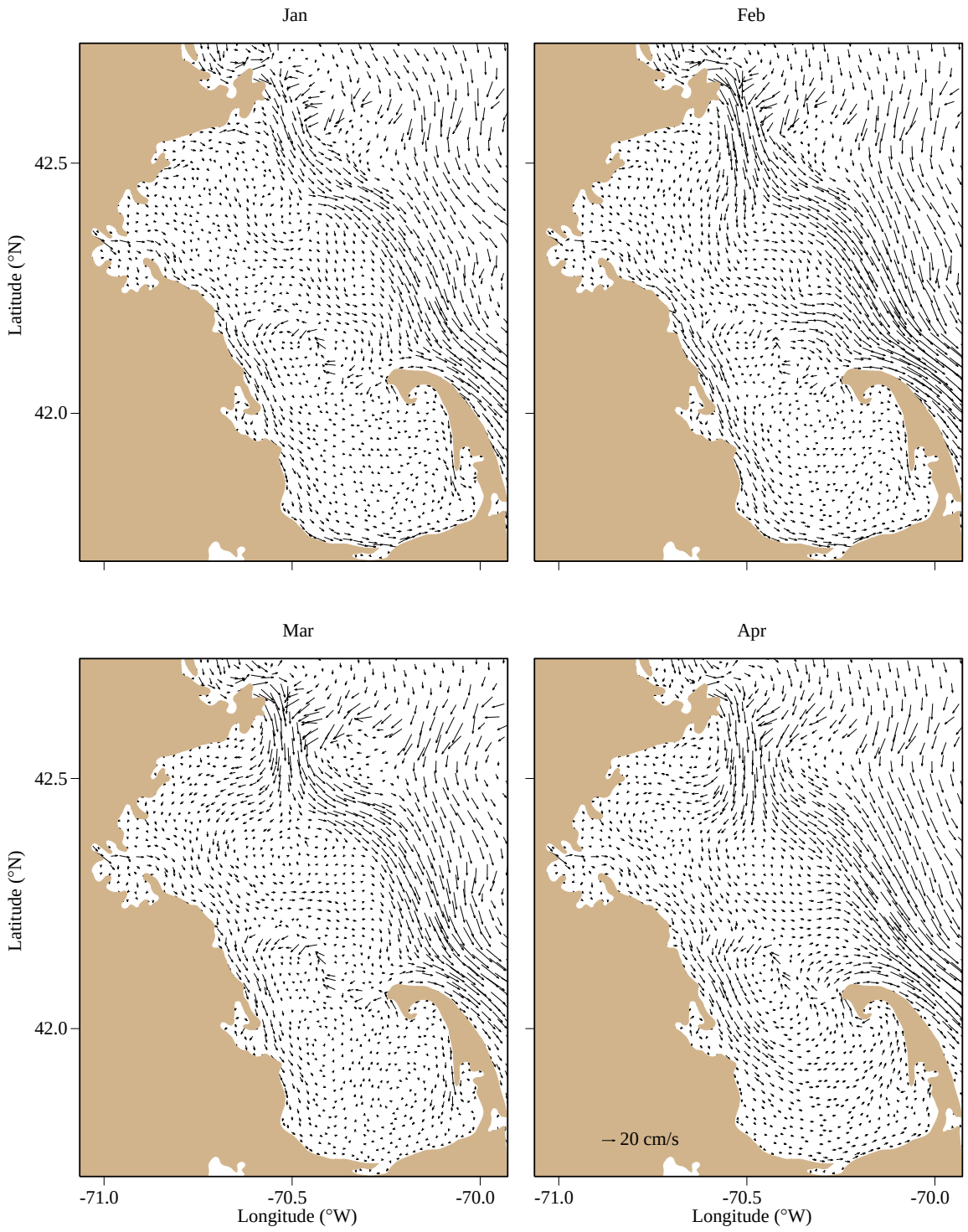

Figure 3. 9 Monthly-averaged surface current from January through April 2009 predicted by FVCOM.

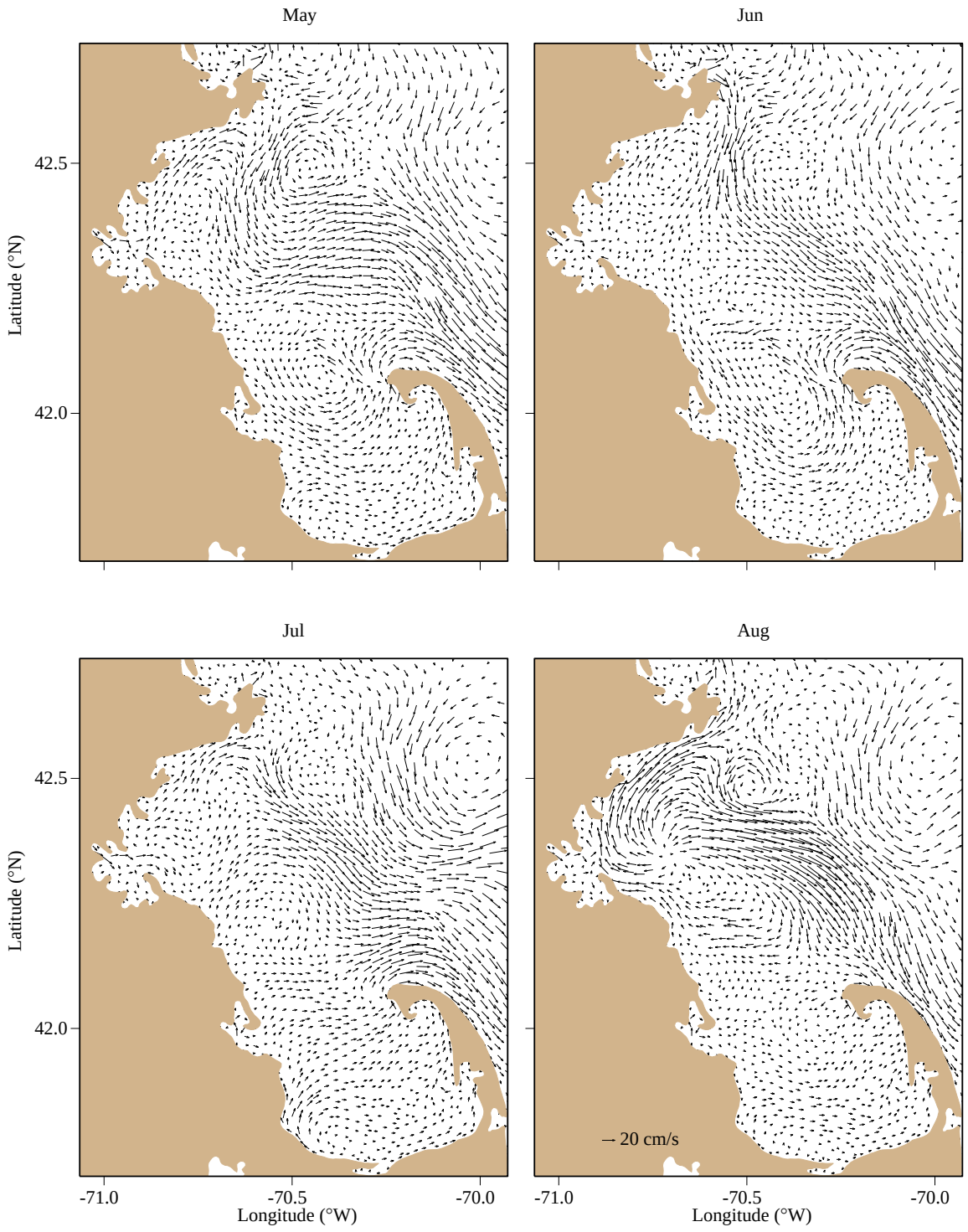

Figure 3. 10 Monthly-averaged surface current from May through August 2009 predicted by FVCOM.

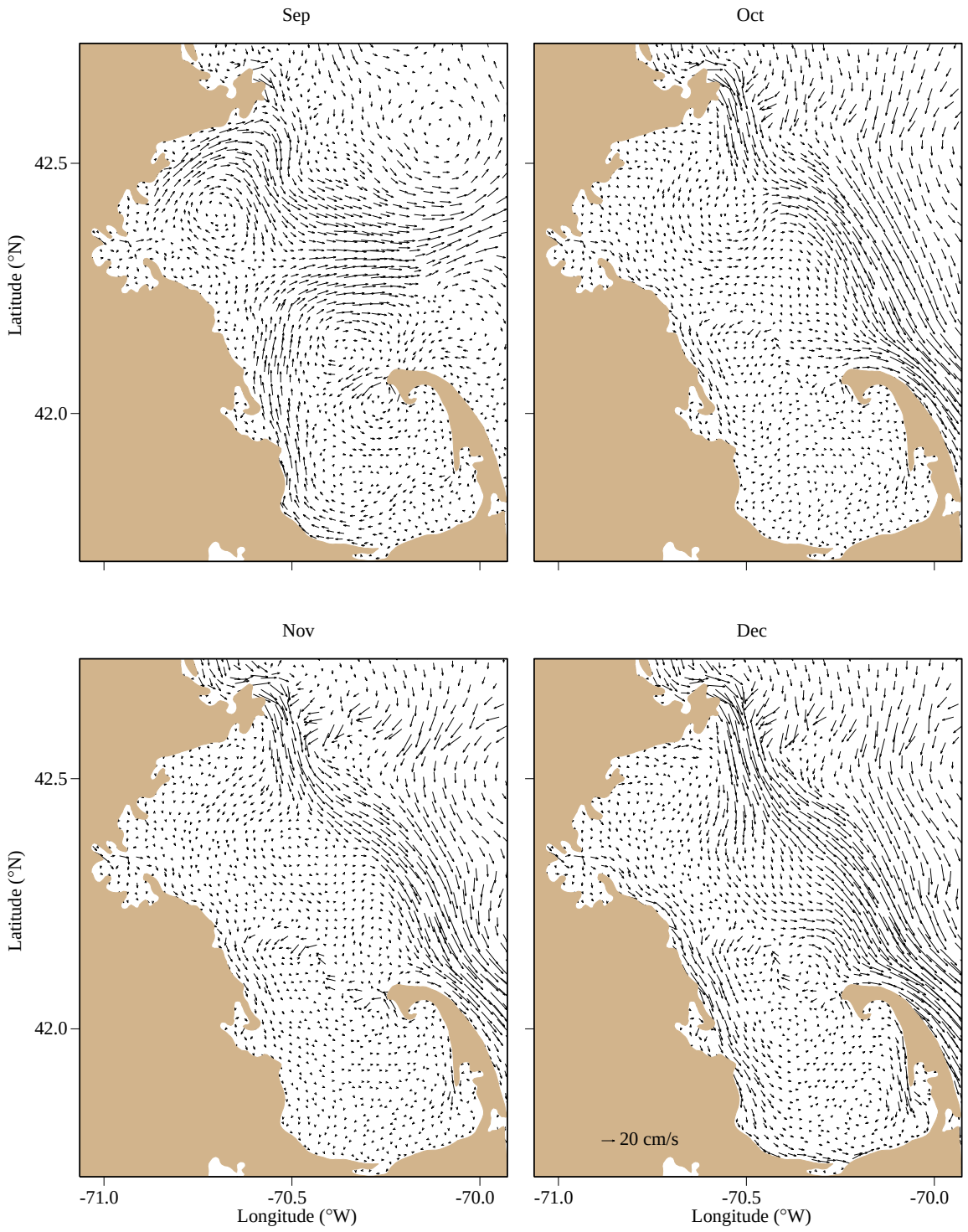

Figure 3. 11 Monthly-averaged surface current from September through December 2009 predicted by FVCOM.

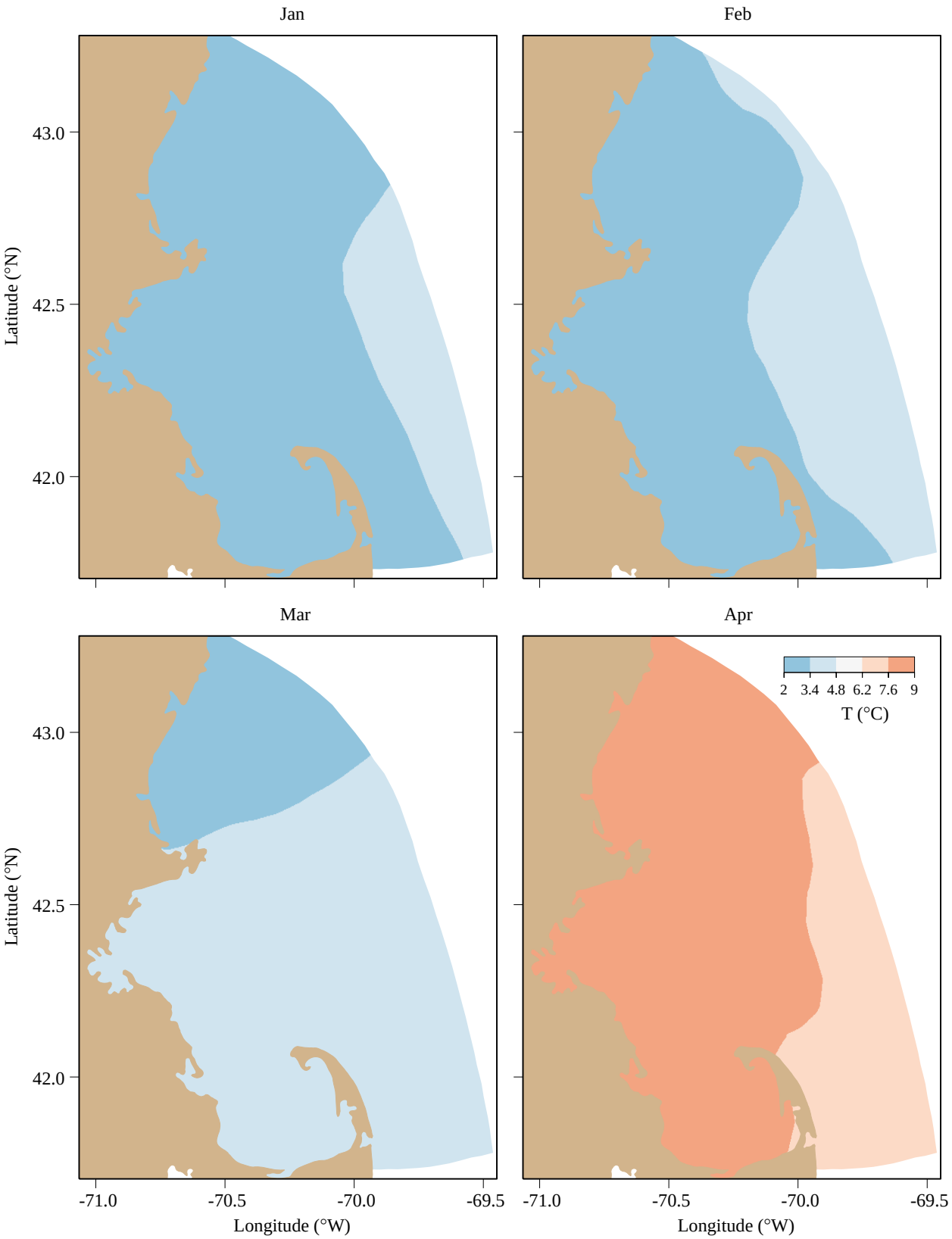

Figure 3. 12 Surface temperature at the end of January, February, March and April, 2009 predicted by FVCOM.

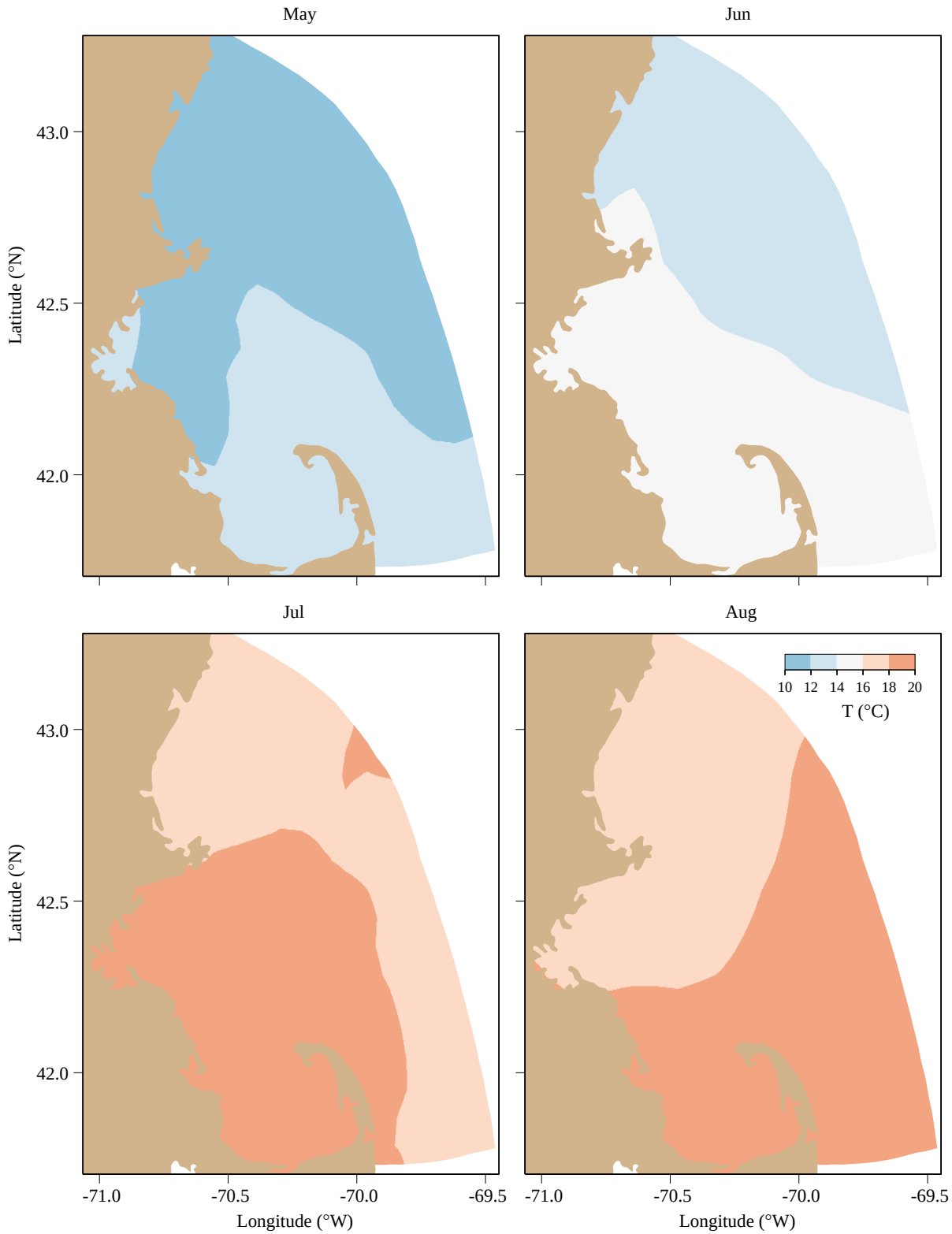

Figure 3. 13 Surface temperature at the end of May, June, July and August, 2009 predicted by FVCOM.

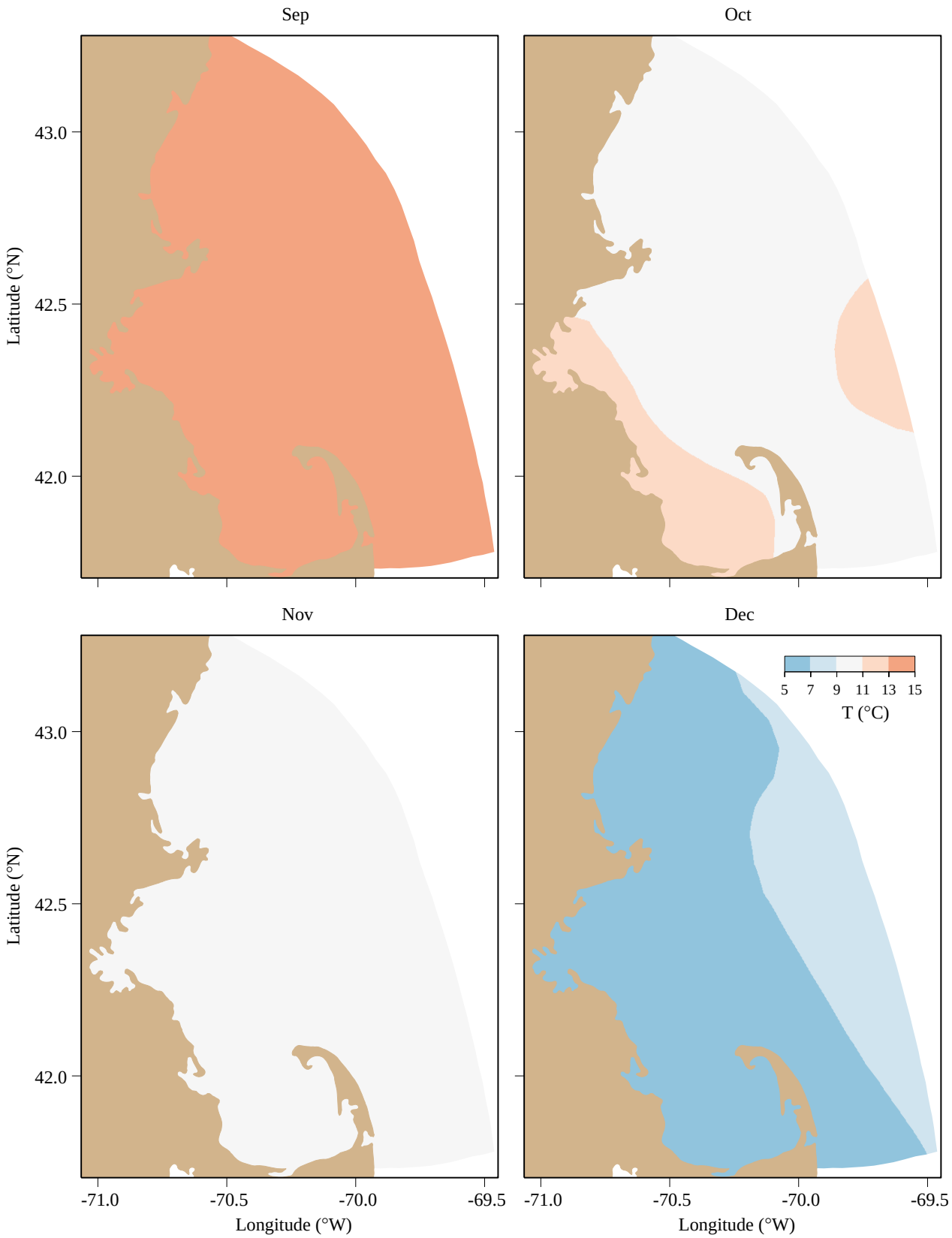

Figure 3. 14 Surface temperature at the end of September, October, November and December, 2009 predicted by FVCOM.

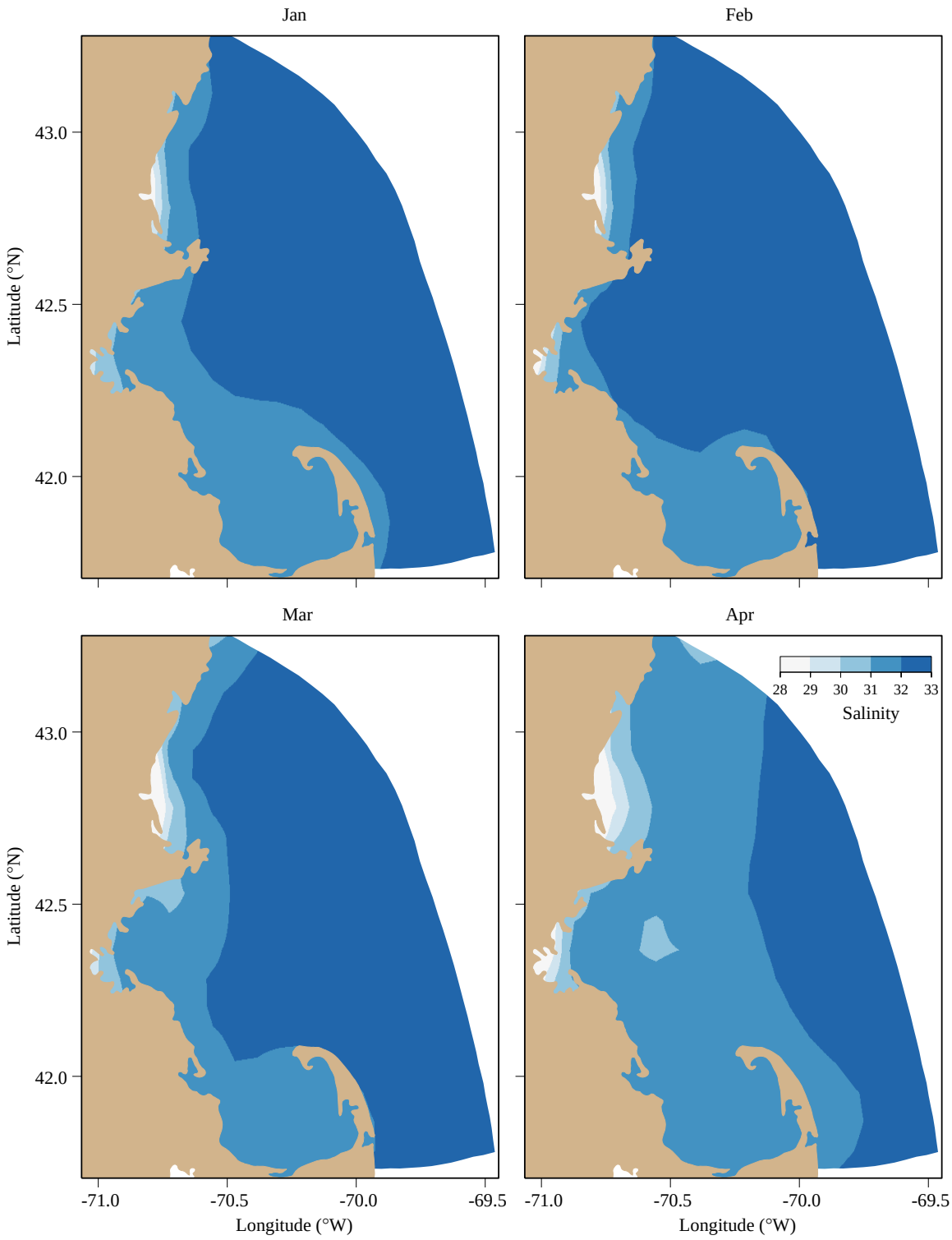

Figure 3. 15 Surface salinity at the end of January, February, March and April, 2009 predicted by FVCOM.

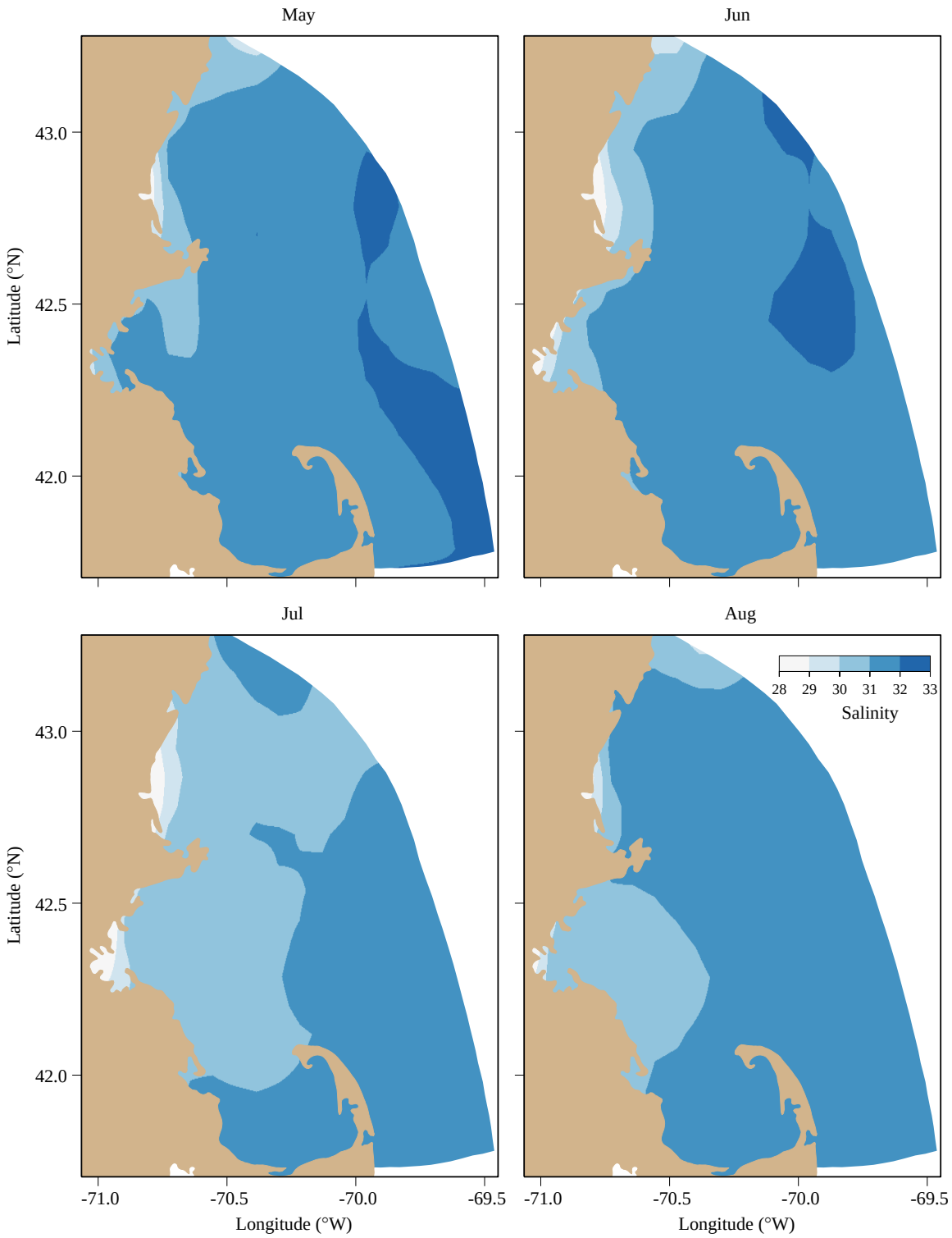

Figure 3. 16 Surface salinity at the end of May, June, July and August, 2009 predicted by FVCOM.

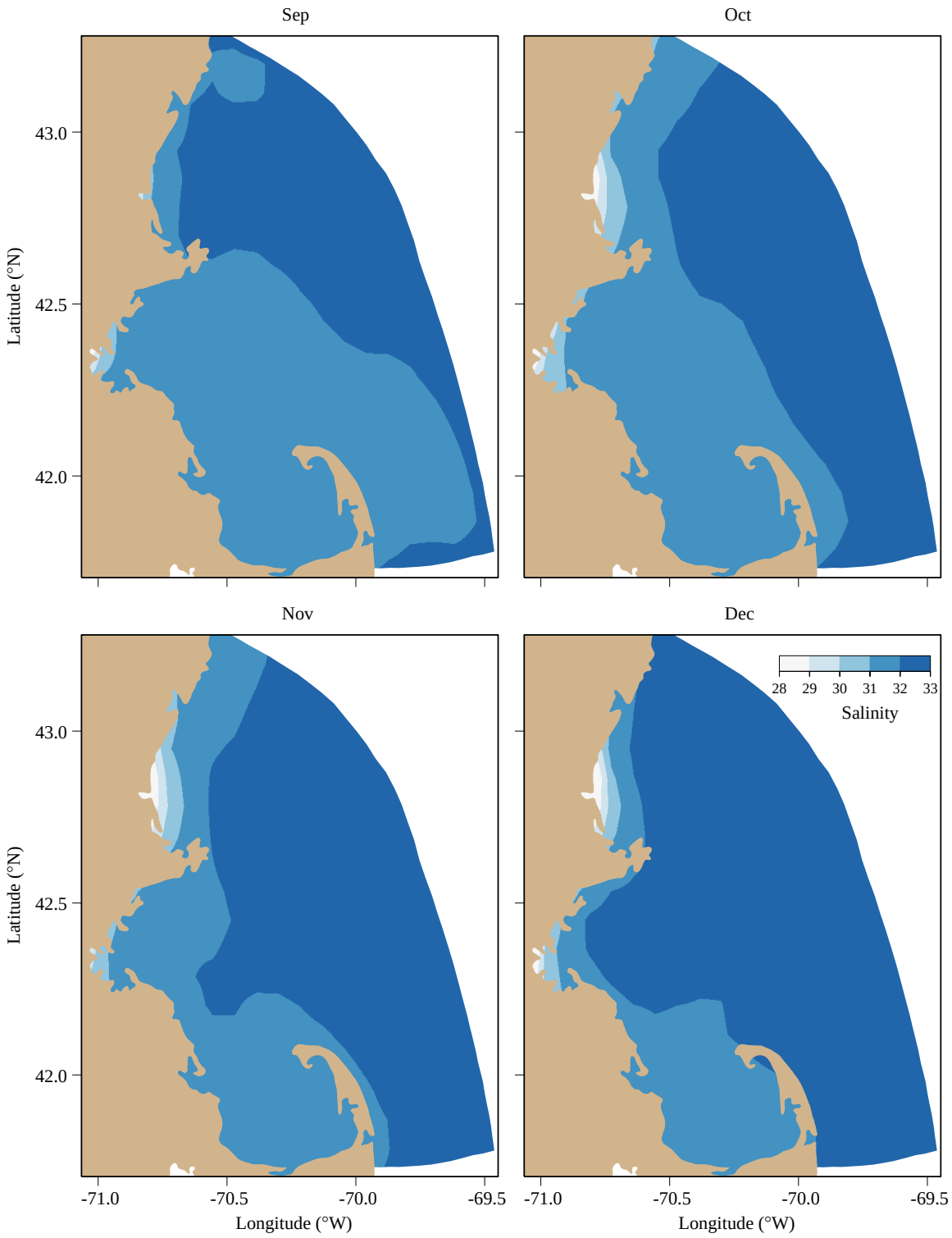

Figure 3. 17 Surface salinity at the end of September, October, November and December, 2009 predicted by FVCOM.

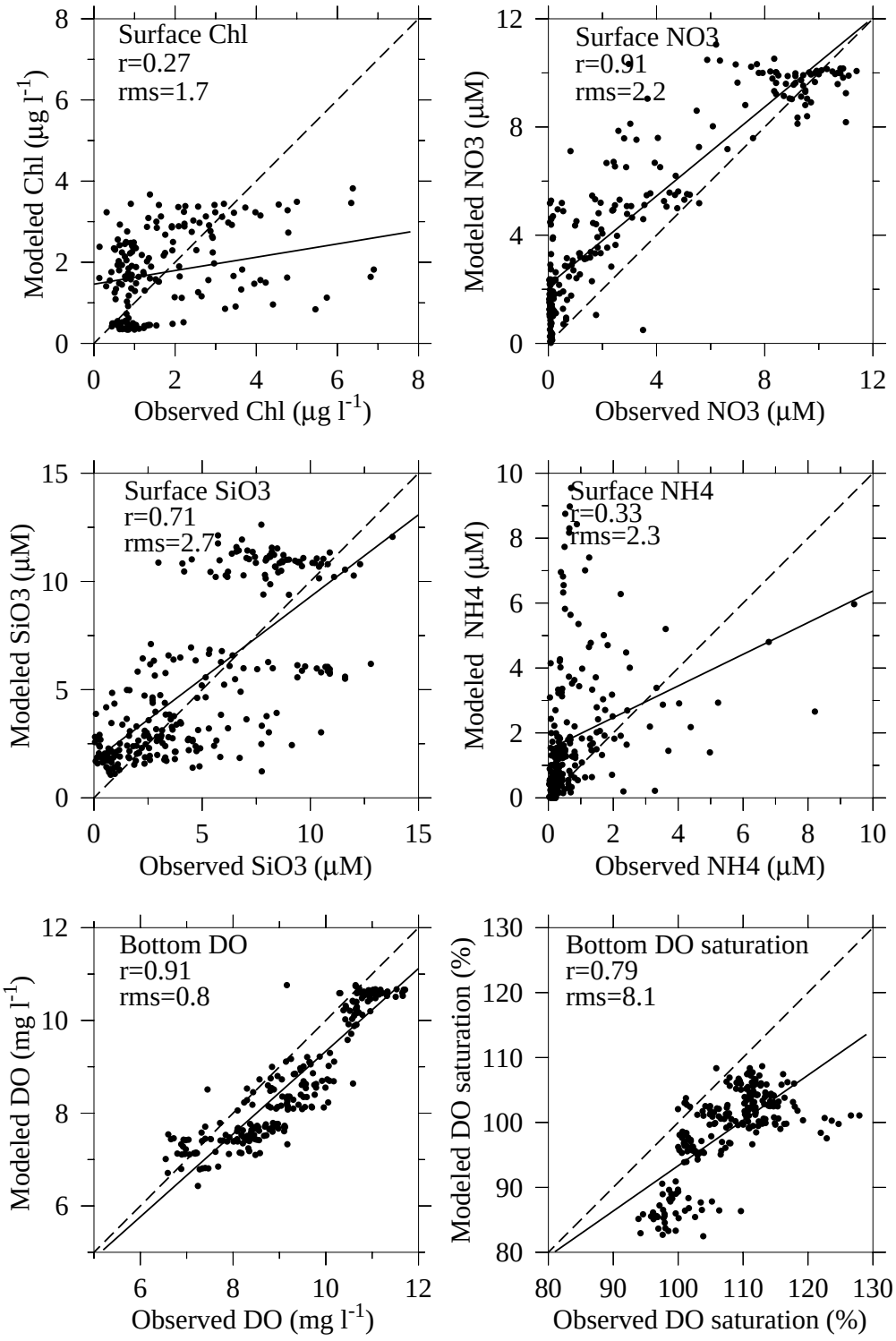

Figure 3. 18 Overall correlation and regression (solid lines) between observed and modeled results of key parameters in 2009. The dashed lines indicate equality between observed and modeled results. All stations are included.

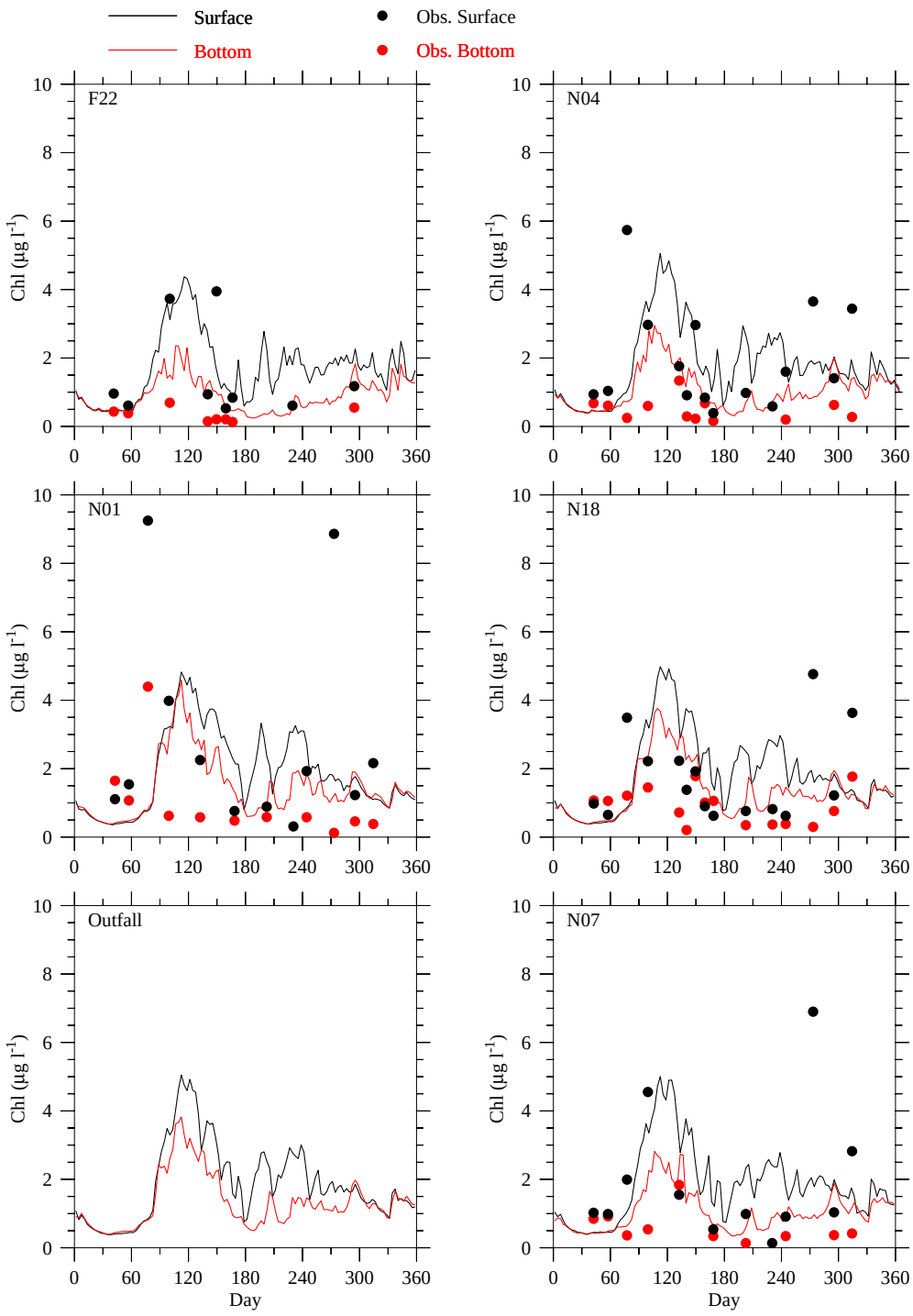

Figure 3. 19 Comparison of chlorophyll observed (dots) and modeled (lines) time-series at the outfall site and selected Massachusetts Bay monitoring stations F22, N04, N01, N18, outfall and N07 for 2009. No chlorophyll data are available at the outfall site.

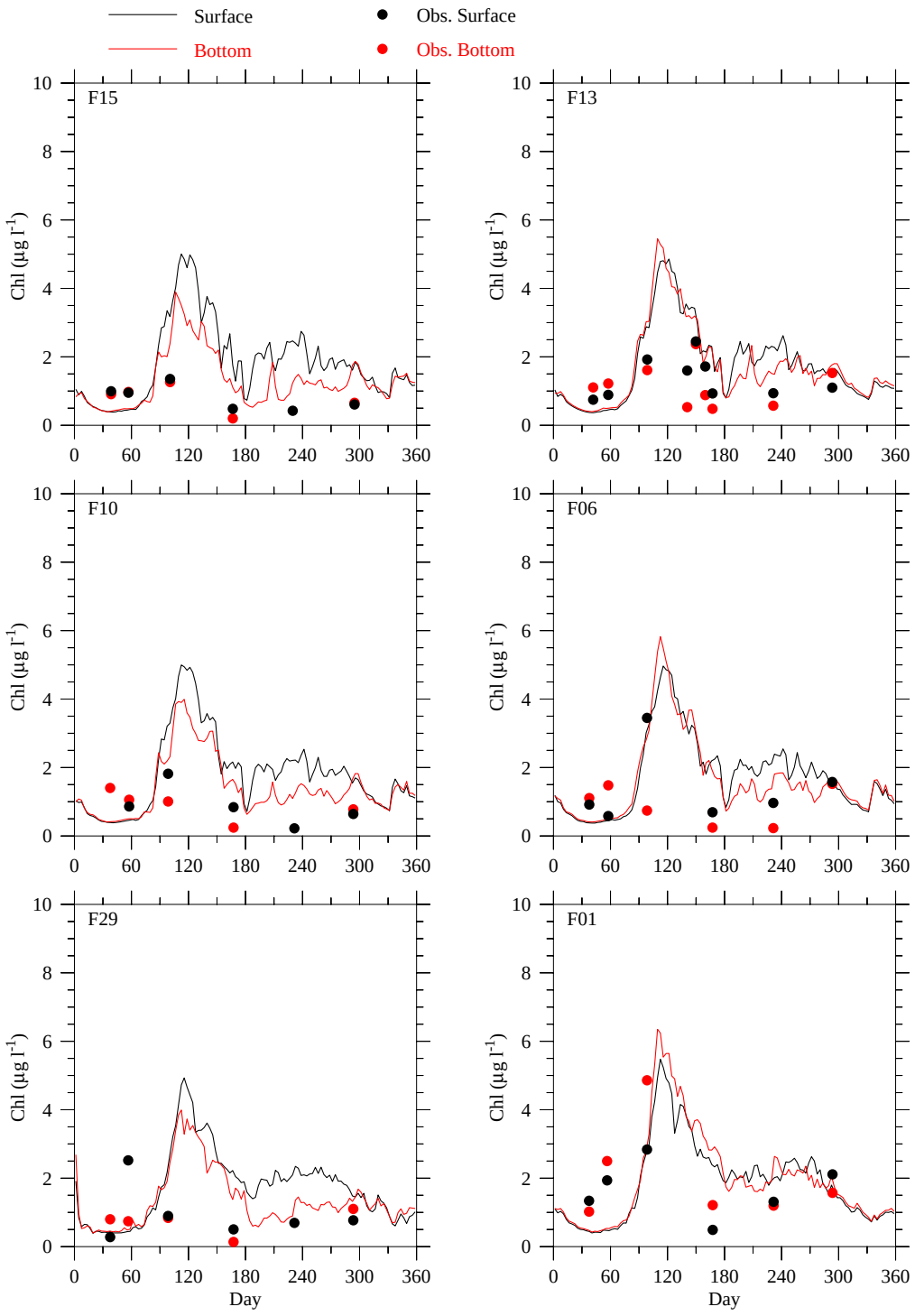

Figure 3. 20 Comparison of chlorophyll observed (dots) and modeled (lines) time-series at selected Massachusetts Bay monitoring stations F15, F13, F10, F06, F29 and F01 for 2009. (Results for stations F15, F10 and F29 are calibrated fluorescence rather than extracted chlorophyll.)

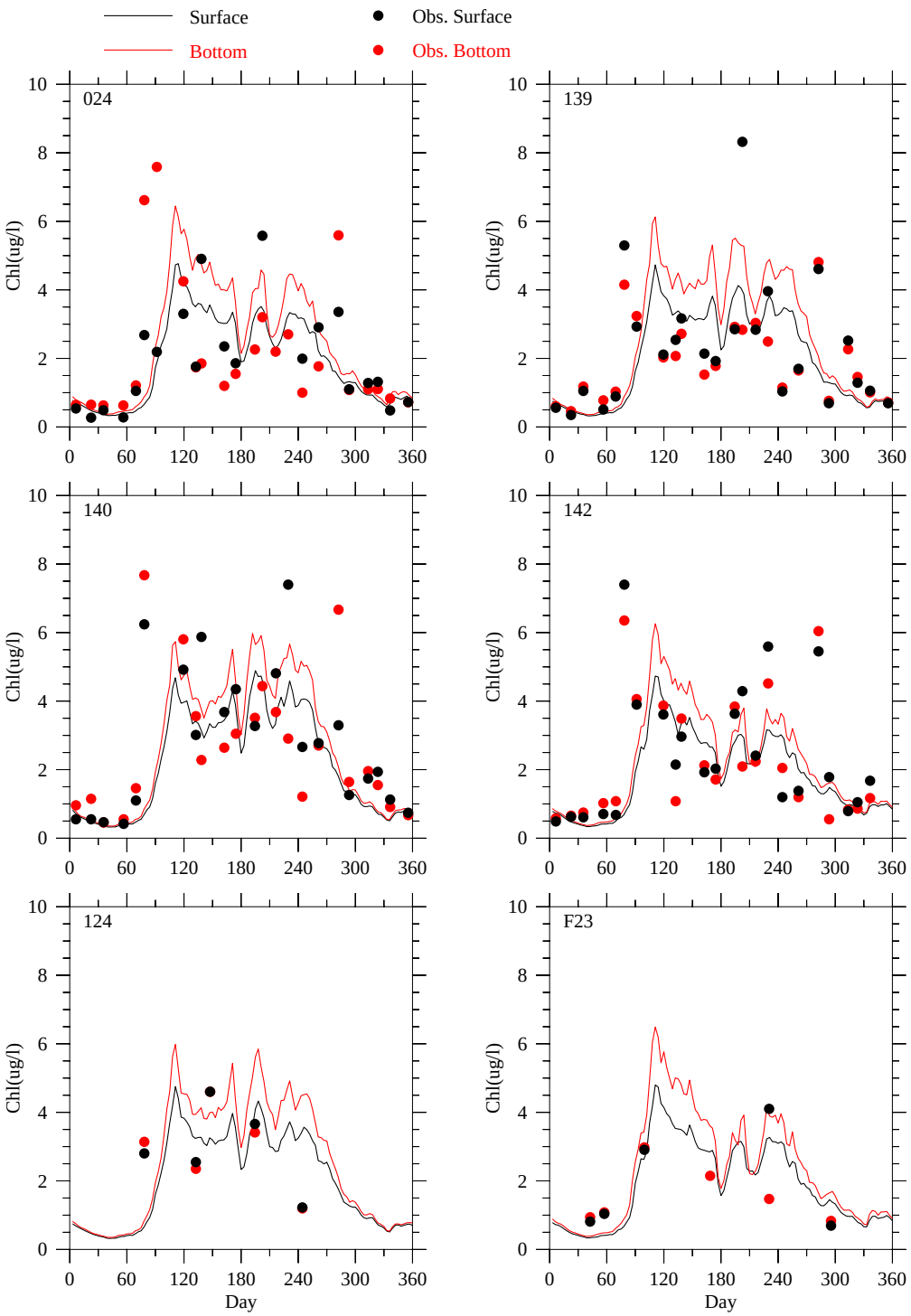

Figure 3. 21 Comparison of chlorophyll observed (dots) and modeled (lines) time-series at selected Boston Harbor stations.

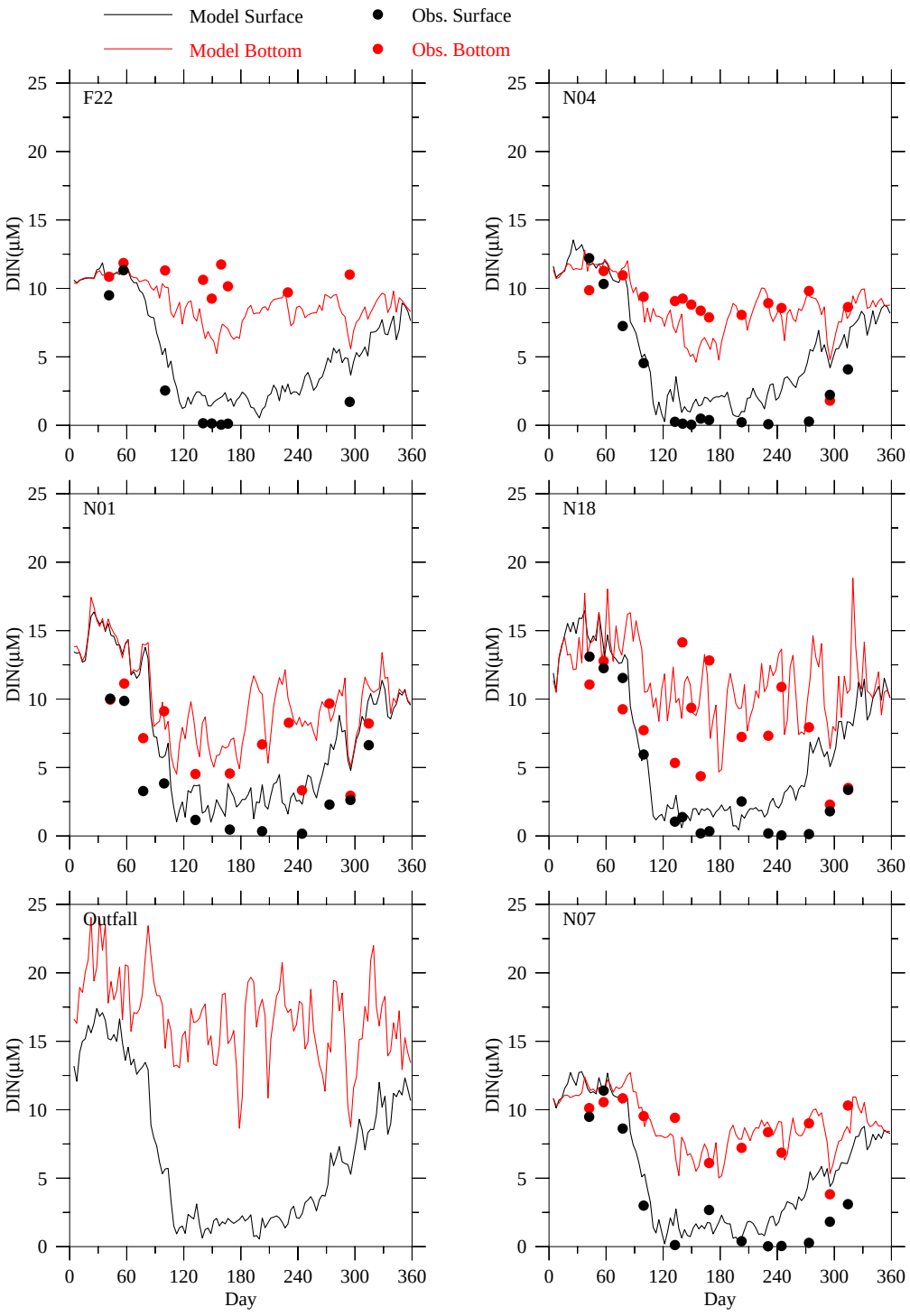

Figure 3. 22 Comparison of DIN observed (dots) and modeled (lines) time-series at the outfall site and selected Massachusetts Bay monitoring stations F22, N04, N01, N18, outfall and N07 for 2009. No DIN data are available at the outfall site.

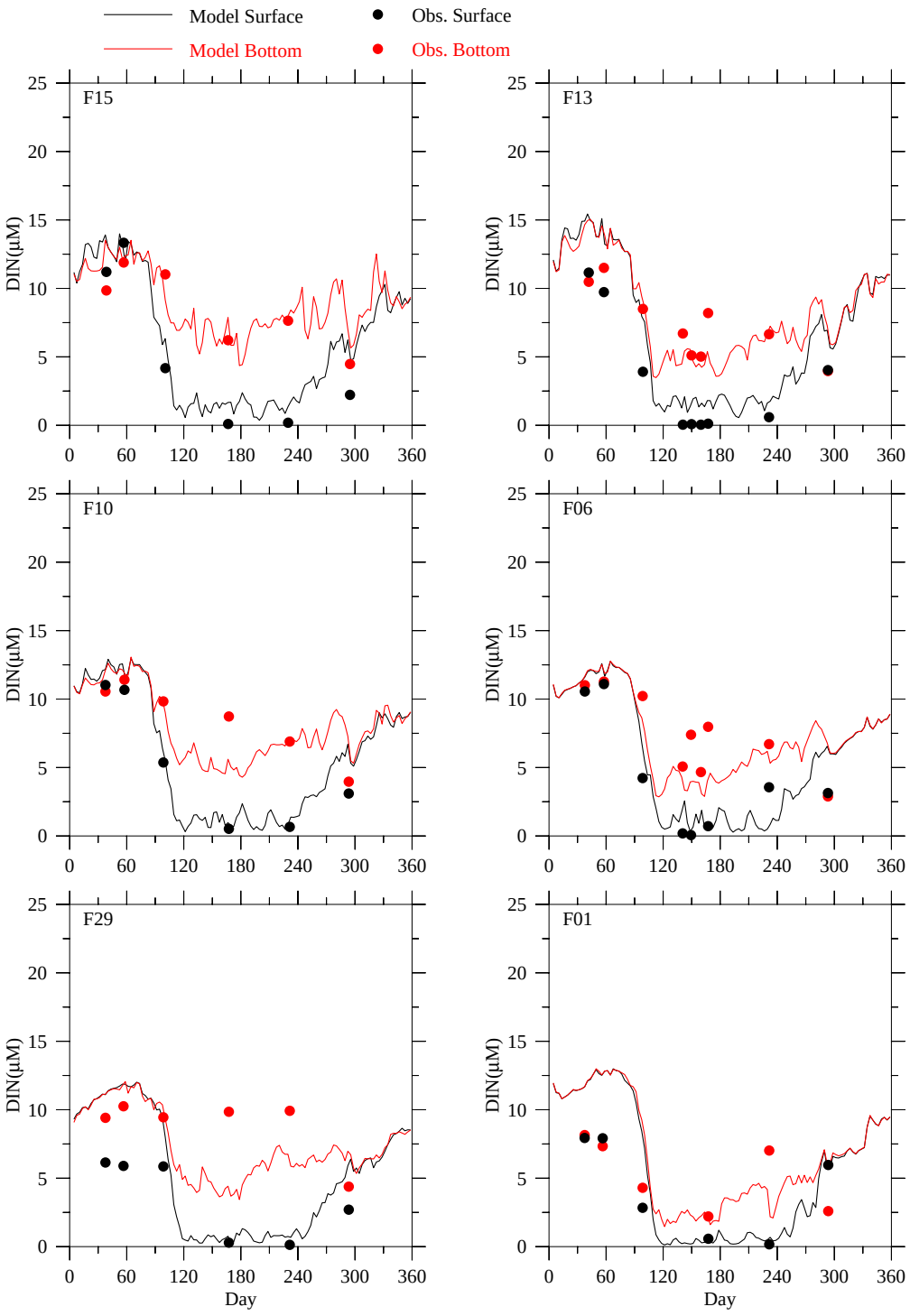

Figure 3. 23 Comparison of DIN observed (dots) and modeled (lines) time-series at selected Massachusetts Bay monitoring stations F15, F13, F10, F06, F29 and F01 for 2009.

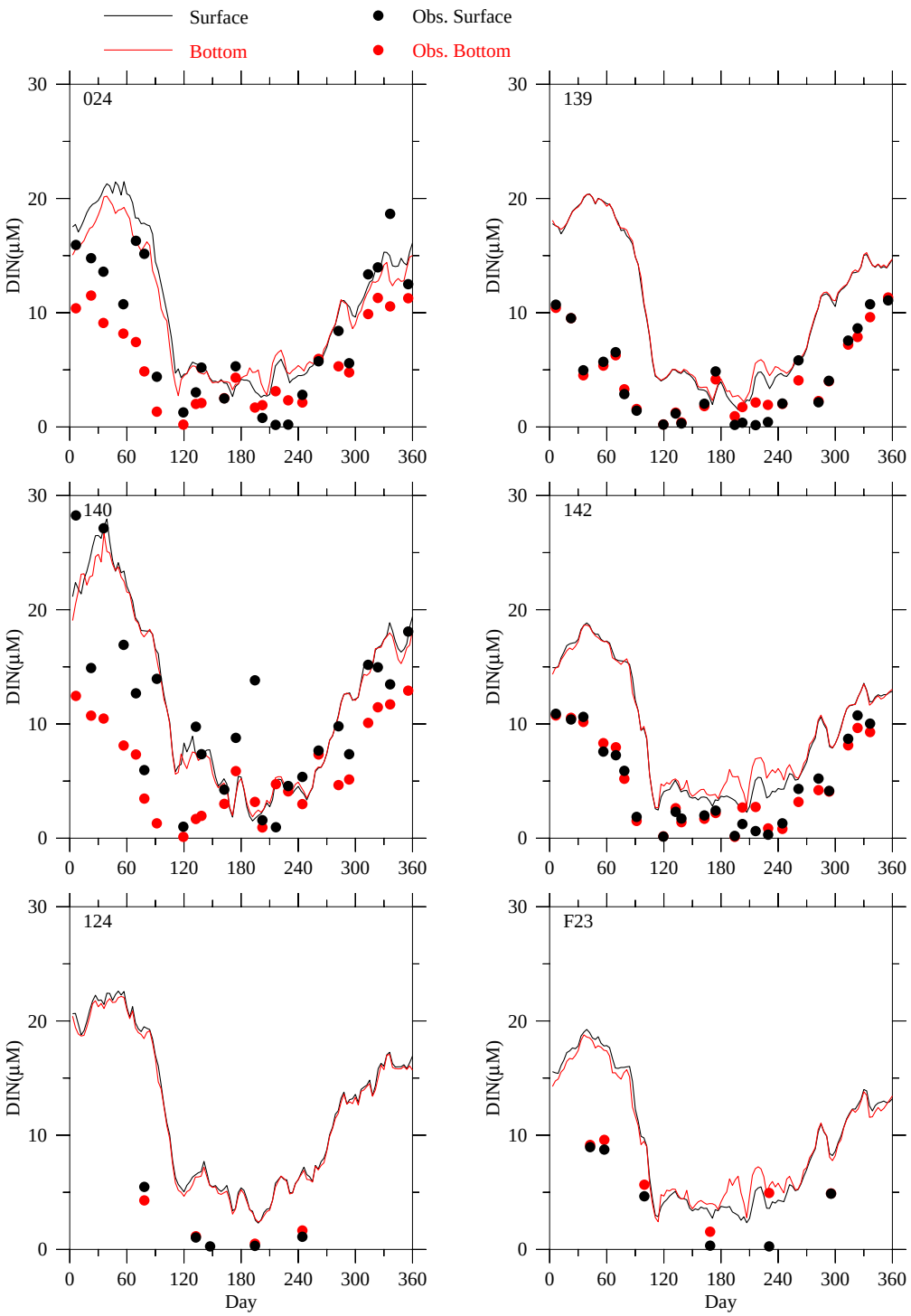

Figure 3. 24 Comparison of DIN observed (dots) and modeled (lines) time-series at selected Boston Harbor stations.

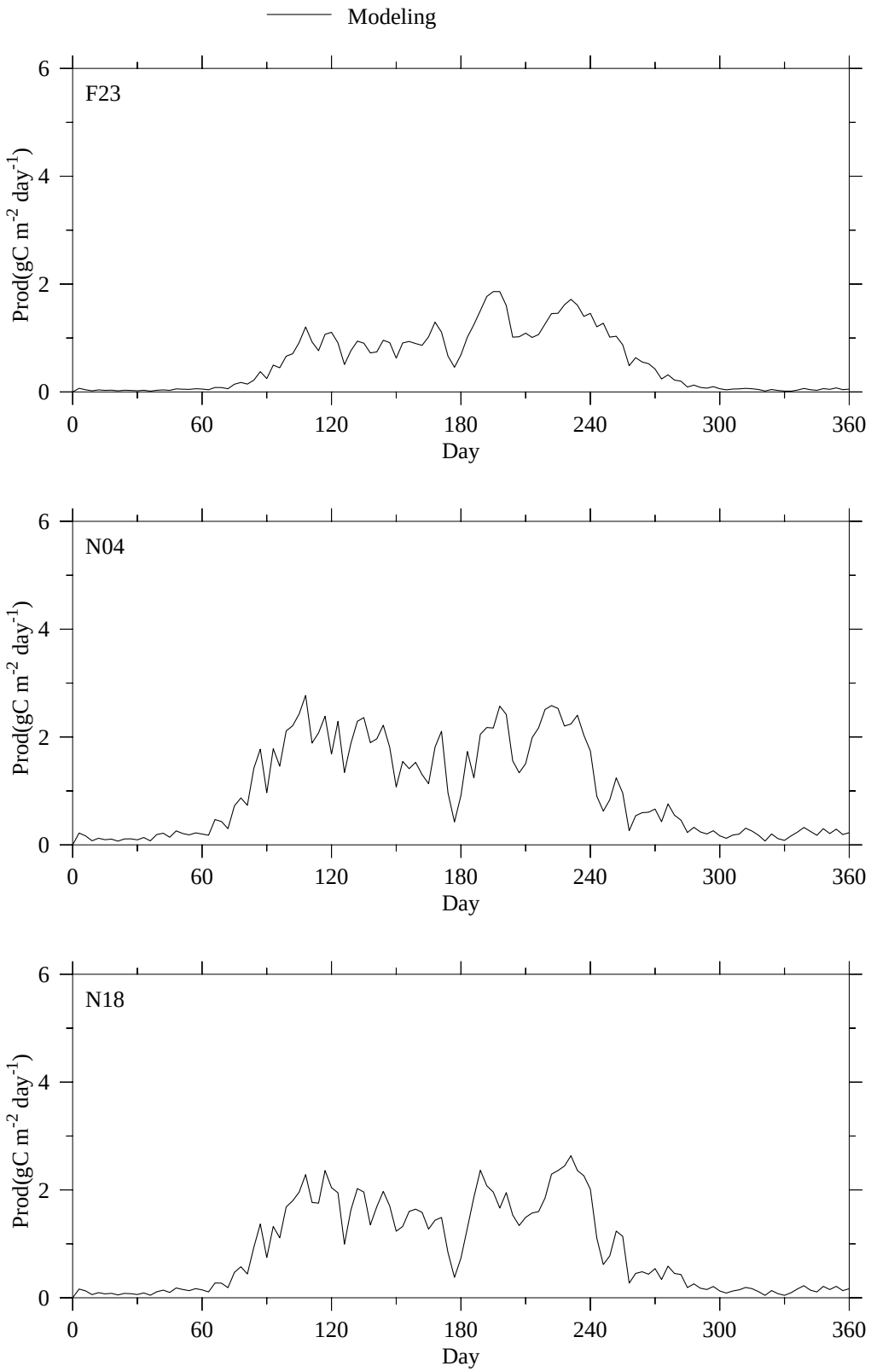

Figure 3. 25 Model-simulated vertically integrated primary production at the MWRA monitoring stations.

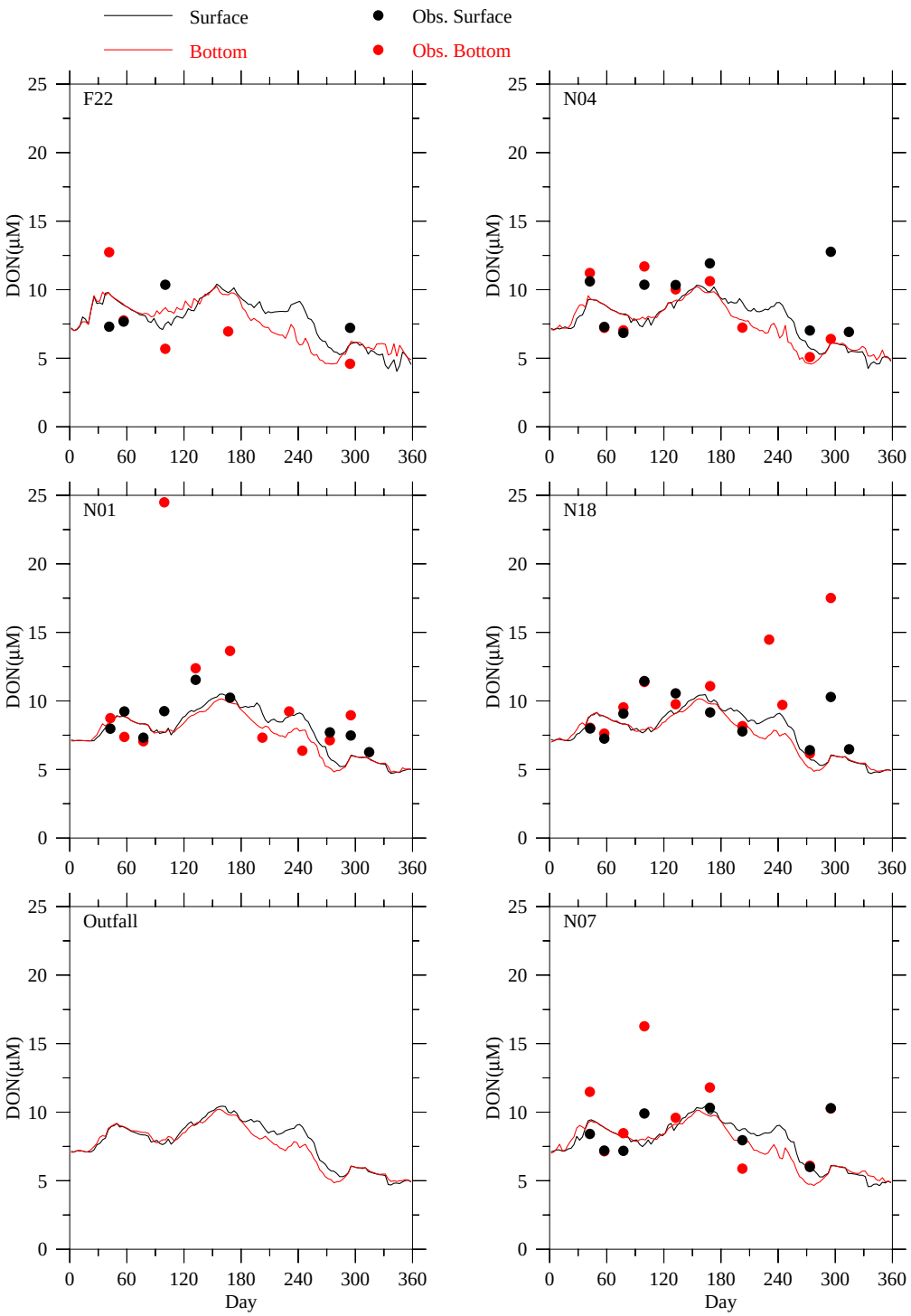

Figure 3. 26 Comparison of DON observed (dots) and modeled (lines) time-series at the outfall site and selected Massachusetts Bay monitoring stations F22, N04, N01, N18, outfall and N07 for 2009. No DON data are available at the outfall site.

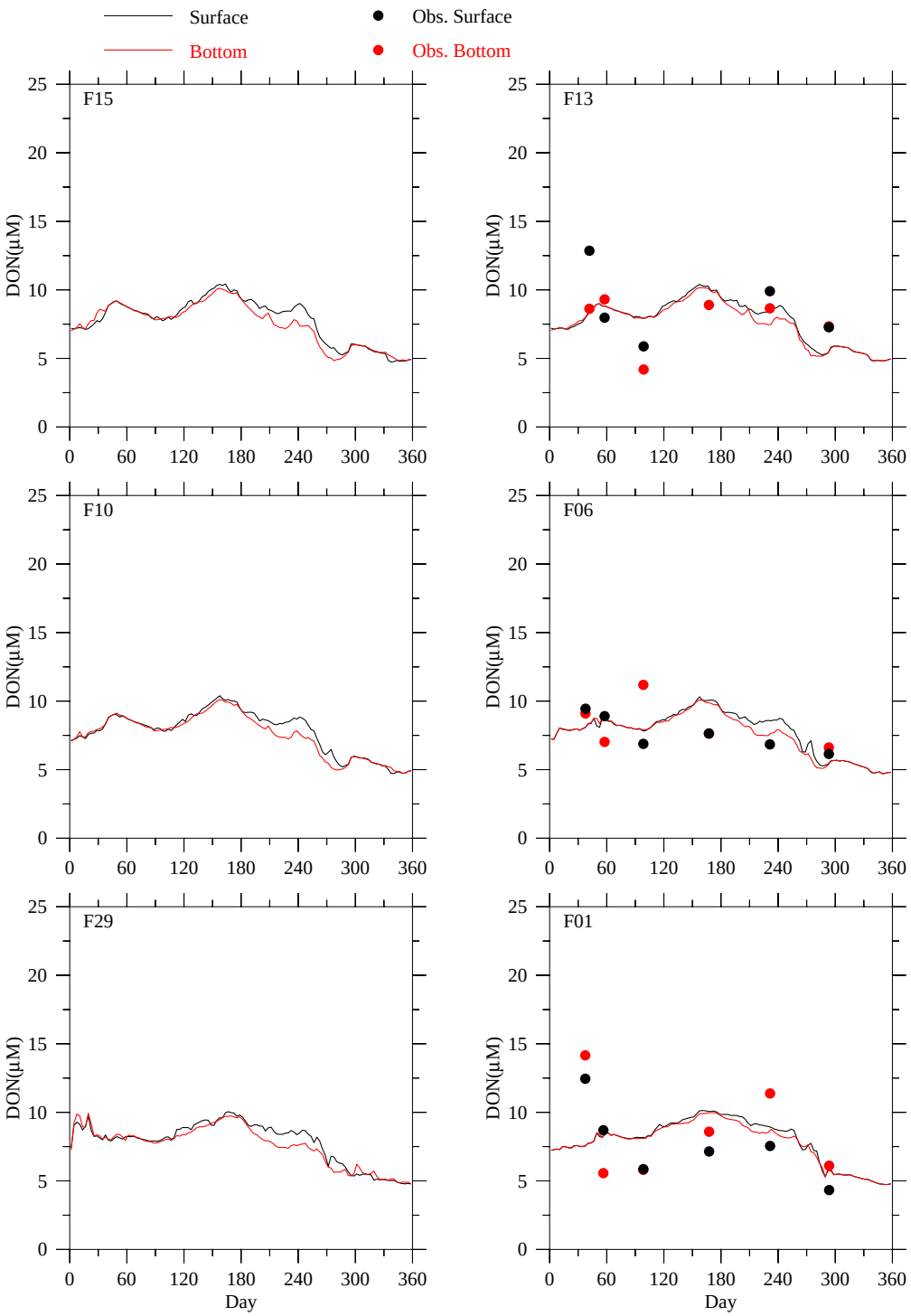

Figure 3. 27 Comparison of DON observed (dots) and modeled (lines) time-series at selected Massachusetts Bay monitoring stations F15, F13, F10, F06, F29 and F01 for 2009. No DON data are available at stations F15, F10 and F29.

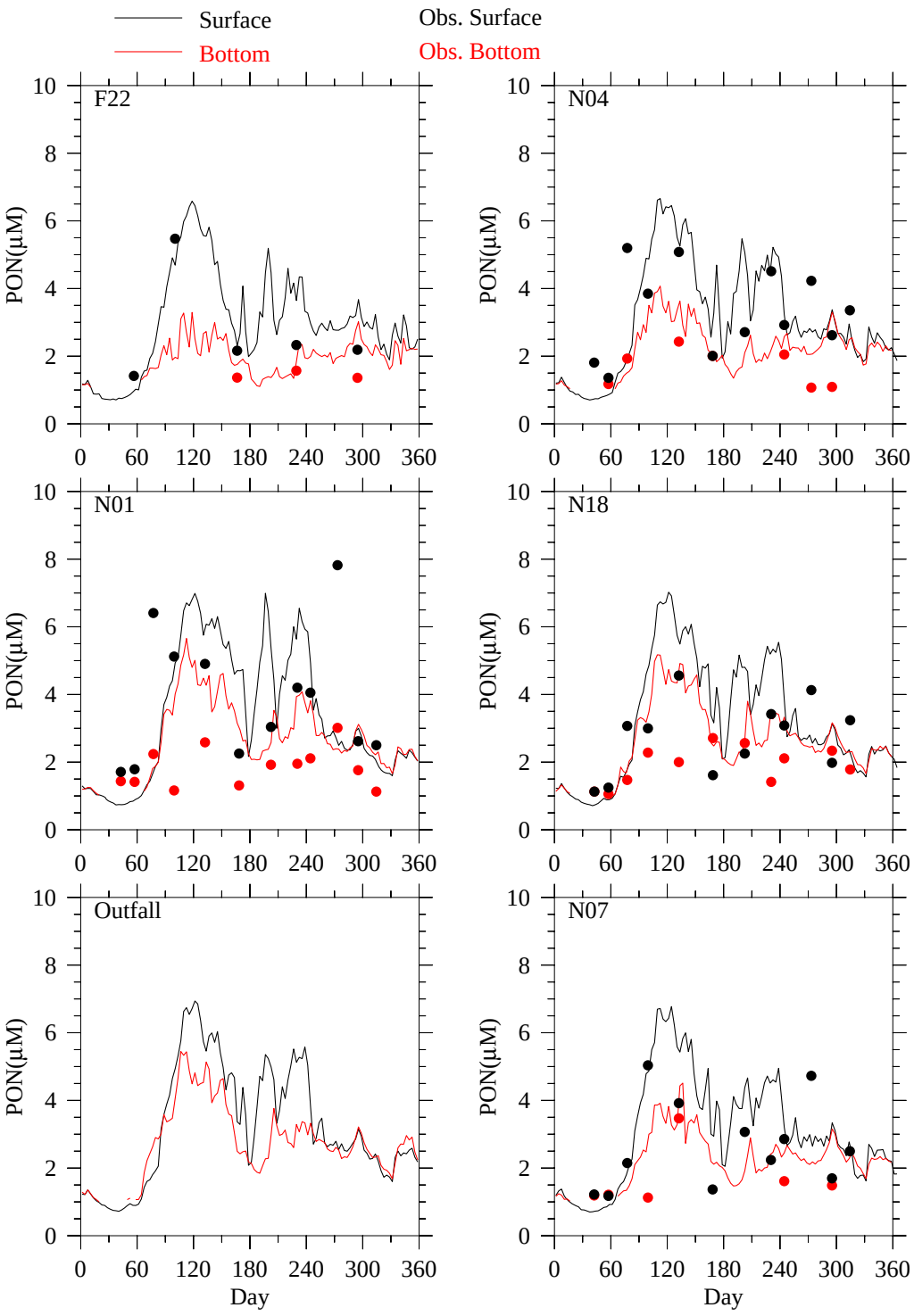

Figure 3. 28 Comparison of PON observed (dots) and modeled (lines) time-series at the outfall site and selected Massachusetts Bay monitoring stations F22, N04, N01, N18, outfall and N07 for 2009. No PON data are available at the outfall site.

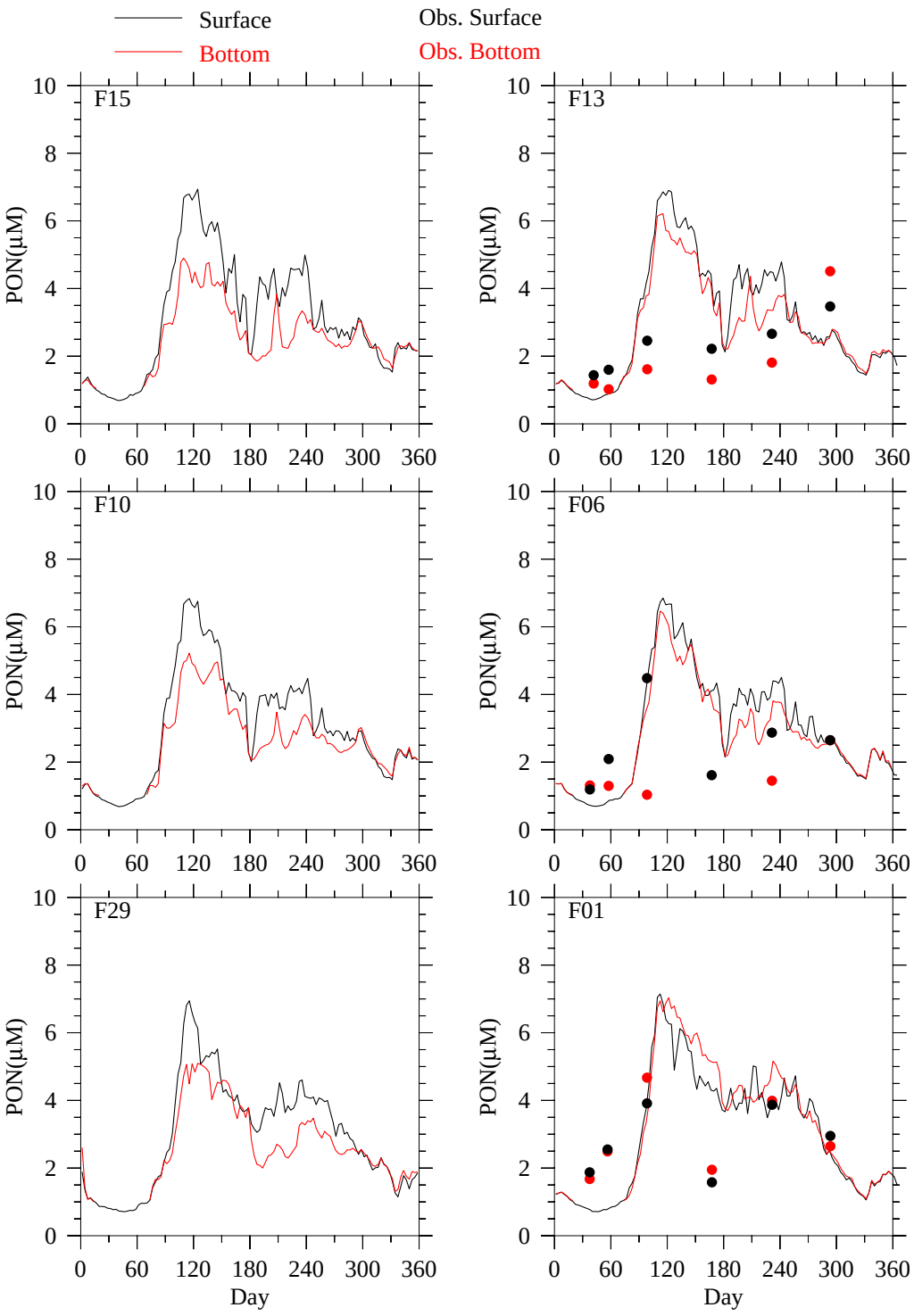

Figure 3. 29 Comparison of PON observed (dots) and modeled (lines) time-series at selected Massachusetts Bay monitoring stations F15, F13, F10, F06, F29 and F01 for 2009. No PON data are available at stations F15, F10 and F29.

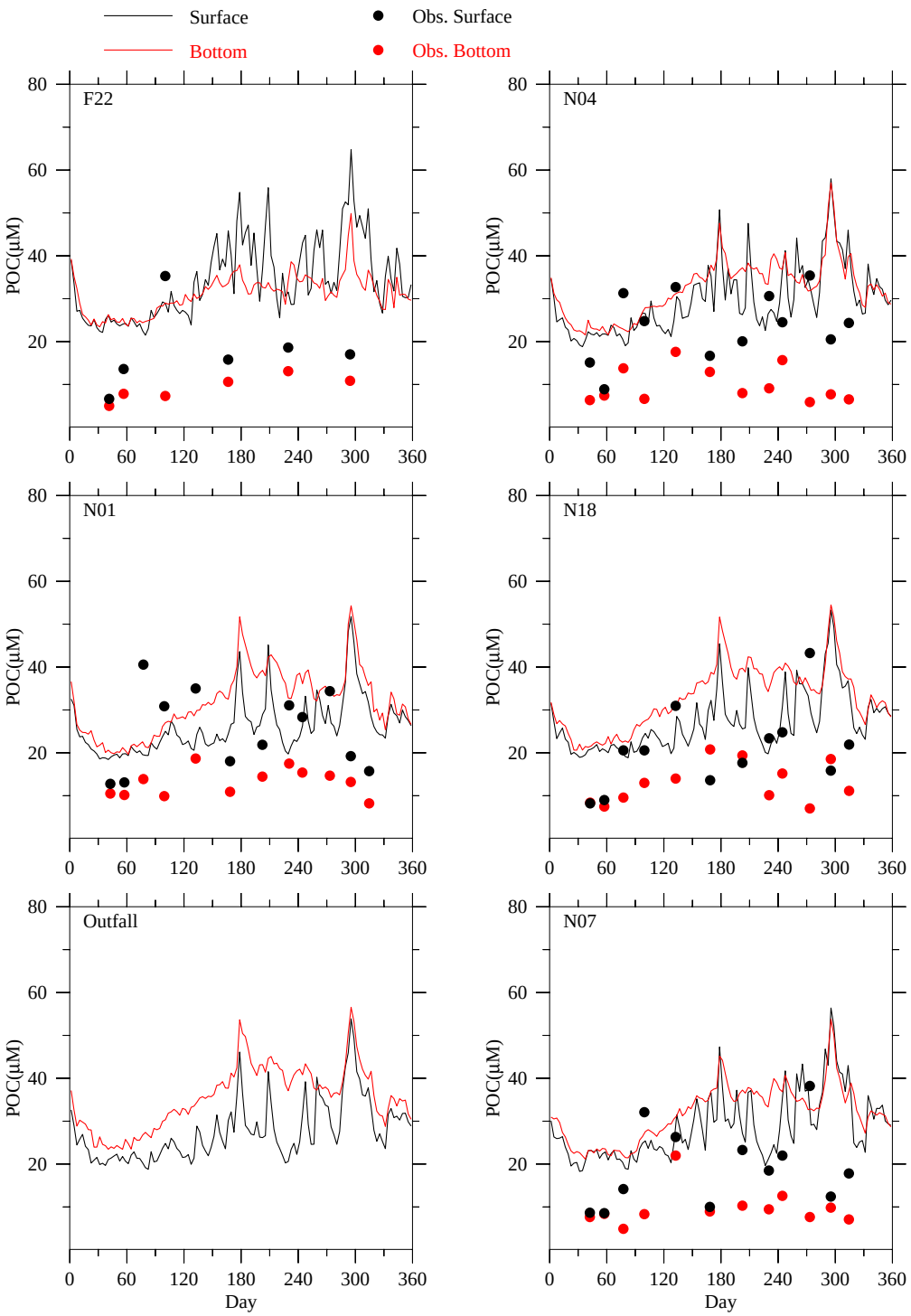

Figure 3. 30 Comparison of POC observed (dots) and modeled (lines) time-series at the outfall site and selected Massachusetts Bay monitoring stations F22, N04, N01, N18, outfall and N07 for 2009. No PON data are available at the outfall site.

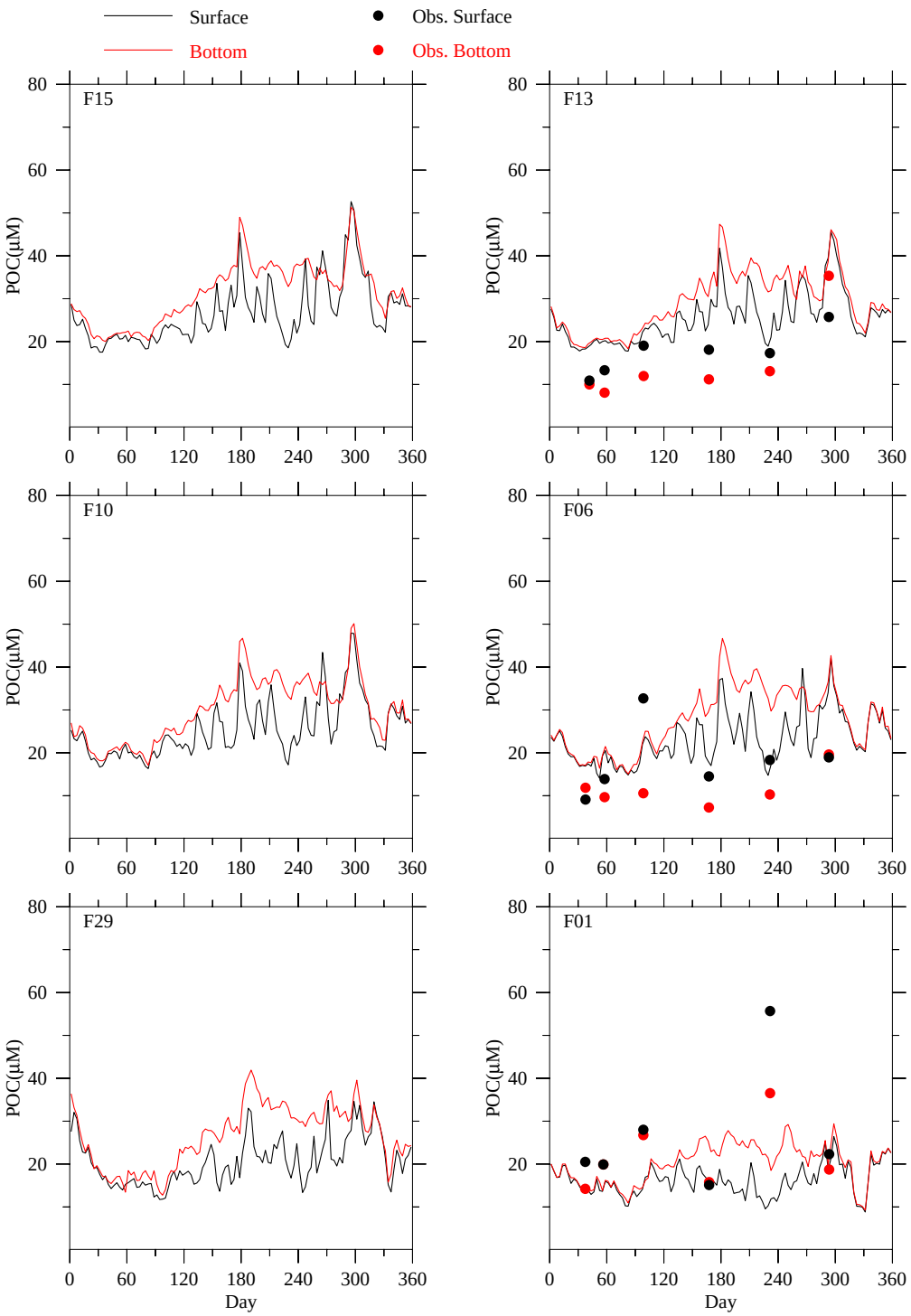

Figure 3. 31 Comparison of POC observed (dots) and modeled (lines) time-series at selected Massachusetts Bay monitoring stations F15, F13, F10, F06, F29 and F01 for 2009. No PON data are available at stations F15, F10 and F29.

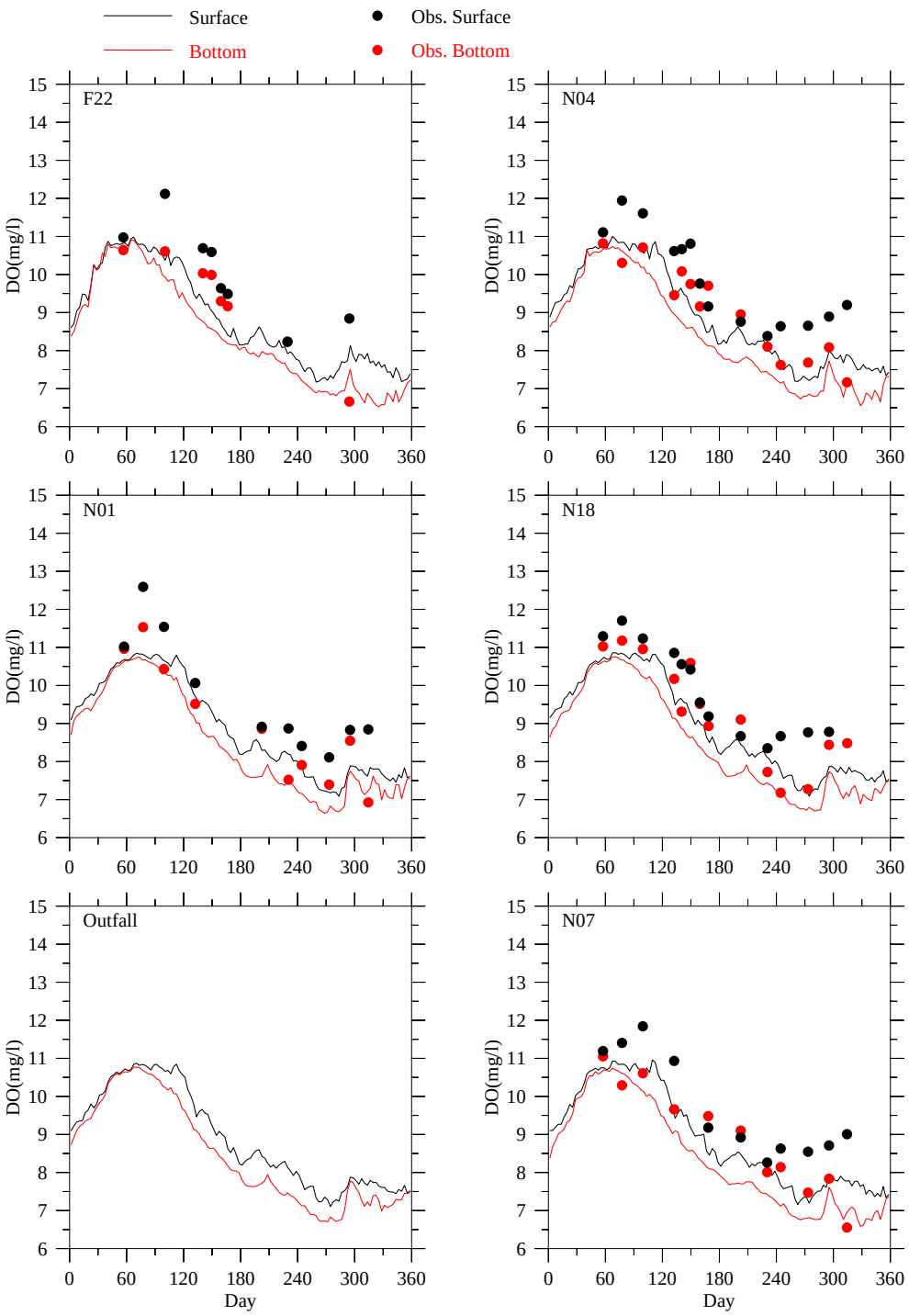

Figure 3. 32 Comparison of DO observed (dots) and modeled (lines) time-series at the outfall site and selected Massachusetts Bay monitoring stations F22, N04, N01, N18, outfall and N07 for 2009. No DO data are available at the outfall site.

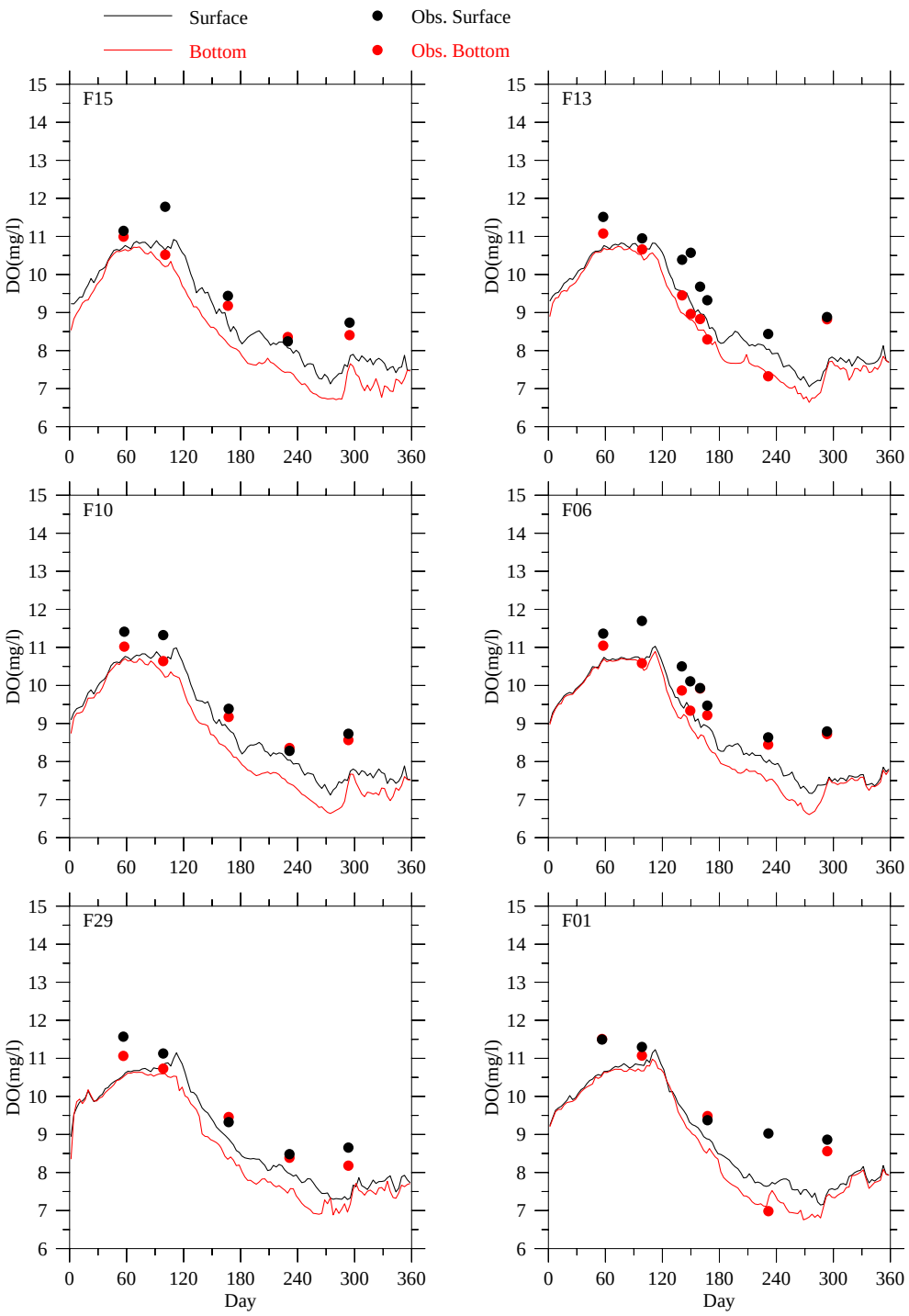

Figure 3. 33 Comparison of DO observed (dots) and modeled (lines) time-series at selected Massachusetts Bay monitoring stations F15, F13, F10, F06, F29 and F01 for 2009.

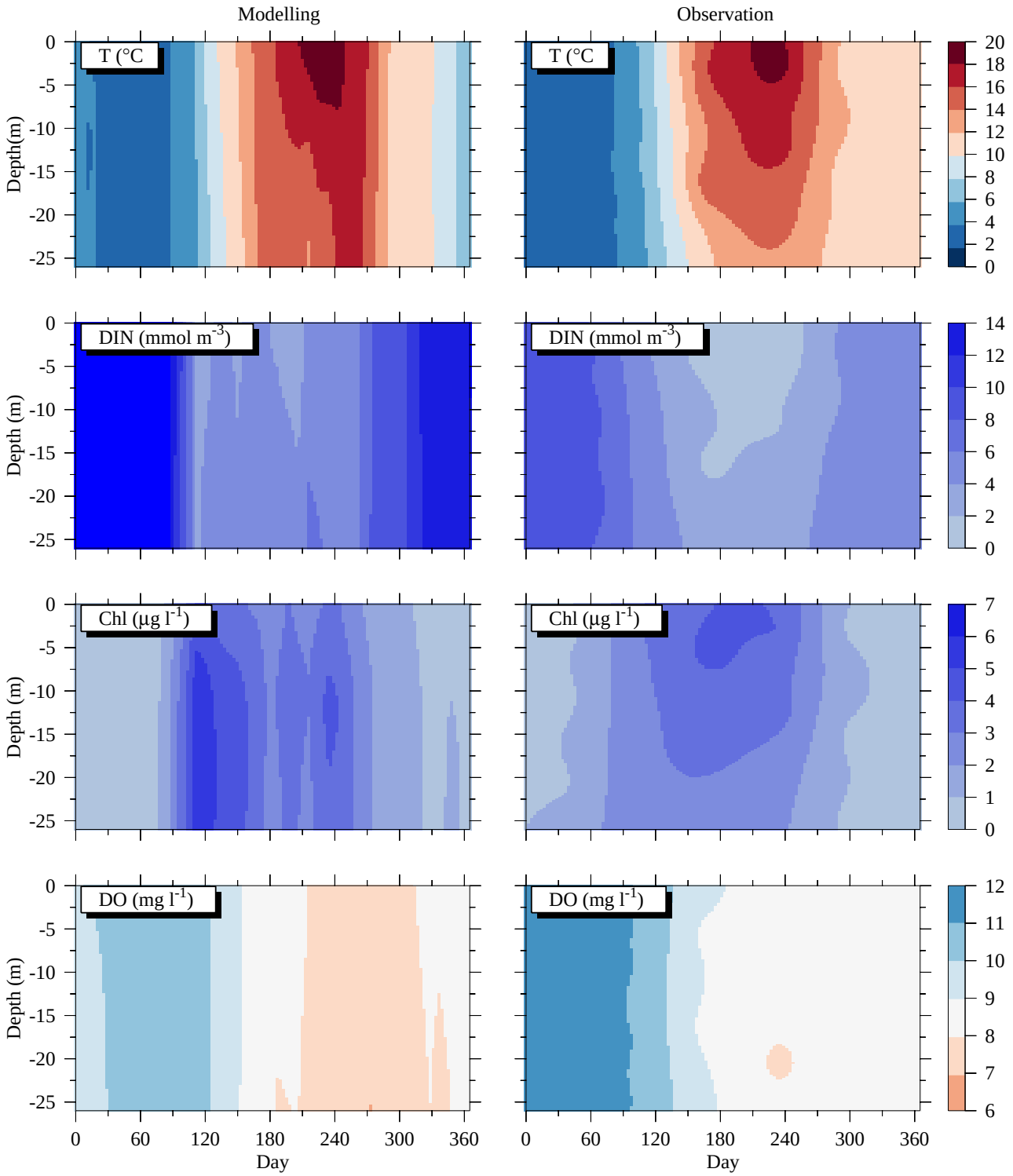

Figure 3. 34 Time-series of vertical distribution of modeled (left panels) and observed (right panels) key parameters (T, DIN, Chl and DO) in the water column at the far-field station F23 in 2009.

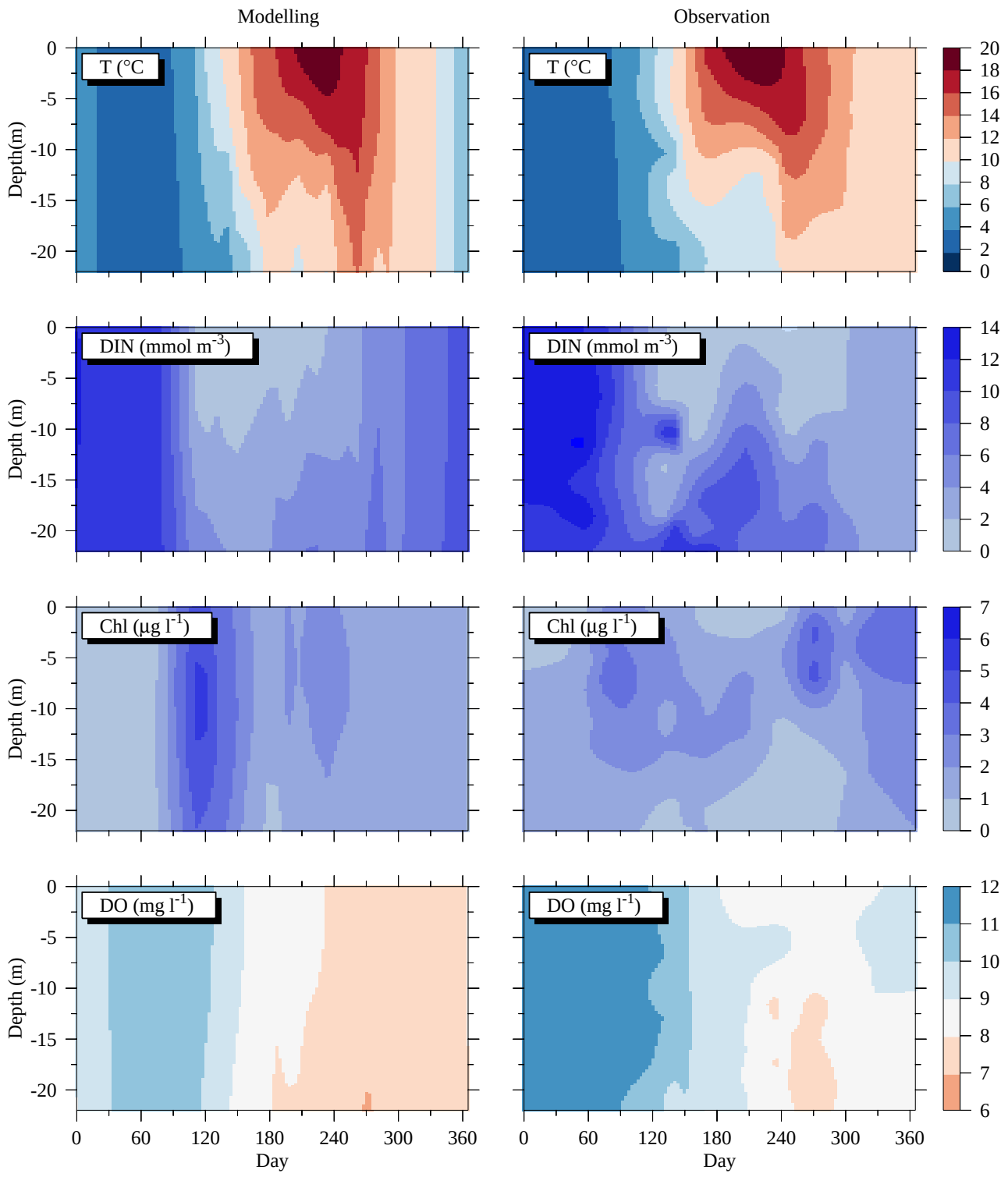

Figure 3. 35 Time-series of vertical distribution of modeled (left panels) and observed (right panels) key parameters (T, DIN, Chl and DO) in the water column at the near-field station N18 in 2009.

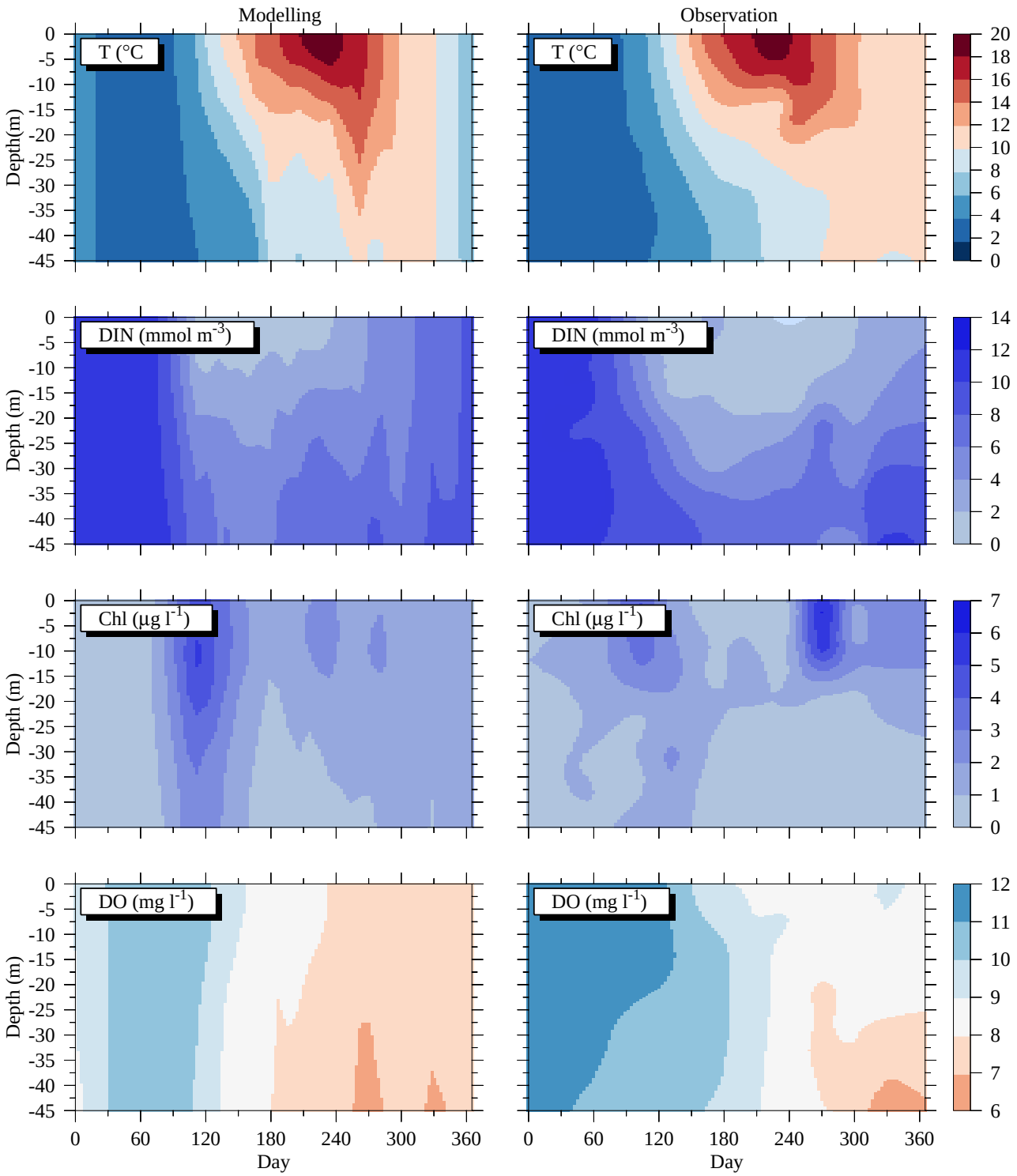

Figure 3. 36 Time-series of vertical distribution of modeled (left panels) and observed (right panels) key parameters (T, DIN, Chl and DO) in the water column at the near-field station N07 in 2009.

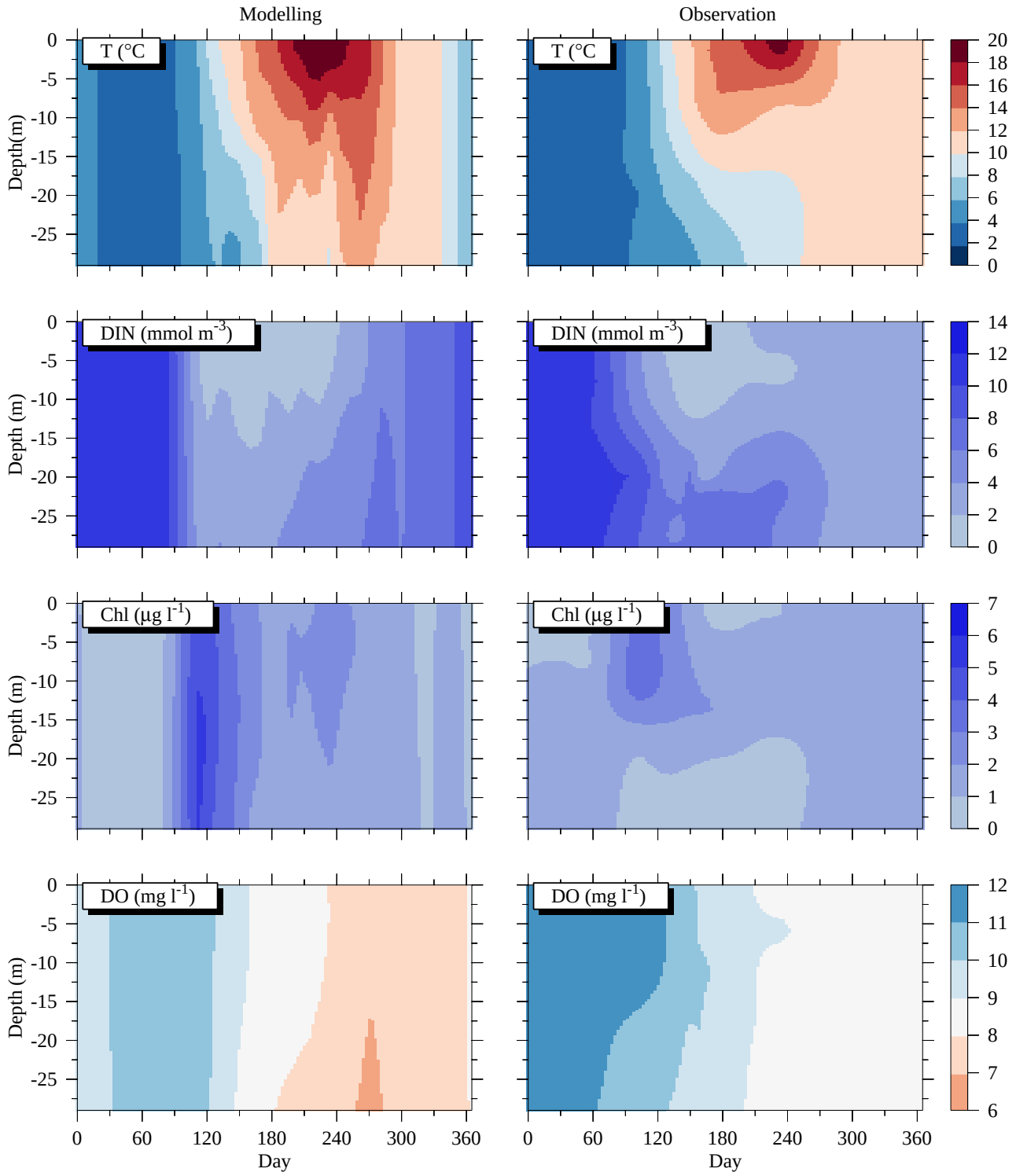

Figure 3. 37 Time-series of vertical distribution of modeled (left panels) and observed (right panels) key parameters (T, DIN, Chl and DO) in the water column at the far-field station F06 in 2009.

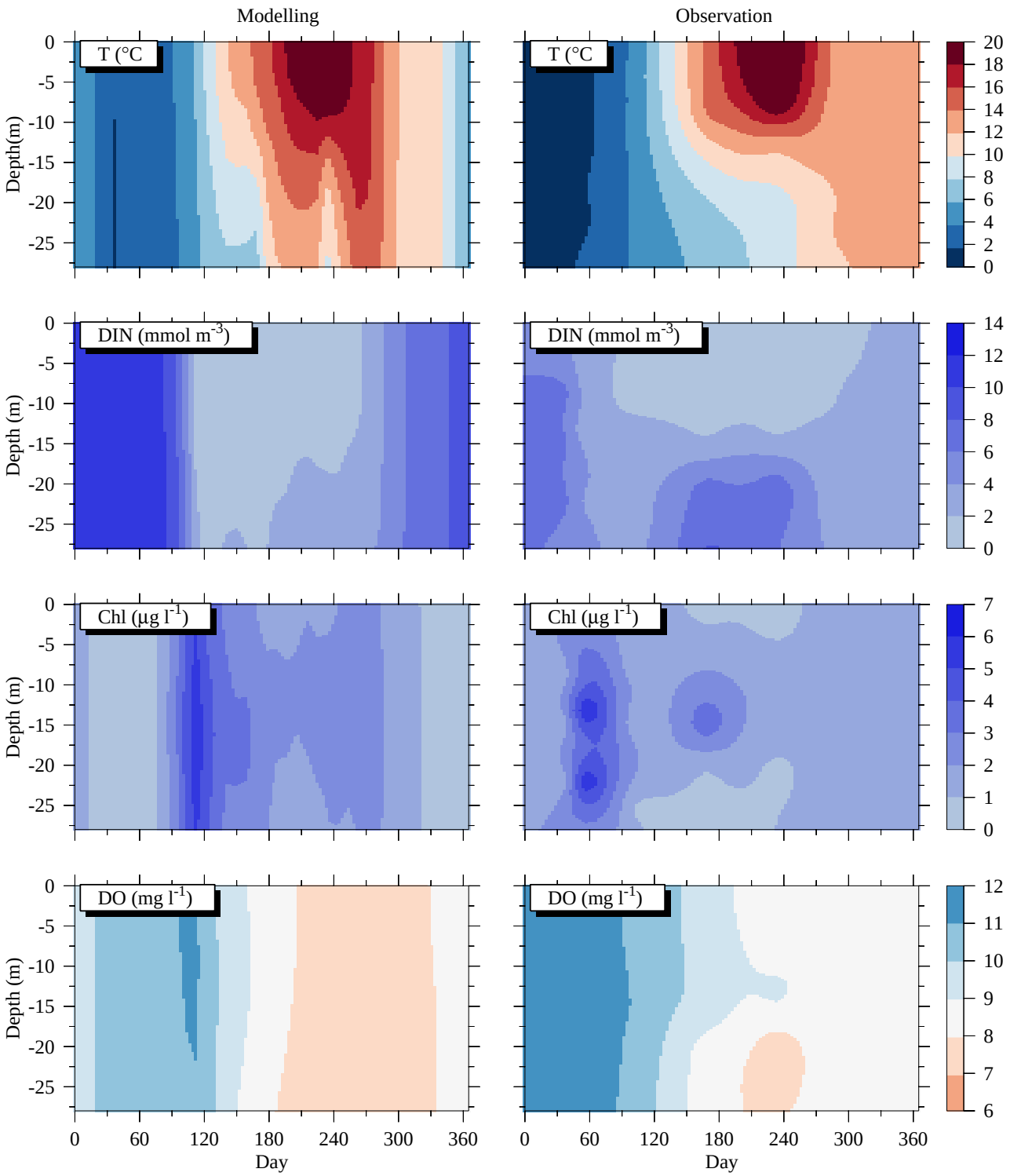

Figure 3. 38 Time-series of vertical distribution of modeled (left panels) and observed (right panels) key parameters (T, DIN, Chl and DO) in the water column at the far-field station F02 in 2009.

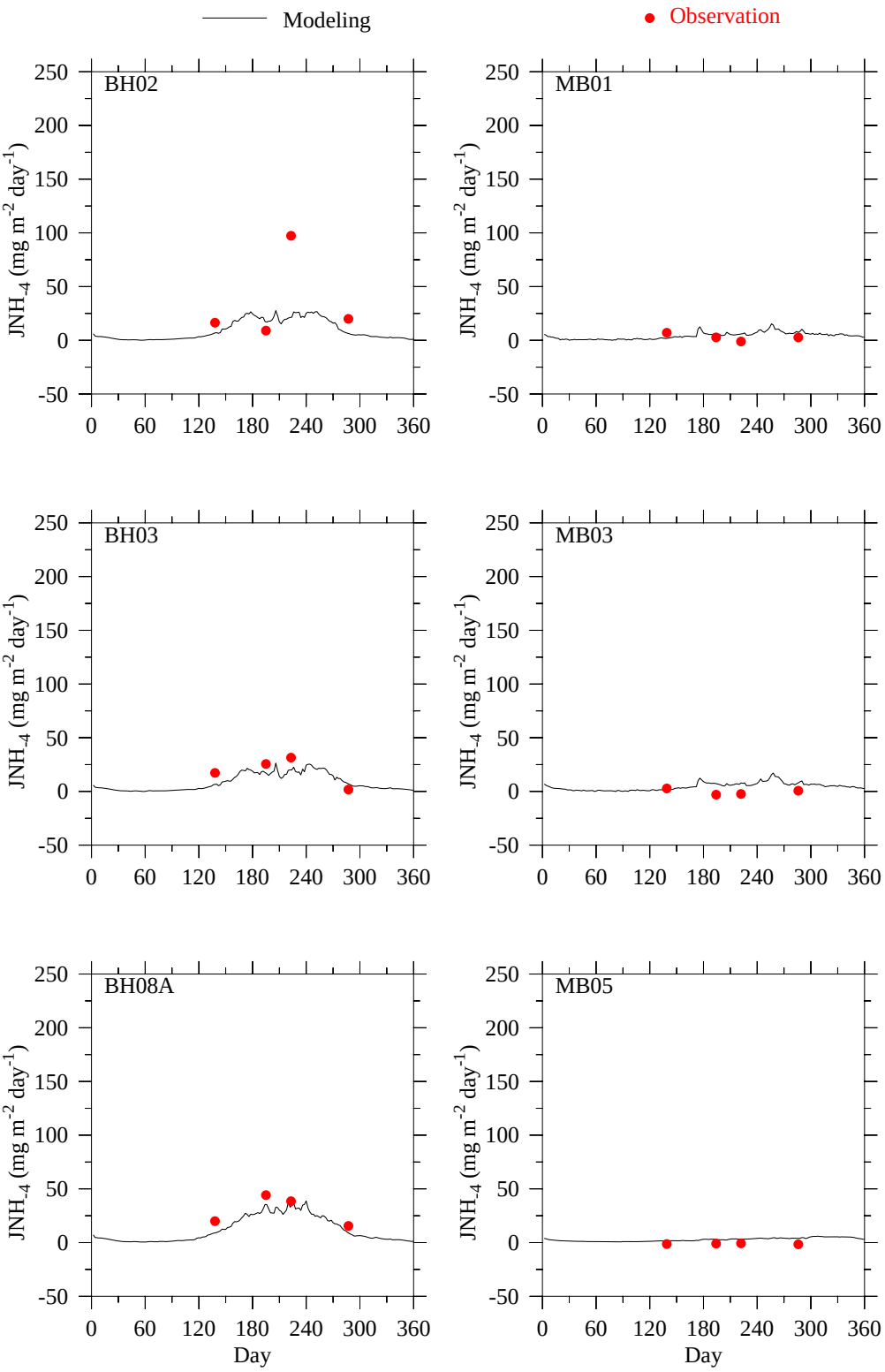

Figure 3. 39 Comparison of sediment NH_4^+ flux observed (dots) and modeled (lines) time-series in 2009.

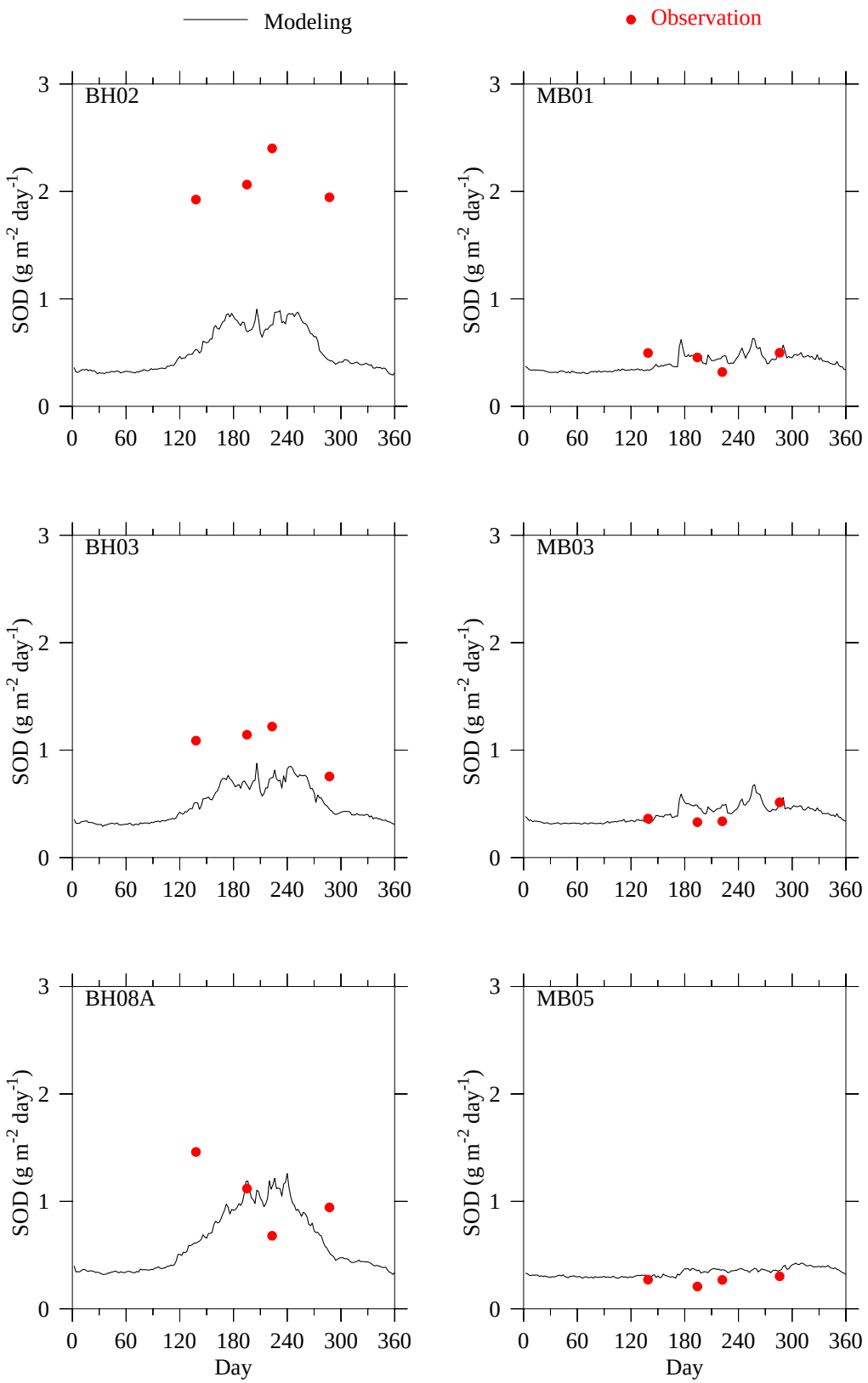

Figure 3. 40 Comparison of sediment oxygen demand observed (dots) and modeled (lines) time-series in 2009.

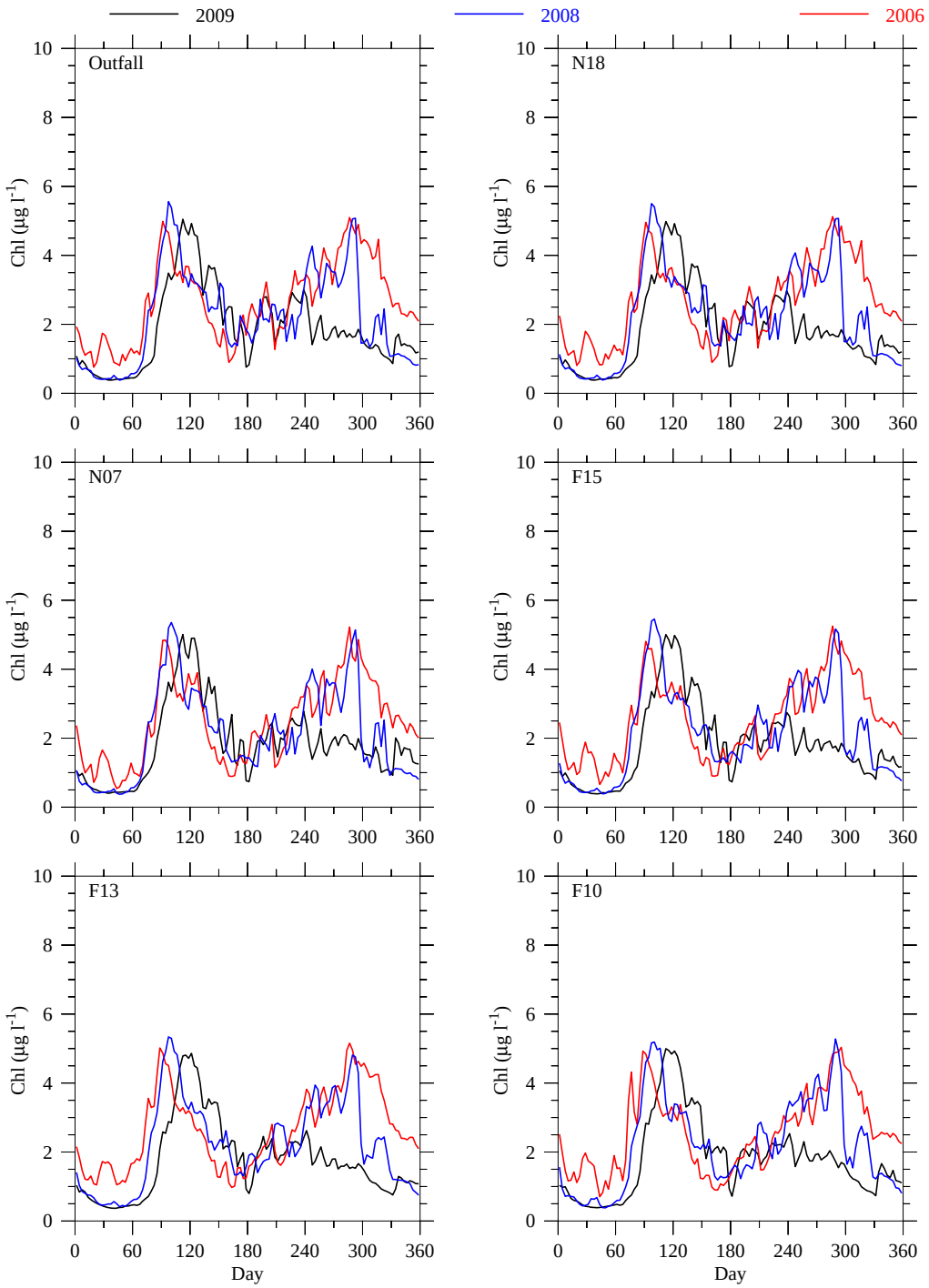

Figure 3. 41 Seasonal and interannual variations in surface chlorophyll concentration at the MWRA outfall site and Stations N18, N07, F15, F13 and F10 computed for 2006 (red lines), 2008 (blue lines) and 2009 (black lines).

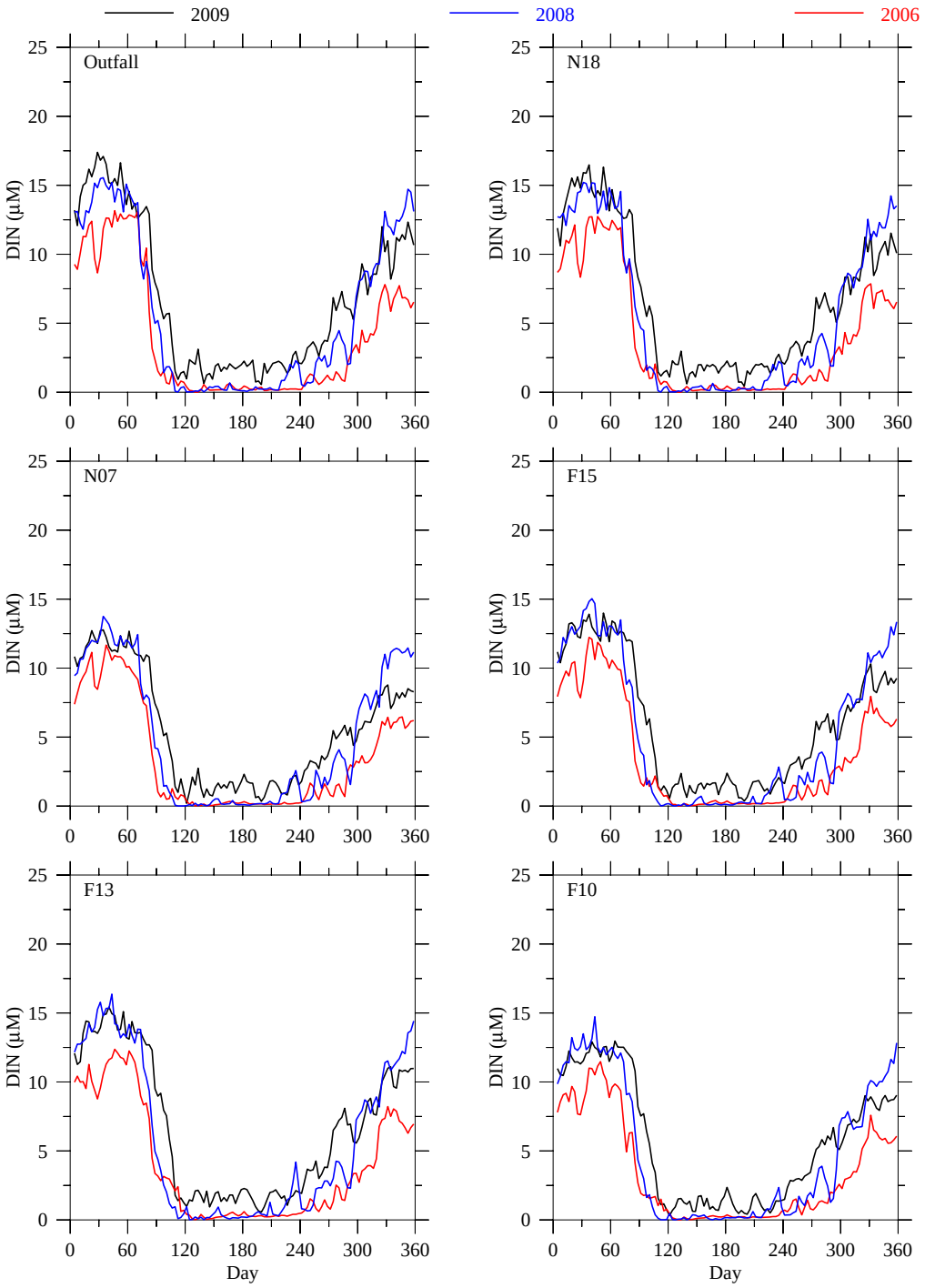

Figure 3. 42 Seasonal and interannual variations in surface DIN concentration at the MWRA outfall site and Stations N18, N07, F15, F13 and F10 computed for 2006 (red lines), 2008 (blue lines) and 2009 (black lines).

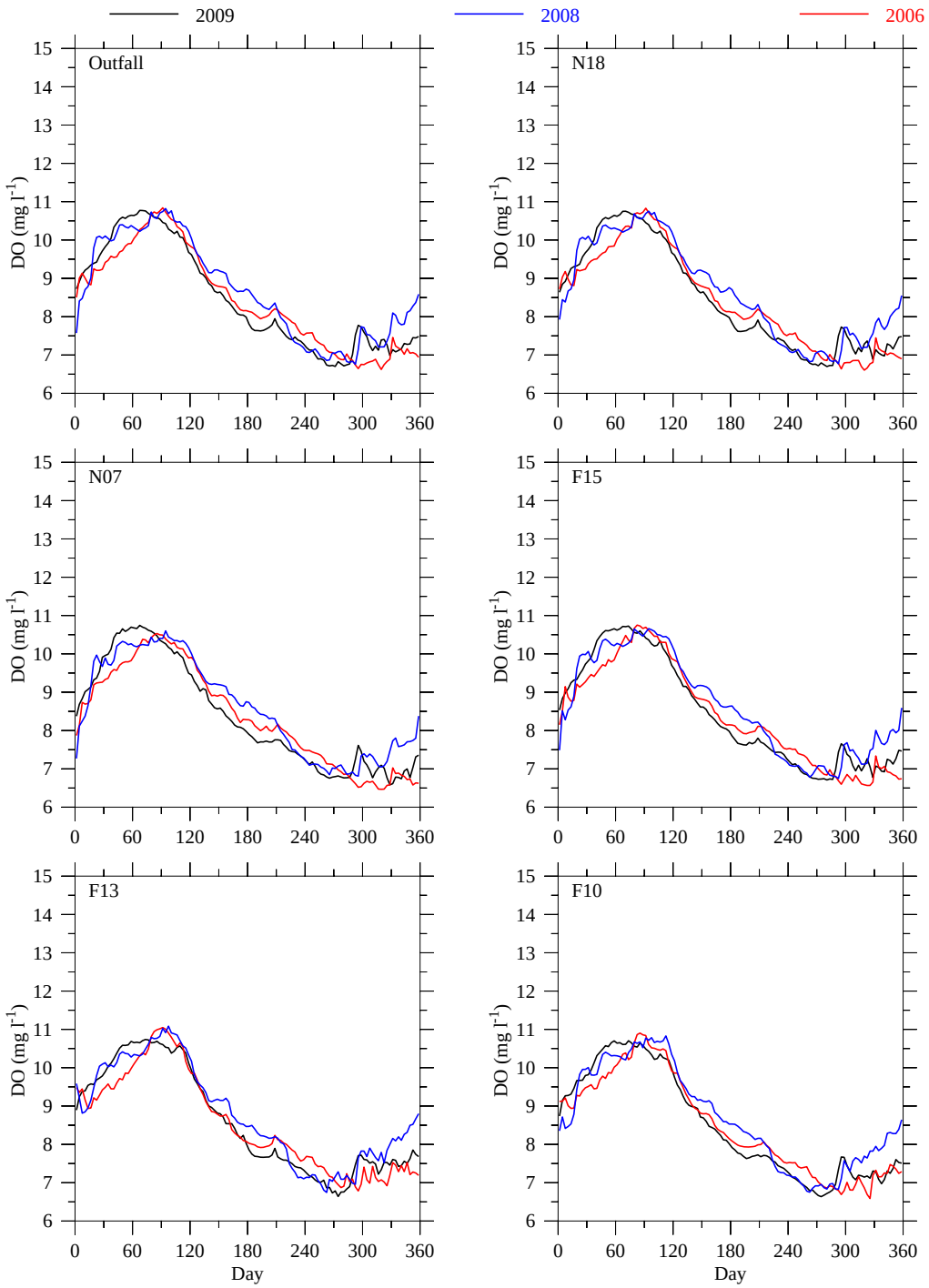

Figure 3. 43 Seasonal and interannual variations in bottom DO concentration at the MWRA outfall site and Stations N18, N07, F15, F13 and F10 computed for 2006 (red lines), 2008 (blue lines) and 2009 (black lines).

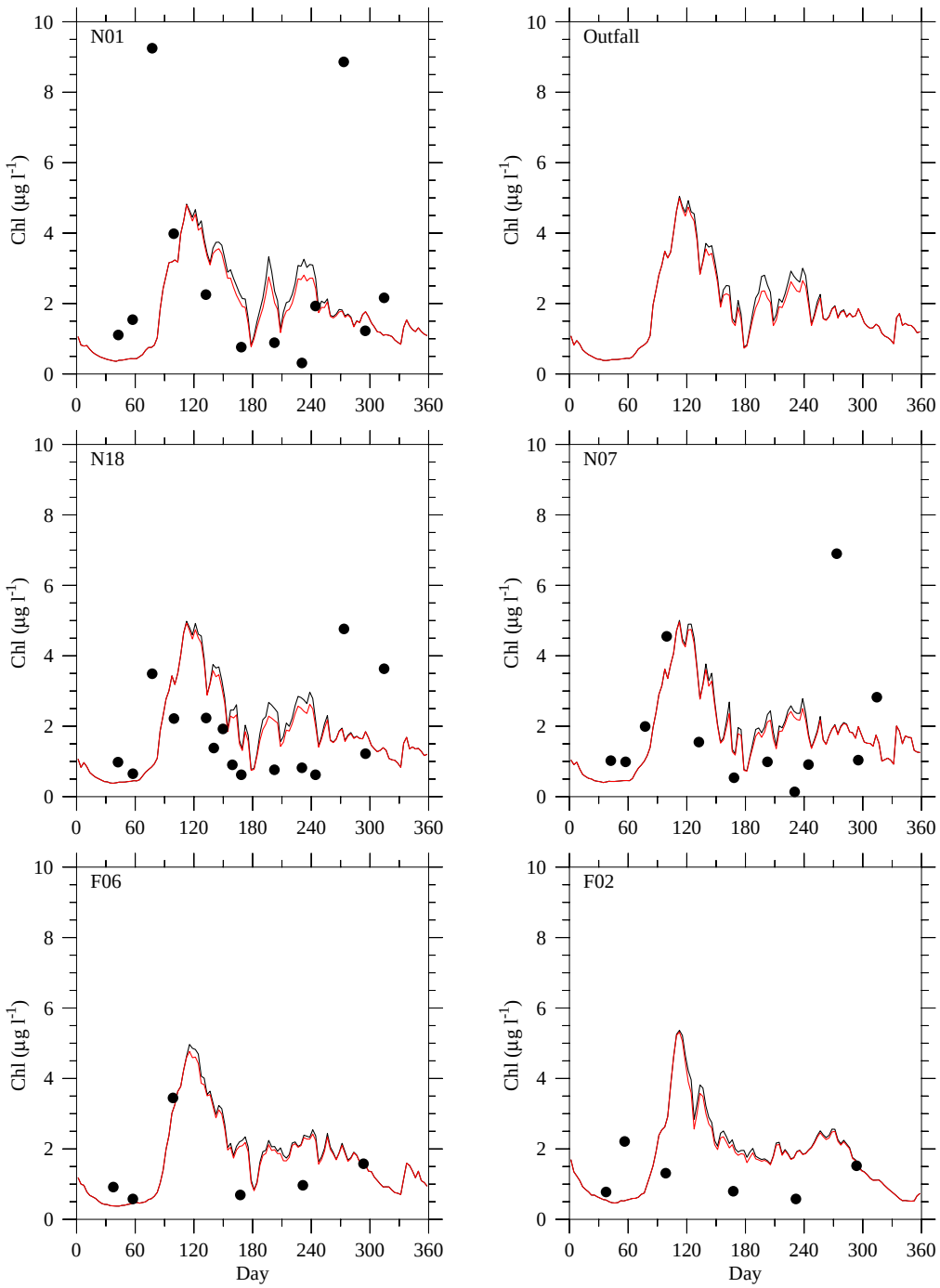

Figure 4. 1 Comparison of surface chlorophyll concentration between the Control (black) and Non-sewage (red) experiments at selected monitoring stations in 2009. Black dots show observed values.

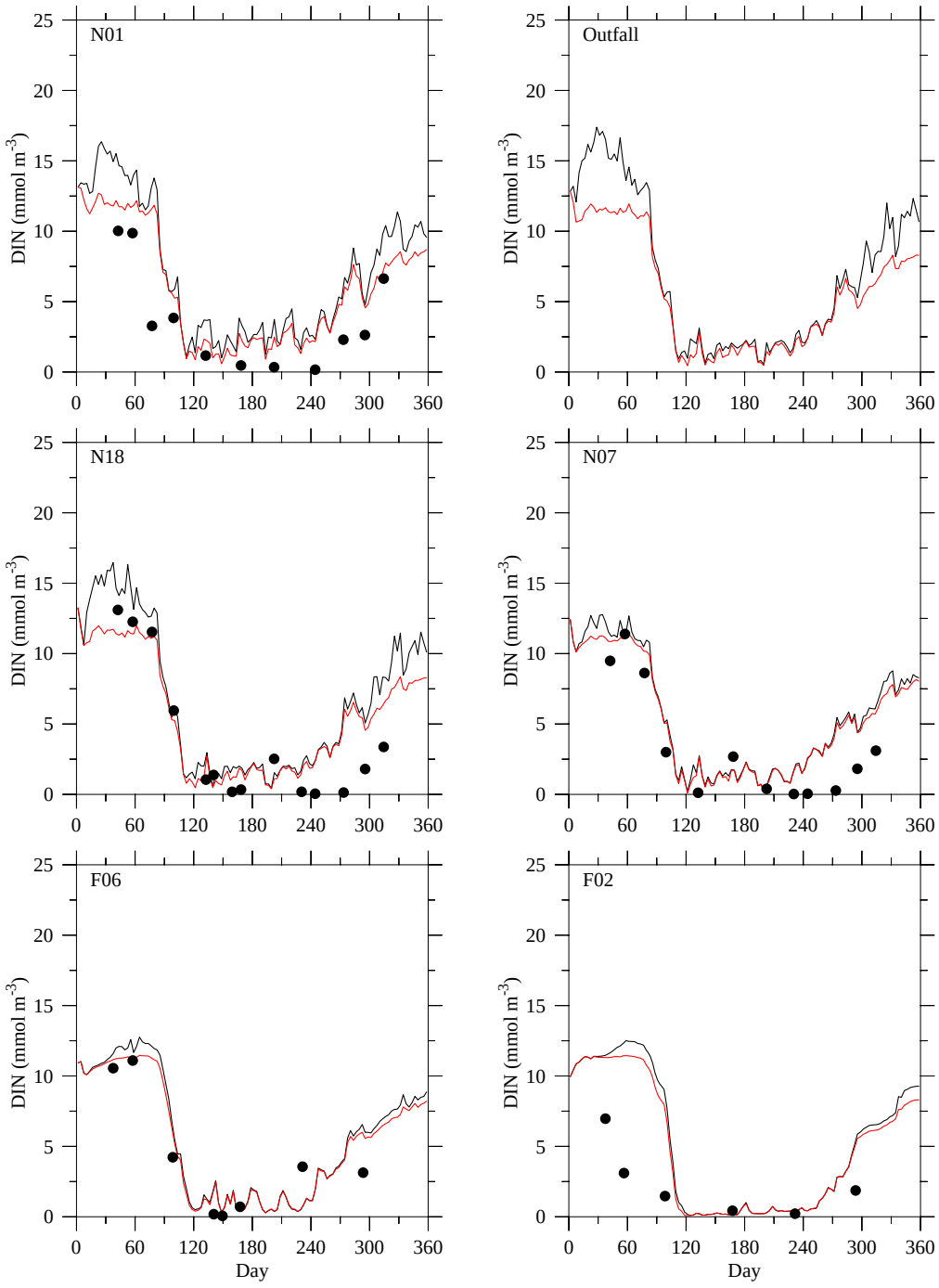

Figure 4. 2 Comparison of surface DIN concentration between the Control (black) and Non-sewage (red) experiments at selected monitoring stations in 2009.

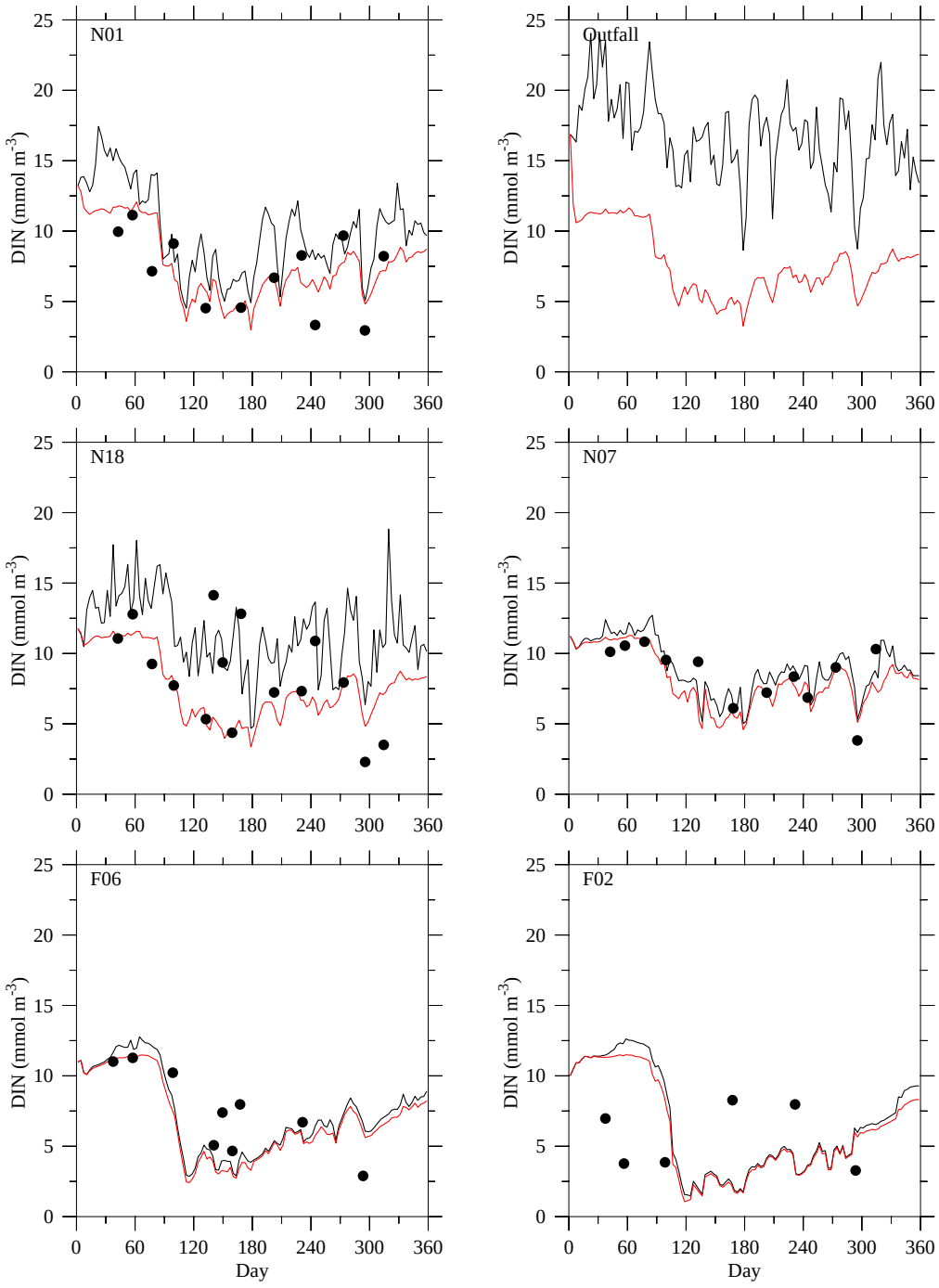

Figure 4. 3 Comparison of bottom DIN concentration between the Control (black) and Non-sewage (red) experiments at selected monitoring stations in 2009.

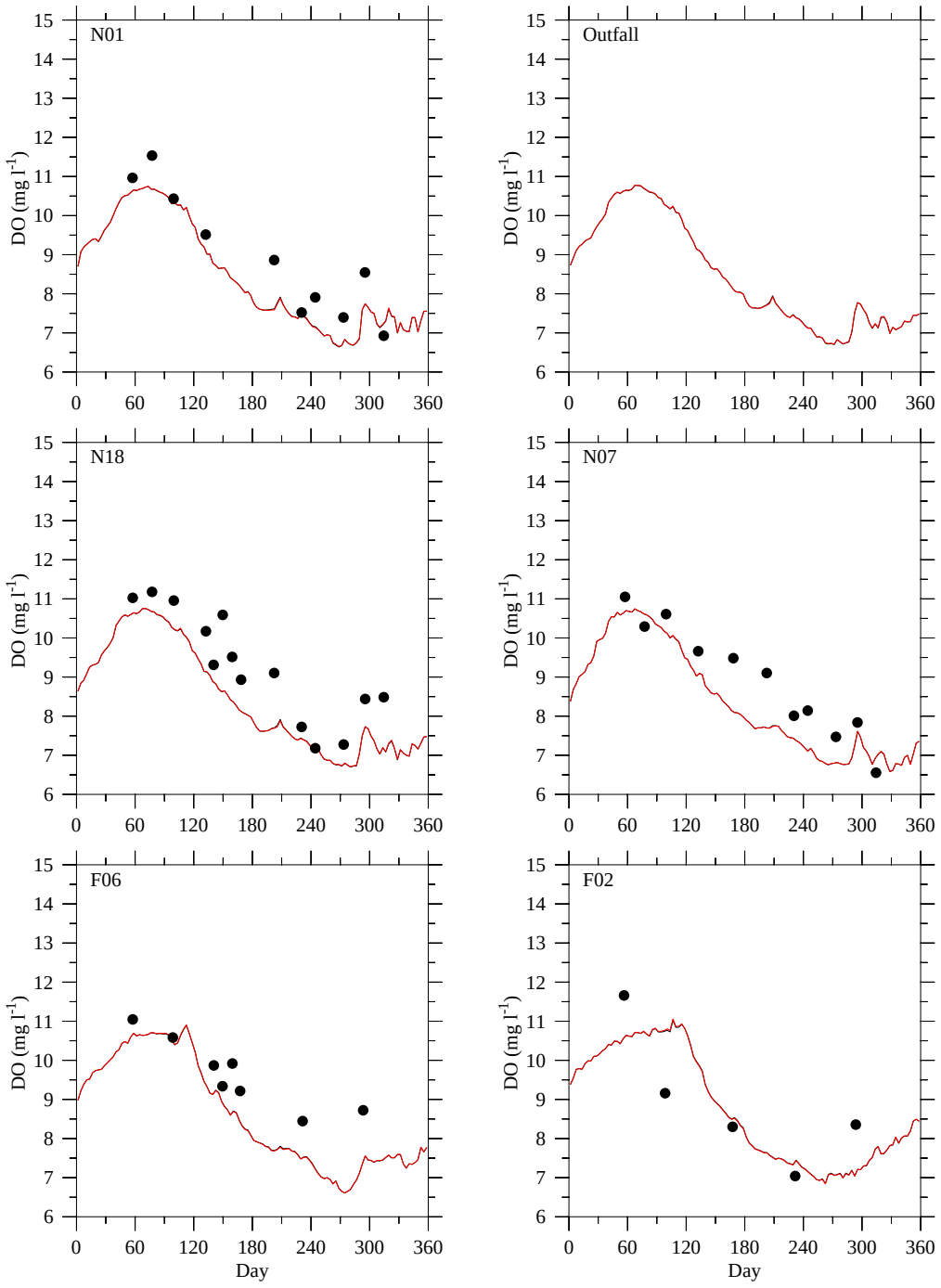

Figure 4. 4 Comparison of bottom dissolved oxygen concentration between the Control (black) and Non-sewage (red) experiments at selected monitoring stations in 2009.

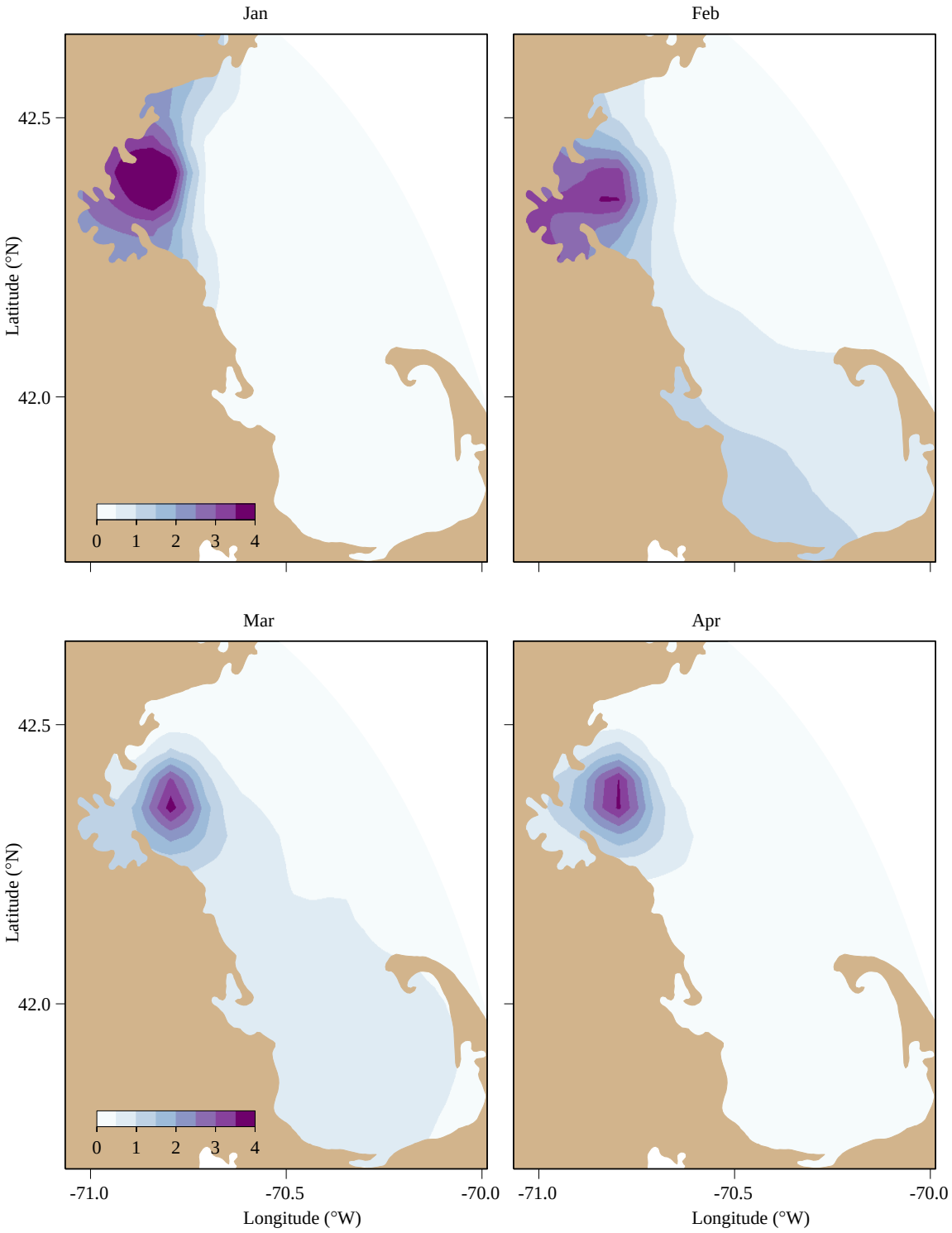

Figure 4. 5 Differences in bottom NH_4^+ concentrations (μM) at the end of January, February, March and April between the Control and Non-sewage experiments in 2009.

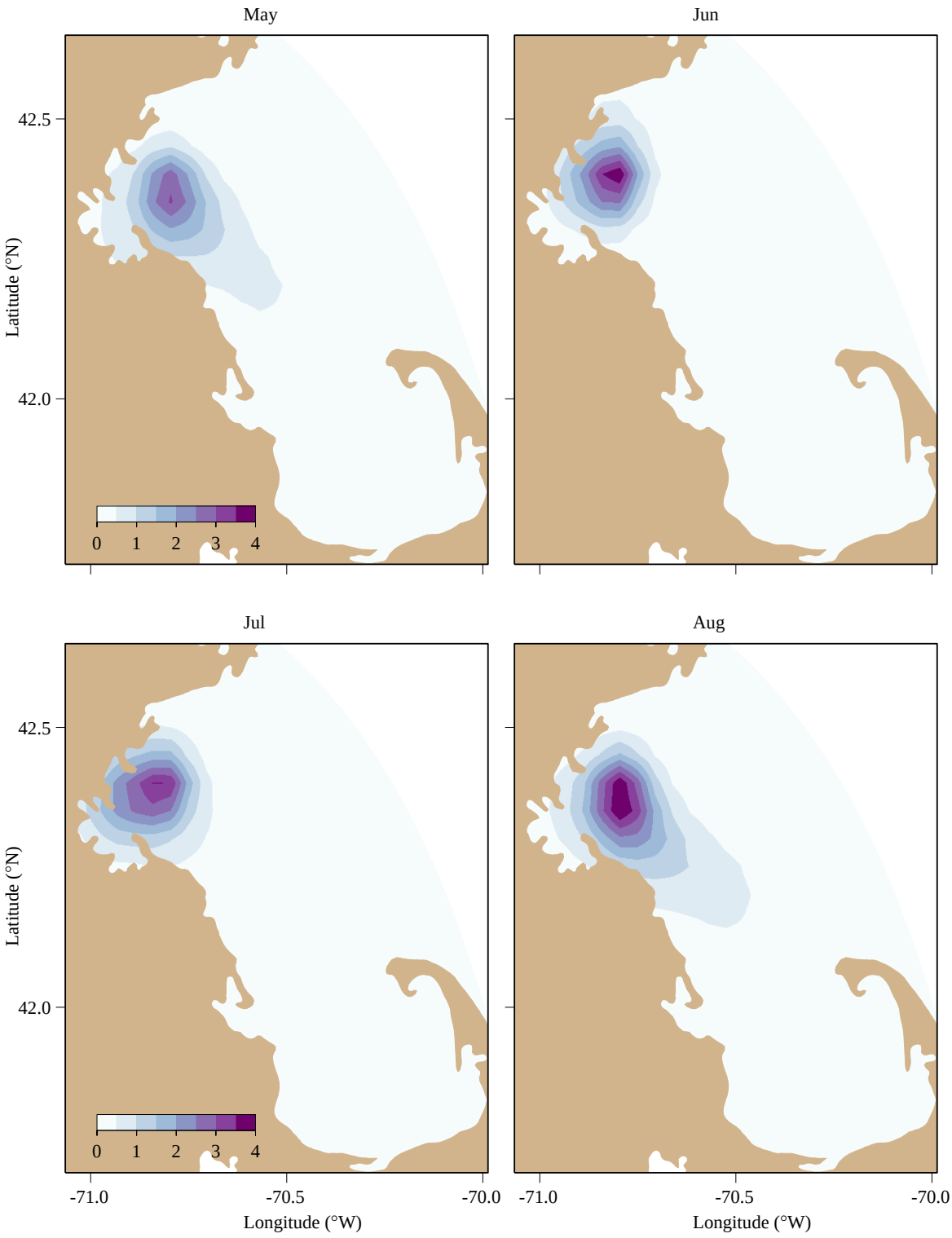

Figure 4. 6 Differences in bottom NH_4^+ concentrations (μM) at the end of May, June, July and August between the Control and Non-sewage experiments in 2009.

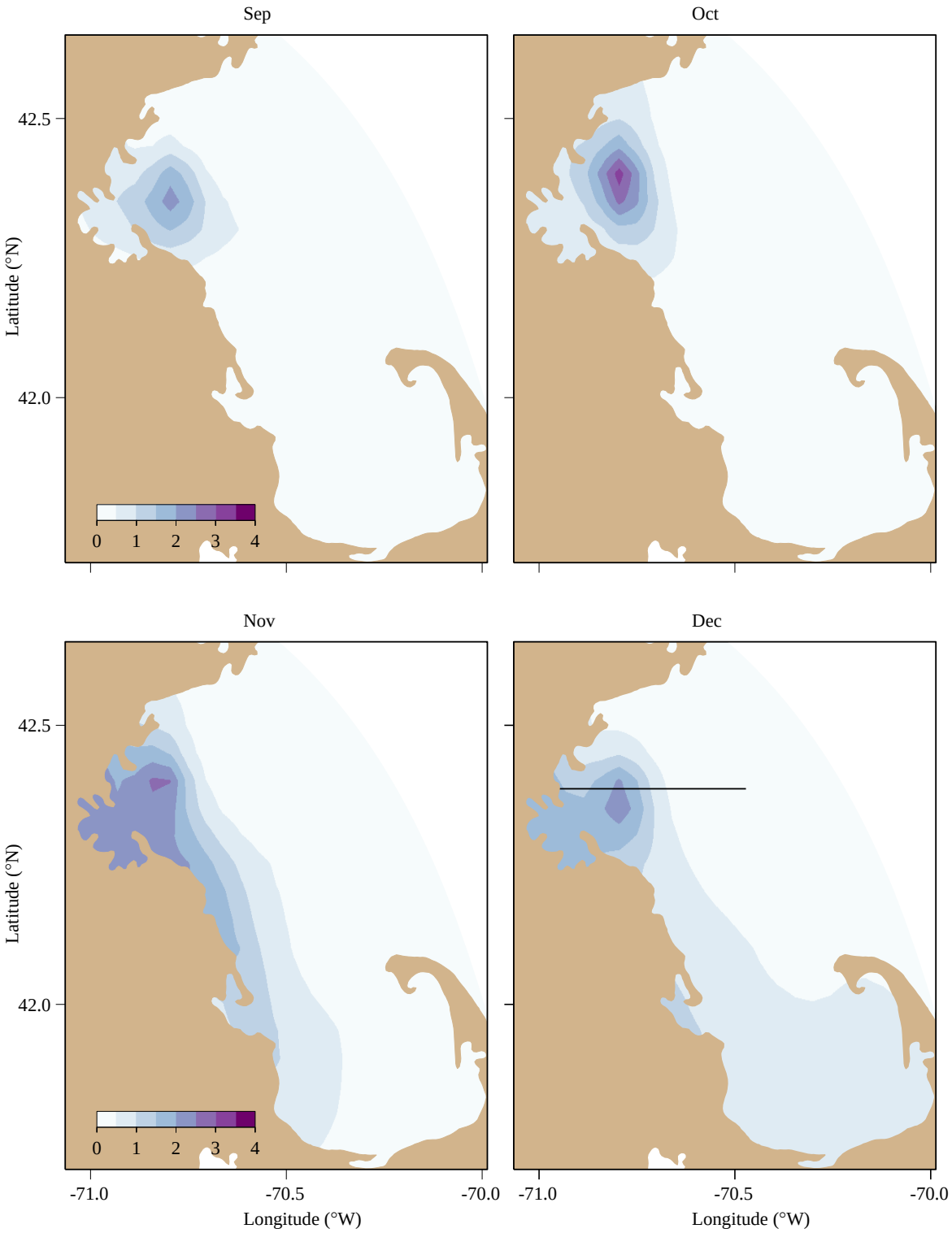

Figure 4. 7 Differences in bottom NH_4^+ concentrations (μM) at the end of September, October, November and December between the Control and Non-sewage experiments in 2009. Black line indicates the transect depicted in the following figures.

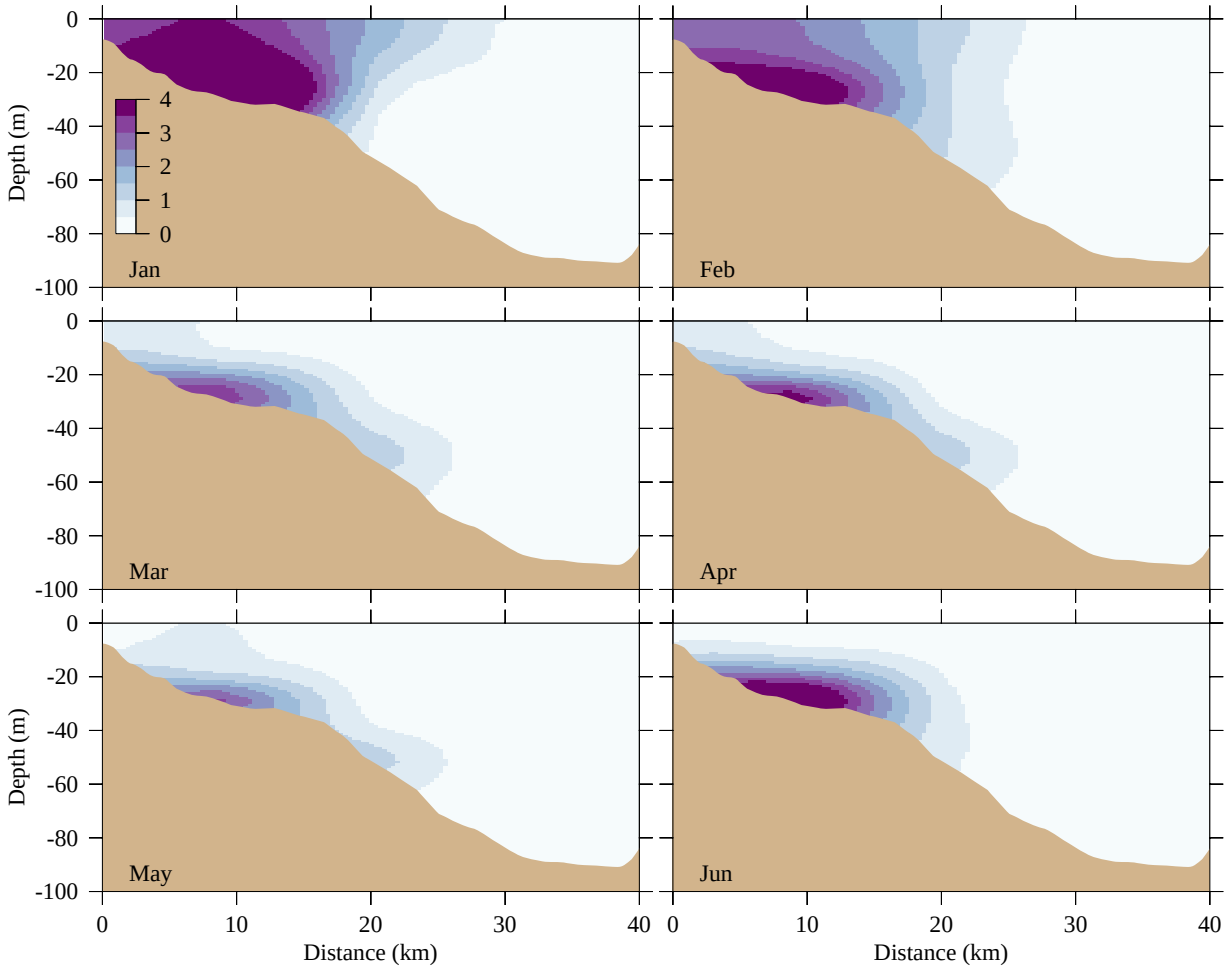

Figure 4. 8 Differences in NH_4^+ concentration (μM) on an east-west transect across the MWRA outfall at the end of each month from January through June between the Control and Non-sewage experiments in 2009.

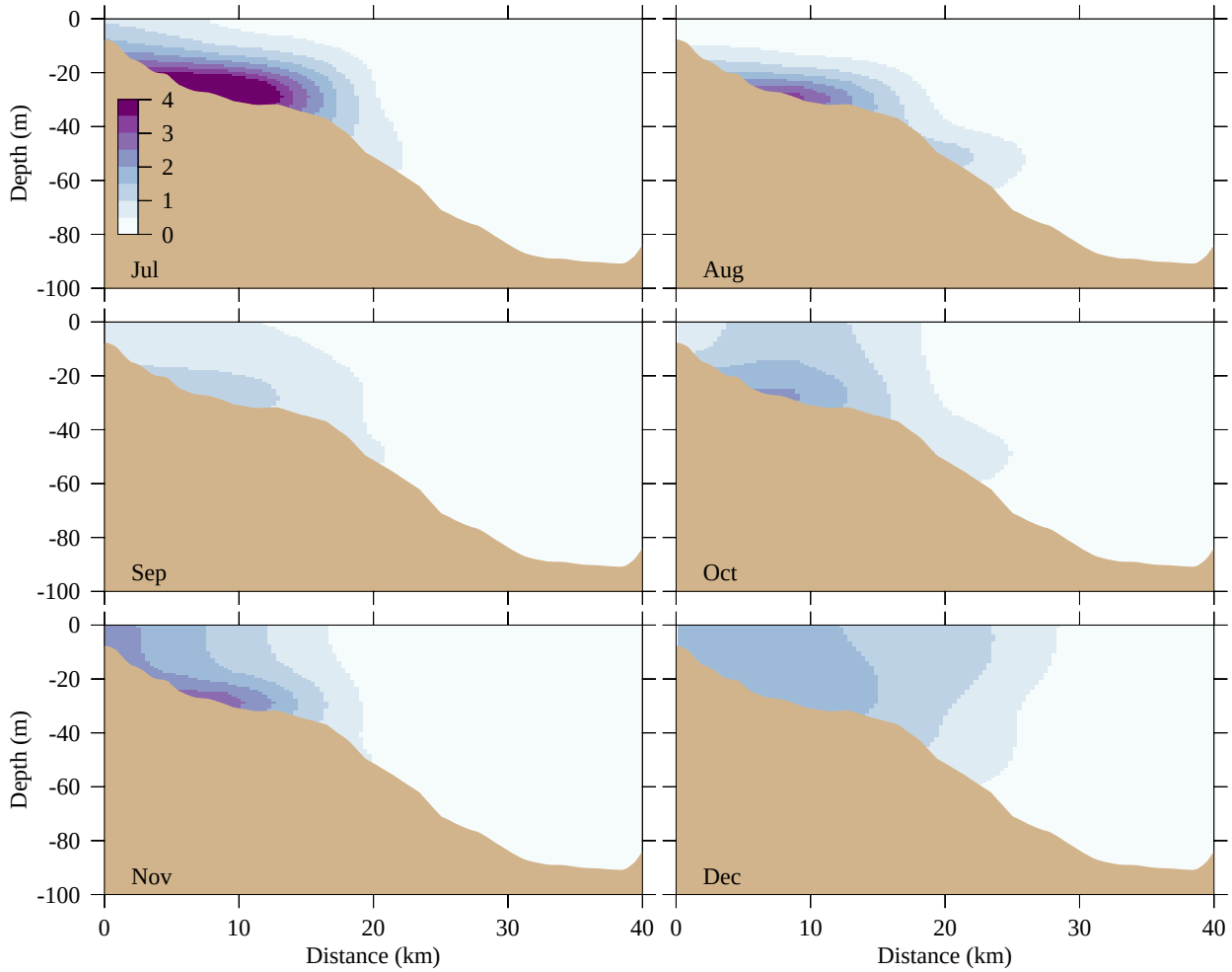

Figure 4. 9 Differences in NH_4^+ concentration (μM) on an east-west transect across the MWRA outfall at the end of each month from July through December between the Control and Non-sewage experiments in 2009.

Massachusetts Water Resources Authority
Charlestown Navy Yard
100 First Avenue
Boston, MA 02129
(617) 242-6000
http://www.mwra.state.ma.us